DEUTSCHES ELEKTRONEN-SYNCHROTRON

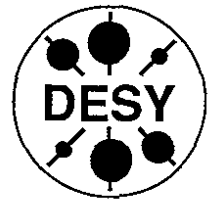

DESY 94-085
May 1994

An Analysis of the Long-Term Stability of the Particle Dynamics in Hadron Storage Rings

O. S. Brüning
Fachbereich Physik, Universität Hamburg

ISSN 0418-9833

NOTKESTRASSE 85 - 22603 HAMBURG

To be sure that your preprints are promptly included in the HIGH ENERGY PHYSICS INDEX, send them to (if possible by air mail):

DESY
Bibliothek
Notkestraße 85
22603 Hamburg
Germany

DESY-IfH
Bibliothek
Platanenallee 6
15738 Zeuthen
Germany

DESY 94-085
May 1994

ISSN 0418-9833

An Analysis of the Long-Term Stability of the Particle Dynamics in Hadron Storage Rings

Dissertation
zur Erlangung des Doktorgrades
des Fachbereichs Physik
der Universität Hamburg

vorgelegt von
Oliver Sim Brüning
aus Hamburg

Hamburg 1994

Gutachter der Dissertation:	Prof. Dr. J. Bartels Dr. H. Mais
Gutachter der Disputation:	Prof. Dr. J. Bartels Prof. Dr. P. Schmüser
Datum der Disputation:	09.05.1994
Sprecher des Fachbereichs Physik und Vorsitzender des Promotionsausschusses:	Prof. Dr. E. Lohrmann

Kurzfassung

Indem die existierenden Modelle für die Teilchenbewegung in einem Speicherring auf den Fall von mehr als einer Modulationsfrequenz erweitert werden, untersucht die vorliegende Arbeit die Teilchendiffusion durch das Zusammenwirken von nichtlinearen Feldern und Modulationseffekten. Da die untersuchten Diffusionsmechanismen nicht von der detaillierten Aufstellung der Magnete im Speicherring abhängen, untersucht die vorliegende Arbeit die Teilchendiffusion zunächst an einer Modellstruktur für den Speicherring und wendet erst in einem zweiten Schritt die so gewonnenen Ergebnisse auf die Teilchendynamik in existierenden Speicherringen an.

Nach einer Zusammenfassung der wichtigsten Aspekte der nichtlinearen Teilchendynamik illustriert die Arbeit, durch welche Mechanismen die Modulationseffekte die dynamische Apertur eines Speicherrings beeinträchtigen.

In einem zweiten Schritt erweitert die vorliegende Arbeit die Stabilitätsanalyse und berechnet Diffusionsraten für die Teilchenbewegung weit innerhalb der dynamischen Apertur. So eine Teilchendiffusion wird zum Beispiel durch das Zusammenwirken von Modulationseffekten und der nichtlinearen Strahl-Strahl Wechselwirkung verursacht. Die Berechnung der Diffusions- und Driftkoeffizienten bezieht sich auf die Parameterwerte des Protonenspeicherrings in HERA, wo die Strahllebensdauer deutlich durch die Strahl-Strahl Wechselwirkung beeinträchtigt wird.

Die Analyse der Diffusionsmechanismen zeigt, daß eine Modulation der Betatronfrequenzen mit schnellen und langsamen Frequenzkomponenten zu einer verstärkten Teilchendiffusion führt. Im Protonenspeicherring von HERA werden die langsamen Frequenzkomponenten der Betatronfrequenzmodulation durch die Bodenbewegung im HERA Tunnel und die schnellen Frequenzkomponenten durch Rippel in den Gleichstromnetzgeräten erzeugt. Ausgehend von konstanten Modulationstiefen für die langsamen Frequenzkomponenten werden obere Grenz- werte, die mit einem effizienten Betrieb des Speicherrings verträglich sind, für die Modulationstiefen der schnellen Frequenzkomponenten bestimmt. Die analytisch berechneten Driftkoeffizienten stimmen sowohl qualitativ als auch quantitativ mit den Daten einer numerischen Simulation der Teilchenbewegung überein. Darüberhinaus zeigt ein Vergleich der berechneten Driftkoeffizienten mit den während des Luminositätbetriebs in HERA gemessenen Daten für die Protonenstrahlgröße, daß die untersuchten Mechanismen zu Anwachsraten von der gleichen Größenordnung führen wie sie im Protonenstrahl beobachtet werden.

Ausgehend von einer Strahl-Strahl Wechselwirkung für flache Strahlen und den Parameterwerten in HERA deuten die analytischen Abschätzungen auf eine empfindliche Abhängigkeit der Anwachsraten von den schnellen Modulationsfrequenzen hin. Eine solche Abhängigkeit der Anwachsraten konnte in einem anschließenden Modulationsexperiment in HERA bestätigt werden, wo eine externe Modulation der Betatronfrequenzen zu einem deutlichem Zuwachs der Anwachsraten führte. Sowohl die analytischen Abschätzungen für die Anwachsraten, als auch die experimentellen Daten deuten darauf hin, daß die Teilchendiffusion im Protonenstrahl von HERA durch eine zusätzliche externe Modulation der Betatronfrequenzen beeinflußt werden kann.

Abstract

Expanding the existing models for the particle motion in a storage ring to include modulation effects with more than one frequency component, the thesis analyzes the particle diffusion due to the combined effect of non-linear fields and tune modulation. The diffusion mechanisms do not depend on the specific distribution of the non-linear fields along the storage ring. Thus, the thesis analyzes the diffusion mechanisms first on a model structure for the storage ring and applies the results of this model analysis in a second step to the particle dynamics in existing storage rings. Summarizing the main aspects of non-linear dynamics, the work illustrates the limiting effect of a tune modulation with more than one frequency component on the dynamic aperture of the storage ring. In a second step, the presented work extends the stability analysis of the particle motion in a storage ring and estimates the diffusion rates well inside the dynamic aperture. For example, a particle diffusion well inside the dynamic aperture is caused by the combined effect of tune modulation and the non-linear beam-beam interaction during luminosity operation. The calculation of the drift and diffusion coefficients focuses on an application to the proton storage ring in HERA, where the proton beam lifetime drops considerably after the proton and electron beams are brought to collision.

The analysis shows that the combined effect of slow and fast modulation frequencies leads to an increased emittance growth in the storage ring. In the proton storage ring of HERA the slow frequency components are caused by ground motion in the HERA tunnel and the fast frequency components by ripples in the power supplies. Taking the modulation frequencies and depths for the slow tune modulation as fixed parameters, the thesis provides upper limits for the modulation depths of a fast tune modulation which result in tolerable growth rates for the proton emittance. The analytically calculated drift coefficients agree qualitatively as well as quantitatively with the data of a numerical simulation for the particle dynamics. A comparison of the calculated drift coefficients with those measured in the HERA proton storage ring shows that the analyzed mechanism can lead to growth rates of the same order of magnitude as the ones measured during the luminosity operation in the HERA storage ring.

Looking at a flat electron beam and the beam-beam interaction parameters of HERA, the analytical estimates for the proton growth rates predict a high sensitivity to the particle diffusion on the frequency components of the fast fast tune modulation. This prediction regarding the growth rates was confirmed by a subsequent modulation experiment in the proton storage ring of HERA, where an external tune modulation with fast frequency components led to a drastic increase in the growth rates. Both the analytical estimates and the experimental data demonstrate that growth rates in the proton beam can be manipulated by an external tune modulation.

Contents

Section 1

Introduction

1.1 Motivation

Storage rings with colliding beams have become an important tool in physical research and proton storage rings have been successfully used in elementary particle physics for many years. The energy of the stored particles has increased with every collider generation to reach a current maximum center of mass particle energy of nearly $2TeV$ in the Fermilab Tevatron (1985). The next generation hadron colliders, proposed for the coming years, will reach even higher energies [1]. The IHEP UNK storage ring in Moscow is proposed to store protons at $3TeV$ using a bending field of 5 Tesla and the CERN LHC will store protons at $8TeV$ using a bending field of 10 Tesla. The large magnetic fields required for keeping particles of such high energies in a circular orbit are only feasible using superconducting magnets. Unfortunately, the absence of almost all resistivity in the superconducting material supports persistent currents, which result in multipole errors of the design field. At low energies, the nonlinearities induced by these multipole errors are the most prominent source for a limitation of the long-term stability of the single particle dynamics in these high energy storage rings. However, during luminosity operation at high energies, the limiting effect of the nonlinear beam-beam interaction dominates the effect of the multipole errors and spoils the long-term *stability of the single particle motion during luminosity.*

The aim of this thesis is to analyze the emittance growth in hadron storage rings due to the non-linear aspects of the particle dynamics with an emphasis on an application to the HERA proton storage ring. Finding analytical estimates for the drift and diffusion coefficients as *functions of the phase space position and the modulation parameters, this work demonstrates* how the tune modulation affects the emittance growth during luminosity operation and compares the analytical estimates with an accompanying experiment in the proton storage ring of HERA. The analytical and experimental results suggest the possibility of actively manipulating the emittance growth in HERA by means of an additional external tune modulation. The following work presents the prerequisites for such an active manipulation of the emittance growth rates in HERA.

The HERA storage ring [2] at DESY in Hamburg went into operation at the end of 1991. It is the first beam facility to bring hadrons and leptons ($820GeV$ protons and $30GeV$ electrons) to collision and it can support up to four experiments. Currently, two main experiments, H1 [3] and ZEUS [4], use the particle collisions at the interaction regions of the colliding beams

and a third experiment set to begin in 1995, HERMES [5], will look at the reactions of the electron beam with an internal gas target. In addition to these three experiments, HERA-B [6], a fourth proposed experiment, would investigate the reactions of the protons of the beam halo with an internal fixed target.

Optimizing the efficiency of the experiments in the proton beam requires an understanding of the origins for the emittance growth in the proton beam. The efficiency of the H1 and ZEUS experiments depends on the beam intensities, their sizes, the beam lifetimes, and the time required for the particle injection and acceleration. The first two quantities determine the luminosity, defined as the rate of events per cross section, and express the momentary efficiency of the experiments. As the luminosity is proportional to the beam intensities and inversely proportional to the beam sizes, high beam intensities and small beam cross sections are desirable to attain a high efficiency in the experiments. In order to achieve a large luminosity over a long period of time, it is not only important to produce initially small beam sizes, but also to keep the beam sizes small during the storing time. For this reason it is desirable to minimize the particle diffusion in the storage rings during luminosity operation.

The background rates in the main experiments are another limiting effect on the efficiency of the experiments. If the background rates become larger than a critical threshold value, the event triggers and the drift chambers inside the experiments can not operate properly. Furthermore, with increasing background rates the lifetime of the drift chamber and the electronic components inside the calorimeters are shortened.

The efficiency of the proposed HERA-B experiment depends on a different set of parameters. Here, the experiment efficiency relies on the dynamic aperture, and on the number of particles and the drift coefficients inside the proton beam halo. On the one hand, the particle diffusion at the edge of the beam core has to be large enough to result in a sufficient number of particles in the beam halo. On the other hand, the diffusion in the beam halo has to be small enough for the particles to stay inside the beam halo for a sufficiently long time period before they reach the dynamic aperture of the storage ring.

Hence, optimizing the efficiency of all three experiments in the proton storage ring requires a clear understanding of the causes for the particle diffusion in the proton beam. While the proton beam lifetime at injection energy is mainly limited by collective effects, it seems that the proton beam quality during the luminosity runs is limited by the non-linear single particle dynamics. At $820GeV$, the proton beam lifetime in HERA drops from more than $1000h$ to about $100h$ when the two beams are brought to collision, indicating a lifetime limitation due to the non-linear beam-beam interaction. Therefore, this work concentrates on the limiting effects due to the beam-beam interaction and searches for possible mechanisms that can account for the observed emittance growth in the proton storage ring of HERA *during luminosity operation.*

Recent experiments at the Fermi National Accelerator Laboratory [7] and at the SPS at CERN [8] showed that an external tune modulation in combination with non-linear fields can drastically enhance the particle diffusion and might limit the beam lifetime in the storage ring. Furthermore, R. Brinkmann [9] showed in a numerical simulation of the particle dynamics that a stochastic variation of the betatron tune as small as $\Delta Q = 10^{-3}$ in connection with the non-linear beam-beam interaction already leads to a serious emittance growth. All three examples for the enhancement of the particle diffusion due to an external tune modulation prompt an analysis of the combined effect of non-linear fields and tune modulation. In a real

storage ring, a natural tune modulation is caused by power supply ripples and by ground motion. As the diffusion due to a tune modulation with more than one modulation frequency dominates the effect of a tune modulation with only one frequency, the following analysis concentrates on the former aspect, and presents a qualitatively new approach to the analysis of the non-linear particle motion in a storage ring. The analysis provides analytical expressions for the drift and diffusion coefficients as functions of the tune values, the phase space position of the particles, and the modulation frequencies and amplitudes. The results predict a sensitive dependency of the drift and diffusion coefficients on the phase space position of the particles, on the linear tune values, and on the modulation frequencies and depths. The predictions are confirmed by the numerical simulations of the particle dynamics and agree qualitatively with the observed beam performance in the proton storage ring of HERA, where the beam lifetime during luminosity operation shows a high dependency on the horizontal and vertical tune values.

The work has two main applications for the operation of the HERA proton storage ring.

- The analytical expressions for the drift and diffusion coefficients can be used to estimate the effect of the natural tune modulation in the storage ring on the beam quality. For example, the work calculates upper limits for the modulation depths which are compatible with an efficient operation of the experiments and estimates the particle diffusion in the proton storage ring due to the expected fluctuations in the power supplies and the ground motion in the HERA tunnel. The following analysis will show that an efficient operation of the storage ring requires modulation amplitudes which are smaller than $\triangle Q = 1.0 \cdot 10^{-4}$.

- The results can be used for an external excitation of a tune modulation in order to manipulate the existing particle diffusion in the proton beam. Assuming the combined effect of non-linear fields and tune modulation as the cause for the emittance growth in HERA, such an additional external tune modulation can either be used to compensate for harmful frequency components in the natural modulation spectrum [10], and hence to reduce the particle diffusion, or to generate frequency components which create a local particle diffusion in the beam halo as it would be useful for the HERA-B experiment. The following analytical diffusion analysis provides the prerequisites for realizing such a controlled external tune modulation in HERA.

A subsequent diffusion experiment in HERA successfully demonstrated the validity of the analytical estimates and showed that modulation depths as small as $\triangle Q = 1.0 \cdot 10^{-4}$ in combination with the non-linear beam-beam interaction lead to a drastic increase of the diffusion coefficients in HERA. Furthermore, the experiment confirmed the expected dependency of the diffusion coefficients in HERA on the modulation frequencies.

1.2 Outline

The thesis is organized as follows:

First, a survey section summarizes the activities related to the question of long-term stability in complex Hamilton systems.

Section three introduces the model structure for the analytical analysis of the particle dynamics and the corresponding map required for the numerical simulations.

The fourth section investigates the irregular particle motion in Hamiltonian systems and presents criteria for the onset of such irregular motion.

Introducing modulation effects into the Hamilton system, the fifth section illustrates how the irregular aspects of the particle motion can be enhanced by the modulation effects.

Recognizing the importance of the tune modulation for the particle diffusion in a storage ring, the sixth chapter discusses the potential sources of the tune modulation in a real storage ring and gives estimates for the modulation amplitudes in the proton storage ring of HERA.

Section seven applies the results of Sections four and five to the particle dynamics in a storage ring and demonstrates how the tune modulation with more than one frequency component can drastically reduce the dynamic aperture in the storage ring.

The eighth section analyzes to what extent the criteria for the onset of irregular particle motion can be applied to the beam-beam interaction with tune values close to the coupling resonance.

Section nine formulates the diffusion models for the particle dynamics in a storage ring and presents analytical expressions for the drift and diffusion coefficients as a function of the phase space position, the tune values, and the modulation frequencies and amplitudes. The analytical estimates are first compared with tracking data to check the validity of the approximations used in the analytical calculations and subsequently with measured drift coefficients in the proton storage ring of HERA.

The analytical estimates indicate a sensitive dependence of the drift coefficients on the modulation amplitudes of the fast frequency components. Recognizing the damaging effect of the tune modulation on the long term stability of the particle motion, the thesis proposes a new method for compensating the harmful frequency components in a storage ring by actively modulating the current in the proton quadrupoles.

Chapter twelve summarizes the results of a subsequent modulation experiment in the proton storage ring of HERA, which successfully probed the applicability of the analytical results for HERA. The experimental data agree qualitatively as well as quantitatively with the analytical estimates and the tracking data.

Finally, the results are summarized in the last chapter.

Section 2

The Question of Long-Term Stability in Complex Dynamical Systems

The question of long-term stability of the particle motion in a storage ring is very similar to the stability question of the planetary motion in our solar system and suggests a stability analysis with the same tools. Both systems are quasi periodic Hamilton systems and require a stability analysis over the time scale of 10^8 periods of the particle motion. The following overview attempts to explain the way in which the tools of celestial mechanics enter the analysis of the particle dynamics in storage rings and to illustrate the principle difficulties related to such an analysis. In a first step, the overview introduces the concept of perturbation theory, which will turn out to be very useful for an analysis of the short-term behaviour of the particle dynamics in a storage ring. In a second step, the overview introduces the concept of irregular motion in Hamiltonian systems and illustrates how the irregular character of the particle motion spoils the concept of perturbation theory. Subsequently, the possibilities for a numerical and analytical analysis of the long-term behaviour of the particle motion are briefly discussed.

Assuming that the planetary motion is ultimately regular and might be solved once the appropriate mathematical tools are available, Poincaré [11] and von Zeipel [12] developed a perturbative method for the stability analysis of near integrable Hamiltonian systems. The method is based on the division of the Hamilton function into an integrable part and a small perturbation. In the case of the solar system the integrable part is given by the completely integrable Hamiltonian corresponding to the two body problem in classical mechanics. In the case of the particle motion in a storage ring the integrable part is given by the Hamilton function of a set of coupled harmonic oscillators. For small perturbations one can transform the system to a new set of coordinates for which the Hamilton function consists of a new integrable term and a perturbation that is smaller than the initial perturbation term. Thus, a successive application of suited coordinate transformations allows the construction of an integrable Hamilton function that approximates the initial system to a desired accuracy. The integrable part of the Hamilton function is also called the 'normal form' of the system [13]. For a Hamiltonian with N degrees of freedom, the normal form has N isolating integrals that must be in involution, i.e., their Poisson brackets with each other must vanish, and the trajectory of the particle motion lies on the surface of an N-dimensional invariant torus in the phase space, the N axes of which correspond to the N invariants of the particle motion [13][14]. Unfortunately, the important question whether the sequence of coordinate transformations

finally converges and whether the system actually has a completely integrable Hamilton function can not generally be answered. In fact, one knows that a Hamilton system with more than one degree of freedom is generally non-integrable. Hence, using perturbation theory in the analysis of non-integrable systems, one has to give a reason for calculating an approximation to a non-existing function. At this point the KAM theorem plays a fundamental role. The theorem was originally postulated by Kolmogorov [15] and proved independently under different restrictions by Arnold [16] and Moser [17]. The KAM theorem states that for near-integrable systems, invariant surfaces continue to exist for most initial conditions. These invariant surfaces are also called 'KAM tori'. For small perturbations, the dynamics in a near-integrable Hamilton system can be approximated by the dynamics in the normal form Hamiltonian which is related to the invariant surfaces.

The concept of perturbation theory has proven to be extremely useful in describing the short-term behaviour of near-integrable systems and has found a wide range of applications. Over the years, the classical method of Poincaré and von Zeipel has been drastically improved by the use of Lie-algebraic methods and the use of Differential Algebra tools. While the use of canonical mixed variable transformations [18] makes it difficult to explore the perturbation theory of Poincaré and von Zeipel to a high order in the perturbation parameter, the use of Lie transformations allows a perturbative treatment up to very high orders in the perturbation parameter. For example, Dragt and Finn [19][20] and Forest [21][22][23] showed how the normal form algorithm can be formulated for maps and how the algebraic structure of Lie transformations can be used for the calculation of normal forms up to arbitrary order using a computer code. A further improvement of the perturbation techniques started with the introduction of Differential Algebra tools [24] [25], which allow the construction of Taylor maps even if the analyzed system is extremely complicated or only defined by a set of symplectic kicks.

Alternatively, Warnock and Ruth [26] and Gabella [27] explored a method to compute invariant tori by solving directly the Hamilton-Jacobi equation. Their method is based on stating the Hamilton-Jacobi equation as a system of equations for the Fourier coefficients of the generating function, and to solving these equations numerically by Newton's method. Using a tracking code for the generation of the input data, they successfully used their method in the calculation of invariant tori in the phase space of a storage ring.

The possibility to calculate normal forms to a high order in the perturbation parameter opens a wide range of applications to particle accelerator physics. For example, with the help of Differential Algebra tools and perturbation theory, one can calculate the machine chromaticity, the detuning and coupling terms due to the non-linear elements, and the locations and strengths of the resonances in the storage ring [28][29].

Even though the particle motion in near-integrable systems lies on invariant surfaces for most initial conditions, there are some areas in the phase space where the particle motion is irregular and can not be approximated by the dynamics in a normal form Hamiltonian. The intricate nature of the motion near unstable fixed points of the near-integrable system leads to an irregular behavior and to ergodicity [30][31][32][33][34][35]. Such regions of irregular particle motion are called stochastic layers. In the vicinity of these stochastic layers, the perturbation series will not converge and the system has no normal form.

Because the trajectories in the stochastic layer are extremely sensitive to their initial conditions, it makes no sense to talk about individual trajectories. Rather, the ergodic character of the particle motion suggests a description of the particle dynamics in terms of stochastic quantities, like diffusion and drift coefficients. In two-dimensional systems and for small perturbations, the ergodic motion in such stochastic layers is bound by KAM surfaces [13] and the stochastic layers of different resonances are separated from each other by stable invariant tori [36]. For small perturbations, the irregular motion is therefore limited to very small regions in the phase space. However, this is not true for systems with more than two dimensions where the stochastic layers of different resonances do intersect. Because of the ergodic character of the motion inside the stochastic layer, it will inevitably spread out over the whole system of intersecting layers. Arnold [37] conjectured that such an instability is generic for many-dimensional non-linear oscillator systems. The particle spread due to such an instability is called 'Arnold diffusion' [38][39] and might spoil the long-term stability of many-dimensional systems.

As the perturbation theory can not account for the irregular aspects of the particle motion, an estimate of the stability time with the help of perturbation theory is very troublesome. Initial attempts to estimate the long-term stability analytically with the help of perturbation theory were done by Nekhoroshev [40]. Nekhoroshev gave a rigorous estimate about the long-term stability in near-integrable systems and showed that the stability time increases exponentially as the perturbation strength decreases linearly. This general result relies on a careful partitioning of the phase space to deal with the resonances and a subtle analysis of the corresponding perturbation theories. Unfortunately, the method tends to overestimate the effects of the regions of stochasticity on the long-term stability and does not allow the calculation of local drift and diffusion coefficients. A different version of the Nekhoroshev estimate and its application to the particle motion in a storage ring has been given by Turchetti [41]. Using the Birkhoff method [42], Turchetti estimates the stability time for symplectic maps. Alternatively, Warnock and Ruth used their method of numerically solving the Hamilton-Jacobi equation with the help of tracking data for an estimate of the long-term stability of the particle motion in a storage ring [43][44][45]. The method is capable of identifying regions in phase space, where the particle motion remains bound over 10^8 turns and promises a practical application in accelerator physics. However, like the Nekhoroshev estimate, both methods tend to overestimate the effect of the regions of stochasticity and do not allow the calculation of local drift and diffusion coefficients.

A realistic estimate for the particle diffusion due to the irregular character of the particle motion in near-integrable systems relies on numerical techniques as well as on explicit models for the diffusion mechanisms. Up to now, a quantitative stability analysis of the particle motion in storage rings mainly relied on numerical techniques using tracking codes [46][28][29]. For example, for the proton storage ring in HERA, the generation of survival plots, surfaces of sections [13] and Lyapunov exponents [47][48][13] was used to estimate the dynamic aperture and the long-term stability of the particle motion [49][50][51][52]. However, the possibility of estimating the resonance parameters in a storage ring with the help of perturbation theory, Differential Algebra and numerical tracking codes suggested attempting the combination of numerical tracking techniques with analytical models for the particle diffusion. First attempts to combine the numerical techniques with analytical models for the particle diffusion

were extremely fruitful [53] and prompt attempts to use existing diffusion models of non-linear dynamics for a quantitative analysis of the emittance growth in hadron storage rings.

Starting point for such a quantitative analysis of the diffusion processes in a storage ring is a careful analysis of the applicability of the diffusion models in non-linear dynamics to the particle motion in a storage ring. While the particle motion in a storage ring corresponds to a perturbed linear system, the diffusion models in non-linear dynamics generally rely on perturbed non-linear systems. For this reason, the applicability of the diffusion mechanisms from non-linear dynamics can not be taken for granted and has to be carefully analyzed.

So far, an analytical analysis of the non-linear particle motion in storage rings focused on estimating the dynamic aperture in the storage rings and did not attempt to evaluate local diffusion and drift coefficients. However, optimizing the machine performance during luminosity conditions requires an analytical understanding of the particle diffusion in the beam halo and close to the beam core. The aim of this thesis is to evaluate diffusion and drift coefficients well inside the dynamic aperture and to extend the diffusion analysis to the case of a tune modulation with more than one frequency component. Looking at a tune modulation with more than one frequency component the work uses the 'modulational diffusion' [54] for a quantitative estimate of the drift and diffusion coefficients in the proton beam of HERA. While the 'Arnold Diffusion' is too slow as to account for the proton diffusion in HERA during luminosity operation, the emittance growth rates due to the 'modulational diffusion', as it is caused by the combined effect of non-linear fields and tune modulation, are of the same order of magnitude as the measured rates in HERA. The analytical analysis demonstrates how the effect of a coupling resonance and the case of more than one sum resonance can be incorporated into the diffusion analysis.

The analytical and the numerical estimates illustrated the relevance of the 'modulational diffusion' for the luminosity operation of HERA and initiated a subsequent diffusion experiment in the proton storage ring of HERA. The experiment successfully demonstrated that modulation depths as small as $\Delta Q = 10^{-4}$ have a significant effect on the particle diffusion in the proton beam and that the diffusion rates show a high dependency on the modulation frequency.

The analytical calculations are based on a Hamiltonian approach to the particle dynamics in the storage ring and the next section presents the Hamilton function corresponding to the particle motion in a storage ring with tune modulation.

Section 3

A Hamiltonian Model for the Particle Motion in a Storage Ring

As an analytical model analysis of the particle motion is the prerequisite for an understanding of the diffusion mechanisms and for calculating analytical expressions for the diffusion and drift coefficients in a storage ring, it forms the starting point of the following analysis. The construction of the model structure consists of two parts. In a first step, the Hamilton function for the particle motion in a storage ring with multipole errors, non-linear beam-beam interaction and tune modulation is presented. In a second step, the one-turn map for the particle motion in the model structure is constructed. The map expresses the particle position after the $(h+1)^{th}$ passage through the model structure as a function of the particle coordinates after the h^{th} passage through the model ring. The non-linear one-turn map will be used for the numerical simulation of the particle dynamics and for the construction of the surfaces of section [11][13] (SoS).

3.1 The Hamilton Function

The linear, uncoupled motion of an on-momentum particle in a FODO structure of an accelerator is governed by Hill's equations [55], i.e. linear equations with periodic coefficients:

$$\frac{d^2x}{ds^2} = -K_x(s)\cdot x; \qquad \frac{d^2z}{ds^2} = -K_z(s)\cdot z. \tag{3.1}$$

s is the distance along the equilibrium orbit, $K_x(s)$ and $K_z(s)$ are periodic functions of s, and x and z are the horizontal and vertical displacements of the particle from the equilibrium orbit respectively. Introducing action-angle variables via a canonical transformation using the mixed variable generating function [18]

$$F_1 = -\sum_{y=x,z}\frac{y^2}{2\beta_y(s)}\cdot\{\tan(\phi_y+\phi_{y,0})+\alpha_y(s)\} \tag{3.2}$$

$$y = \sqrt{2\beta_y(s)I_y}\cdot\cos(\phi_y); \qquad \frac{dy}{ds} = -\sqrt{\frac{2I_y}{\beta_y(s)}}\cdot\sin(\phi_y); \qquad y = x,z,$$

where $\beta_x(s)$ and $\beta_z(s)$ are the linear optic functions [55], the corresponding Hamilton function takes the convenient form

$$H = \nu_x\cdot I_x + \nu_z\cdot I_z. \tag{3.3}$$

ν_x and ν_z are the horizontal and vertical tunes

$$\nu_y = \frac{2\pi}{L}\cdot Q_y, \quad y = x,z. \tag{3.4}$$

For the sake of simplicity the following analysis assumes constant beta functions: $\beta_y(s) = 1/\nu_y$, $\alpha_y \equiv 0$, $(y = x,z)$ [55].

Introducing the potential for four sextupole kicks [56]

$$V_{sext}(x,z,s) = (\delta_{L_2}(s)+\delta_{L_3}(s)+\delta_{L_5}(s)+\delta_{L_6}(s))\cdot\frac{\lambda}{6}\cdot(x^3-3xz^2), \tag{3.5}$$

the beam-beam potential in the 'weak-strong' approximation for two interaction regions [57]

$$V_{beam}(x,z,s) = (\delta_{L_1}(s)+\delta_{L_4}(s))\cdot\frac{N_b r_p}{\gamma_p}\cdot\int_0^\infty\frac{1-\exp\left[-\frac{(x-d_x)^2}{2\sigma_x^2+q}-\frac{(z-d_z)^2}{2\sigma_z^2+q}\right]}{(2\sigma_x^2+q)^{1/2}\cdot(2\sigma_z^2+q)^{1/2}}dq, \tag{3.6}$$

the potential of six skew quadrupole kicks

$$V_{skew}(x,z,s) = (\delta_{L_1}(s)+\delta_{L_2}(s)+\delta_{L_3}(s)+\delta_{L_4}(s)+\delta_{L_5}(s)+\delta_{L_6}(s))\cdot k_s\cdot x\cdot z, \tag{3.7}$$

and a horizontal tune modulation with N frequencies, the Hamilton function (3.3) takes the form

$$\begin{aligned} H \;=\; & \nu_x\cdot\left[1+\sum_{p=1}^{N}\frac{\Delta Q_{x,p}}{Q_x}\cdot\cos\left(\frac{2\pi f_{mod,p}}{L f_{rev}}\cdot s\right)\right]\cdot I_x + \nu_z\cdot I_z + \\ & V_{sext}(I_x,I_z,\phi_x,\phi_z,s) + V_{skew}(I_x,I_z,\phi_x,\phi_z,s) + V_{beam}(I_x,I_z,\phi_x,\phi_z,s), \end{aligned} \tag{3.8}$$

where the system has been transformed to the action-angle variables

$$y = \sqrt{2\beta_y I_y}\cdot\cos(\phi_y), \quad p_y = -\sqrt{\frac{2I_y}{\beta_y}}\cdot\sin(\phi_y), \quad y = x,z. \tag{3.9}$$

defined by the canonical transformation (3.2).

λ is the integrated sextupole strength ($\lambda = \frac{e}{P_0}\int_0^L\left(\frac{\partial^2 B_z}{\partial x^2}\right)_{x=z=0}ds \rightarrow [\lambda] = \frac{1}{m^2}$). B the magnetic field, e the unit charge, L the length of the model storage ring, P_0 the particle momentum, k_s the integrated skew-quadrupole component, N_b the number of electrons per bunch, r_p the proton radius, γ_p the relativistic gamma factor of the proton beam, σ_x and σ_z the horizontal and vertical beam sizes of the electron beam, d_x and d_z are the horizontal and vertical positions of the electron beam relative to the closed orbit of the protons, f_{rev} the revolution frequency, $\Delta Q_{x,p}$ the modulation depths, $f_{mod,p}$ the modulation frequencies, and $\delta_{L_j}(s)$ are periodic delta functions ($\delta_{L_j}(s) = \sum_m\delta(s-L_j-m\cdot L)$). The beam-beam strength parameters ξ_x and ξ_z, which give the horizontal and vertical linear detuning due to the beam-beam kick per interaction region are given by [57]

$$\xi_y = \frac{N_b r_p\beta_y^*}{2\pi\gamma_p\sigma_y\cdot(\sigma_x+\sigma_z)}, \qquad y = x,z. \tag{3.10}$$

The potentials in (3.8) have a complicated dependence on the action-angle variables, which makes a discussion of the resonance structure difficult. A clear discussion of the resonance structure in (3.8) is much easier if the potential is given by its Fourier presentation. The potential of the skew-quadrupole kicks already has a complete Fourier form if one inserts the action-angle variables into (3.7). For the calculation of the Fourier series corresponding to the beam-beam potential (3.6), one calculates the Fourier coefficients using a Fourier transformation. In principle, the integral in (3.6) can be evaluated analytically, yielding a generalized hypergeometric series of the second kind ${}_2F_2(a,b;c,d;z)$ [58]. However, because there is no look-up table for such a series, the series must be numerically evaluated. Therefore, instead of taking the detour over the generalized hypergeometric series, the Fourier coefficients are directly calculated by integrating the integral in (3.6) numerically and using a Fast Fourier Transform (FFT) with respect to the angle variables in (3.9). The calculation of a complete Fourier presentation of the sextupole potential (3.5) requires perturbation theory. To this end, the tune modulation must be first eliminated from the linear part of (3.8). Introducing the vectors $\vec{n} = (n_1, n_2, ..., n_N)$, $\vec{f}_{mod} = (f_{mod,1}, f_{mod,2}, ..., f_{mod,N})$, and using a canonical transformation defined by the mixed variable generating function [18]

$$F_2 = \tilde{I}_x \cdot \left[\phi_x - \sum_{p=1}^{N} \frac{\triangle Q_{x,p} f_{rev}}{f_{mod,p}} \cdot \sin\left(\frac{2\pi f_{mod,p}}{L f_{rev}} \cdot s \right) \right], \tag{3.11}$$

in order to eliminate the tune modulation from the linear part of (3.8) one can use Deprit perturbation theory [59][13] for the calculation of the mode amplitudes of the sextupole potential (3.5). Neglecting the tilde on the new variables in (3.11), one gets finally for the Fourier presentation of (3.8)

$$\begin{aligned} H = {} & \nu_x \cdot I_x + \nu_z \cdot I_z + \qquad (3.12) \\ & \sum_{l,m,k,\vec{n}} \left[\prod_{p=1}^{N} J_{n_p}\left(\frac{l \triangle Q_{x,p} f_{rev}}{f_{mod,p}} \right) \right] \cdot \left\{ A_{l,m,k}(I_x, I_z) \cdot \cos\left(l\phi_x + m\phi_z + \frac{2\pi}{L}\left(k + \frac{\vec{n}\cdot\vec{f}_{mod}}{f_{rev}} \right) \cdot s \right) + \right. \\ & \left. B_{l,m,k}(I_x, I_z) \cdot \sin\left(l\phi_x + m\phi_z + \frac{2\pi}{L}\left(k + \frac{\vec{n}\cdot\vec{f}_{mod}}{f_{rev}} \right) \cdot s \right) \right\}. \end{aligned}$$

where $J_{n_p}(l \triangle Q_{x,p} f_{rev}/f_{mod,p})$ are the Bessel functions of the first kind. In the following, the Fourier modes are labeled by the index triplet (l,m,k). The Fourier coefficients are composed by the skew-quadrupole, the sextupole, and the beam-beam contributions

$$\begin{aligned} A_{l,m,k}(I_x, I_z) &= A^{skew}_{l,m,k}(I_x, I_z) + A^{beam-beam}_{l,m,k}(I_x, I_z) + A^{sext}_{l,m,k}(I_x, I_z) \qquad (3.13) \\ B_{l,m,k}(I_x, I_z) &= B^{skew}_{l,m,k}(I_x, I_z) + B^{beam-beam}_{l,m,k}(I_x, I_z) + B^{sext}_{l,m,k}(I_x, I_z). \end{aligned}$$

There is a very important difference between the mode amplitudes of the magnetic multipole errors and the mode amplitudes of the beam-beam potential (3.6). While the mode amplitudes of the skew quadrupole and the sextupole kicks increase polynomally with increasing actions, the mode amplitudes of the beam-beam potential ultimately vanish for very large actions [57]. On the other hand, for small actions the mode amplitudes of the beam-beam potential are large compared to the mode amplitudes of the magnetic multipole errors [60]. Hence, while the magnetic multipole errors are particularly important for determining the dynamic

aperture at large action values, it is the mode amplitudes of the beam-beam interaction which are particularly important for calculating the drift and diffusion coefficients during the luminosity runs. For the sake of simplicity, the analysis of the dynamic aperture in Section (7) is therefore limited to sextupole kicks only and the discussion of the drift and diffusion coefficients in Section (9) is limited to mode amplitudes of the beam-beam interaction only.

But before the resonance structure of (3.12) is investigated in more detail, the non-linear map corresponding to (3.8) is first constructed and the concept of a surface of section (SoS) [11][13][14] is introduced.

3.2 Nonlinear Mapping

In this section, the one-turn-map corresponding to the Hamilton function (3.8) is constructed. The map will be used for a numerical simulation of the particle dynamics, as it is required for the construction of the surfaces of section [11][13][14] (SoS) and for the numerical calculation of the diffusion and drift coefficients.

The equation of motion corresponding to the linear part of the Hamilton function (3.8) can be integrated, yielding

$$\begin{aligned} I_z(s_0 + hL + \triangle L) &= I_z(s_0 + hL), \quad & \phi_z(s_0 + hL + \triangle L) &= \phi_z(s_0 + hL) + \triangle_z(\triangle L), \qquad (3.14) \\ I_x(s_0 + hL + \triangle L) &= I_x(s_0 + hL), \quad & \phi_x(s_0 + hL + \triangle L) &= \phi_x(s_0 + hL) + \triangle_x(s_0 + hL, \triangle L), \end{aligned}$$

with

$$\begin{aligned} \triangle_z(\triangle L) &= \nu_z \cdot \triangle L, \qquad (3.15) \\ \triangle_x(s_0 + hL, \triangle L) &= \nu_x \triangle L + \\ & \sum_{p=1}^{N} \left[\frac{2\triangle Q_{x,p} f_{rev}}{\pi f_{mod,p}} \sin\left(\frac{f_{mod,p} \triangle L}{L f_{rev}} \right) \cos\left(\frac{2\pi f_{mod,p} h}{f_{rev}} + \frac{\pi f_{mod,p} \cdot (2s_0 + \triangle L)}{L f_{rev}} \right) \right]. \end{aligned}$$

Taking into account the nonlinear kicks corresponding to (3.5) and (3.6), and the linear skew-quadrupole kicks, the position after the $(h+1)^{th}$ passage through the model ring can be expressed as a function of the position after the h^{th} passage through the model ring. While the symplectic skew-quadrupole and sextupole kicks can be directly calculated from (3.5) and (3.7) using

$$\triangle p_y = -\int_{L_0-\epsilon}^{L_0+\epsilon} \frac{\partial V(x,z)}{\partial y} ds, \quad y = x, z, \tag{3.16}$$

the calculation of the beam-beam kicks is more complicated. For the beam-beam potential (3.6) Equation (3.16) yields for the horizontal beam-beam kick [57]

$$\triangle p_x = -\frac{2N_b r_p \cdot (x - d_x)}{\gamma_p} \cdot \int_0^\infty \frac{\exp\left(-\frac{(x-d_x)^2}{2\sigma_x^2+q} - \frac{(z-d_z)^2}{2\sigma_z^2+q} \right)}{(2\sigma_x^2+q)^{3/2} \cdot (2\sigma_x^2+q)^{1/2}} dq. \tag{3.17}$$

The vertical kick has the same form but with x and z exchanged. In the limit of round beams with $\sigma_x = \sigma_z$, equation (3.17) yields for $(d_x = 0 = d_z)$

$$\triangle p_y = -\frac{2N_b r_p y}{\gamma_p r^2} \cdot \left[1 - \exp\left(-\frac{r^2}{2\sigma^2} \right) \right], \quad y = x, z,$$

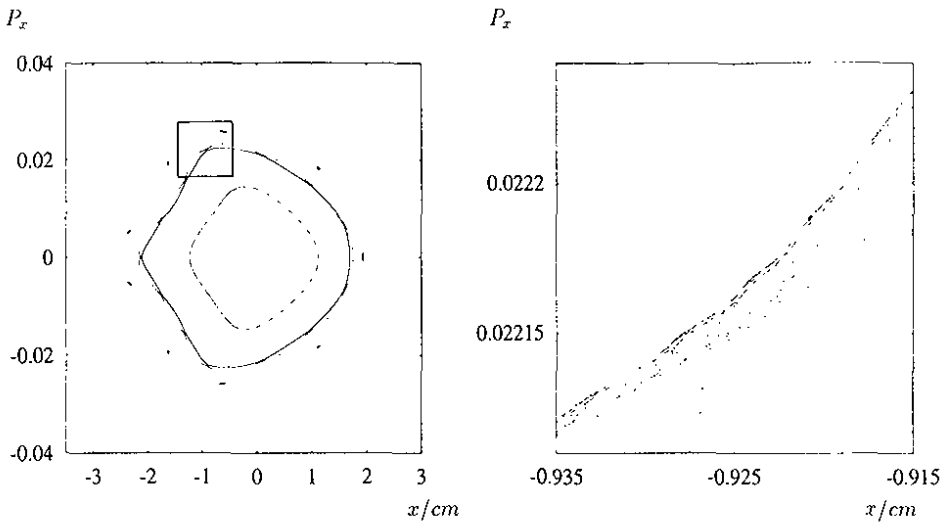

Figure 3.1:
Left: The surfaces of section without tune modulation in the P_x and x variables for a purely horizontal particle motion ($p_z \equiv 0, z \equiv 0$) in the HERA-p FODO cell [62]. One clearly recognizes the island chains of the $(9, 0, -281)$ and $(13, 0, -406)$ resonance.
Right: Enlargement of the hyperbolic fixed point of the $(13, 0, -406)$ resonance that lies inside the framed box. The ergodic character of the particle motion near the separatrix of the $(13, 0, -406)$ resonance is clearly recognizable.

with ($r^2 = x^2 + z^2$). For flat beams, the integral in (3.17) can be evaluated in terms of the complex error function [61]. Unfortunately, the numerical particle tracking with a map that requires an evaluation of the complex error function after each iteration is much too slow for a numerical simulation of the particle dynamics within a reasonable period of time.

In order to achieve reasonable tracking times, one has to approximate the beam-beam kick with an expression that allows a fast calculation of the kicks. There are three different possibilities for approximating the beam-beam kick for flat beams. First, one can try to calculate the integral in (3.17) numerically. But the numerical evaluation of (3.17) to a sufficient accuracy turns out to be as time consuming as a direct call of a library routine for the complex error function. Alternatively, one can try to calculate the complex error function for a finite set of coordinates in the beginning of the particle tracking and to interpolate the kick strength from a two-dimensional table during the tracking. While the method has been successfully used in the simulations of the beam-beam interaction in e^+/e^- colliders, it can not be used in the simulation of the beam-beam interaction in proton storage rings. Because the interpolation method leads to small discontinuities in the derivatives of the kicks with respect to the coordinates, the method can lead to an artificial damping of the proton dynamics ('grid-noise').

In this thesis, the beam-beam kick for flat beams is evaluated using a Padé approximation for the complex error function [58][9] (see Appendix (A)). The Padé approximation allows a calculation of the beam-beam kicks within a reasonable amount of time and yields an

expression which is continuous in the derivatives with respect to the particle coordinates up to arbitrary order. Transforming back to the variables x, P_x, z, and P_z, the non-linear map corresponding to (3.8) consists of the linear transfer maps

(3.18.*a*)

$$\begin{pmatrix} x \\ P_x \\ z \\ P_z \end{pmatrix}_{s_0+h\cdot L+\Delta L} = \begin{pmatrix} \cos(\Delta_x) & \beta_x \cdot \sin(\Delta_x) & 0 & 0 \\ -\sin(\Delta_x)/\beta_x & \cos(\Delta_x) & 0 & 0 \\ 0 & 0 & \cos(\Delta_z) & \beta_z \cdot \sin(\Delta_z) \\ 0 & 0 & -\sin(\Delta_z)/\beta_z & \cos(\Delta_z) \end{pmatrix} \cdot \begin{pmatrix} x \\ P_x \\ z \\ P_z \end{pmatrix}_{s_0+h\cdot L}$$

the sextupole kicks

$$\begin{pmatrix} x \\ P_x \\ z \\ P_z \end{pmatrix}_{s_0+h\cdot L+L_1+\epsilon} = \begin{pmatrix} x \\ P_x \\ z \\ P_z \end{pmatrix}_{s_0+h\cdot L+L_1-\epsilon} + \begin{pmatrix} 0 \\ -\frac{\lambda}{2}\cdot(x^2-z^2) \\ 0 \\ \lambda \cdot x \cdot z \end{pmatrix}_{s_0+h\cdot L+L_1-\epsilon} \qquad (3.18.b)$$

the skew-quadrupole kicks

$$\begin{pmatrix} x \\ P_x \\ z \\ P_z \end{pmatrix}_{s_0+h\cdot L+L_1+\epsilon} = \begin{pmatrix} x \\ P_x \\ z \\ P_z \end{pmatrix}_{s_0+h\cdot L+L_1-\epsilon} + \begin{pmatrix} 0 \\ -k_s \cdot z \\ 0 \\ -k_s \cdot x \end{pmatrix}_{s_0+h\cdot L+L_1-\epsilon} \qquad (3.18.c)$$

and the beam-beam kicks

(3.18.*d*)

$$\begin{pmatrix} x \\ P_x \\ z \\ P_z \end{pmatrix}_{s_0+h\cdot L+L_1+\epsilon} = \begin{pmatrix} x \\ P_x \\ z \\ P_z \end{pmatrix}_{s_0+h\cdot L+L_1-\epsilon} + \begin{pmatrix} 0 \\ -\frac{N_b r_p}{\gamma_\epsilon}\cdot\frac{x}{r^2}\cdot[1-\exp(-r^2/2\sigma^2)] \\ 0 \\ -\frac{N_b r_p}{\gamma_\epsilon}\frac{z}{r^2}\cdot[1-\exp(-r^2/2\sigma^2)] \end{pmatrix}_{s_0+h\cdot L+L_1-\epsilon}$$

For flat beams, the Padé approximation given in Appendix (A) must be used for the beam-beam kicks.

The combined map will be used for the construction of the surface of section (SoS) [11][13] and for the numerical tracking of particle distributions in the phase space of (3.8).

The surface of section depicts the particle coordinates at the intersection points of the particle trajectory with a given surface in the phase space. The following analysis uses the surface $mod(s, \kappa \cdot L) = 0$ for the surface of section, with $\kappa \in \mathbf{Z}$ imposed by the map (3.18). In the case of a quasi periodic, bounded particle motion, the particle trajectory intersects the surface of section repeatedly and the positions of the intersection points reflect the resonance structure in the phase space. A short summary of the main concepts of the SoS follows. A thorough description of the SoS can be found in [13] and [14].

Looking at a four-dimensional phase space, the intersection points of a trajectory which corresponds to a regular particle motion lie on a closed curve in the SoS. For a particle

motion on a resonance, the resonance structure can be recognized by the appearance of a set of stable and unstable fixed points. In the direct neighbourhood of the stable fixed points, the intersection points lie on a set of closed curves around each stable fixed point. These islands are enclosed by the separatrix of the resonance, which connects all the unstable fixed points of the resonance and forms the boundary between rotation and libration [13]. The left-hand side of Fig.3.1 illustrates the appearance of such island chains for the purely horizontal particle motion ($I_z \equiv 0$) in the FODO cell of the proton storage ring in HERA. For the purely horizontal particle motion, the corresponding phase space has three dimensions. Two dimensions correspond to the horizontal action-angle variables and one dimension comes from the explicit dependence of the nonlinear potentials on the arc-length s. The nonlinear fields are generated by the sextupole correction coils in the main dipoles [62]. One clearly recognizes the 13 islands corresponding to the horizontal $(13, 0, -406)$ resonance and the 9 islands corresponding to the $(9, 0, -281)$ resonance. The particle motion near the separatrix of the $(9, 0, -281)$ resonance is unbound, and the particles are quickly lost.

The intersection points of a trajectory which corresponds to an irregular particle motion do not lie on closed curves in the SoS. Because of the ergodic character of the irregular particle motion, the intersection points cover an area with non-vanishing measure in the SoS. The right-hand side of Fig.3.1 illustrates the ergodicity of the particle motion near a hyperbolic fixed point of the $(13, 0, -406)$ resonance. Here, the intersection points clearly do not lie on a single curve, but cover an area with non-vanishing measure. Thus, the SoS allows a clear distinction between regular and irregular particle motion.

In the case of systems with more than two degrees of freedom, the intersection points of a regular trajectory with the SoS do not necessarily lie on a closed curve in the SoS. However, the arrangement of the intersection points can still reflect the resonance structure of the phase space and show resonance islands for a particle motion on a non-linear resonance. By allowing a clear distinction between regular and irregular particle motion, the SoS plays an important role in the following analysis of the non-linear particle dynamics.

For the construction of the SoS in the case of a harmonic tune modulation, one has to limit the tune modulation to frequencies that satisfy the resonance condition

$$\kappa \cdot f_{rev} + \vec{\delta} \cdot \vec{f}_{mod} = 0, \qquad \kappa, \delta_p \in \mathbf{Z}, \quad p = 1, 2, ..., N \rightarrow \frac{f_{mod,p}}{f_{rev}} = \frac{q}{r}, \; q, r \in \mathbf{Z}. \tag{3.19}$$

Rather than taking the particle coordinates after each passage through the model storage ring, as in the case without tune modulation, one takes the coordinates now only after each κ^{th} passage through the model ring, with κ being the smallest common denominator of the modulation frequencies $f_{mod,p}$. Without this restriction, one can only construct a stroboscopic phase space projection, which does not depict the clear resonance island structure.

The Hamilton function (3.12) of the model structure has two degrees of freedom plus an explicit time dependence, leading to a five-dimensional phase space. Hence, its phase space structure is rather complicated and heuristic criteria for the onset of irregular particle motion would be helpful for the diffusion analysis. Such a criterion, the 'overlap criterion of neighbouring resonances' was proposed by Chirikov [36] and will be introduced in the next chapter.

Section 4

Criteria for the Onset of Irregular Particle Motion

For an analysis of the particle diffusion due to the irregular aspects of the particle motion, it is necessary to have criteria for the onset of irregular motion in perturbed integrable systems. This section will briefly summarize the main concepts of such criteria and illustrate how they can be applied to the Hamiltonian (3.12). The starting point of all methods is to approximate the system near a resonance by a single resonance Hamiltonian and to reintroduce the other Fourier components as a perturbation to this Hamiltonian.

4.1 The Single Resonance Approximation

In order to apply the criteria for irregular particle motion to the particle motion in storage rings, the Hamilton function (3.12) is expressed as a sum of an integrable non-linear Hamiltonian and a small perturbation. Introducing the notation

$$\delta_{l,m,k} = \begin{cases} \arctan\left(\frac{A_{l,m,k}}{B_{l,m,k}}\right) + \frac{\pi}{2} & \text{for } B_{l,m,k} \geq 0 \\ \arctan\left(\frac{A_{l,m,k}}{B_{l,m,k}}\right) - \frac{\pi}{2} & \text{for } B_{l,m,k} < 0 \end{cases} \tag{4.1}$$

and

$$\epsilon V_{l,m,k,\vec{n}} = \left[\prod_{p=1}^{N} J_{n_p}\left(\frac{l \triangle Q_{x,p} f_{rev}}{f_{mod,p}}\right)\right] \cdot \sqrt{A_{l,m,k}^2 + B_{l,m,k}^2} \tag{4.2}$$

one can write (3.12) in the form

$$H(I_x, I_z, \phi_x, \phi_z, s) = H_0(I_x, I_z) - \epsilon \sum_{l,m,k,\vec{n}} V_{l,m,k,\vec{n}} \cdot \cos\left(l\phi_x + m\phi_z + \frac{2\pi}{L}\left(k + \frac{\vec{n}\vec{f}_{mod}}{f_{rev}}\right) \cdot s + \delta_{l,m,k}\right) \tag{4.3}$$

with

$$H_0(I_x, I_z) = \nu_x \cdot I_x + \nu_z \cdot I_z + A_{0,0,0}(I_x, I_z). \tag{4.4}$$

The effect of a perturbation Fourier component in (4.3) becomes stronger, the slower the time variation of the phase

$$\psi_{l,m,k,\vec{n}} = l\phi_x + m\phi_z + \frac{2\pi}{L} \cdot \left(k + \frac{\vec{n} \cdot \vec{f}_{mod}}{f_{rev}}\right) \cdot s. \tag{4.5}$$

In the limiting case of a constant phase, one arrives at a resonance:

$$l \cdot \frac{\partial H_0}{\partial I_x} + m \cdot \frac{\partial H_0}{\partial I_z} + \frac{2\pi}{L} \cdot \left(k + \frac{\vec{n} \cdot \vec{f}_{mod}}{f_{rev}} \right) = 0. \tag{4.6}$$

Assuming that the resonance condition (4.6) is only fulfilled by one Fourier mode, and that all the non-resonant phases are rapidly oscillating functions of s, the non-resonant Fourier components in the neighbourhood of the resonance (4.6) can be neglected and one can approximate (4.3) with the single resonance Hamiltonian

$$\begin{aligned} H_{res}(I_x, I_z, \phi_x, \phi_z, s) &= H_0(I_x, I_z) \\ &\quad - \epsilon \cdot V_{l,m,k,\vec{n}} \cdot \cos\left(l\phi_x + m\phi_z + \frac{2\pi}{L} \left(k + \frac{\vec{n} \cdot \vec{f}_{mod}}{f_{rev}} \right) \cdot s + \delta_{l,m,k} \right). \end{aligned} \tag{4.7}$$

Using such a 'averaging method' [63], one obtains the 'single resonance approximation' [13]. However, this approximation is only applicable for a 'moderate non-linearity' of the integrable Hamiltonian H_0 [36]. The condition for 'moderate non-linearity' can be best expressed in terms of resonance variables. For $l, m \neq 0$ the resonance variables I_+ and ψ_+ are defined by a canonical transformation using the mixed variable generating function

$$F_2 = I_+ \cdot \left(l\phi_x + m\phi_z + \frac{2\pi}{L} \cdot \left[k + \frac{\vec{n} \cdot \vec{f}_{mod}}{f_{rev}} \right] \cdot s + \delta_{l,m,k} \right) + I_- \cdot (l\phi_x - m\phi_z), \tag{4.8}$$

and take the form

$$I_+ = \frac{mI_x + lI_z}{2lm}, \qquad \psi_+ = l\phi_x + m\phi_z + \frac{2\pi}{L} \cdot \left[k + \frac{\vec{n} \cdot \vec{f}_{mod}}{f_{rev}} \right] \cdot s + \delta_{l,m,k}, \tag{4.9}$$

$$I_- = \frac{mI_x - lI_z}{2lm}, \qquad \psi_- = l\phi_x - m\phi_z. \tag{4.10}$$

In terms of the resonance variable I_+, the condition for 'moderate non-linearity' can be written as

$$\epsilon \ll \alpha \ll \frac{1}{\epsilon} \cdot \left[\frac{\omega_{r,t,k,\vec{n}}}{\omega_0} \right]^2, \tag{4.11}$$

where α is the non-linearity parameter [36]

$$\alpha = \frac{I_+}{\omega_0} \cdot \frac{\partial \omega_0}{\partial I_+}, \tag{4.12}$$

and where

$$\omega_0 = l\frac{\partial H_0}{\partial I_x} + m\frac{\partial H_0}{\partial I_z}, \quad \omega_{r,t,k,\vec{n}} = r\frac{\partial H_0}{\partial I_x} + t\frac{\partial H_0}{\partial I_z} + \frac{2\pi}{L} \left(k + \frac{\vec{n} \cdot \vec{f}_{mod}}{f_{rev}} \right); r \neq l, t \neq m. \tag{4.13}$$

In (4.11) it was assumed that the small parameter ϵ is adjusted in such way that $V_{l,m,k,\vec{n}} \sim I_+ \cdot \omega_0$.

The condition for 'moderate non-linearity' puts two restrictions on the non-linearity parameter (4.12). On the one hand, the condition requires a sufficiently large non-linearity,

which ensures a stabilization of the particle motion on the resonance. Due to this 'non-linear stabilization', the resonance covers only a finite fraction of the phase space. On the other hand, the non-linearity must not be too large, because a sufficiently small non-linearity is the prerequisite for the validity of the 'averaging method' [36].

As the Hamilton function for the particle motion in a storage ring corresponds to a perturbed linear system, the condition of 'moderate non-linearity' (4.11) imposes a severe condition on the applicability of the 'single resonance approximation' for (3.12). For this reason, one must carefully analyze the applicability of the single resonance approximation and see whether the approximated Hamiltonian still corresponds to the original system. In the following analysis, the validity of the single resonance approximation is checked by comparing the analytical estimates for the fixed point positions and the resonance widths with the numerical tracking results.

Assuming the applicability of the single resonance approximation (4.7), one can transform (4.7) to the resonance variables (4.9) and expand the Hamilton function into a Taylor series around the resonance values $I_{+,res}$ and $I_{-,res}$ of the action variables. Neglecting the constant terms and the derivatives of the potential with respect to the action variable I_+, one obtains the Hamilton function of a standard pendulum and the region of a non-linear resonance in phase space corresponds to the phase space of a standard pendulum, i.e., a restricted oscillation of the resonance variables I_+ and ψ_+:

$$H_{res} = \frac{1}{2} G \cdot p^2 - F \cdot \cos(\psi_+), \tag{4.14}$$

with

$$G := \frac{\partial^2 H_0}{\partial I_+^2}(I_{+,res}, I_{-,res}), \quad F := \epsilon V_{l,m,k,\vec{n}}(I_{+,res}, I_{-,res}), \quad p := (I_{+,res} - I_+).$$

In the neighbourhood of the stable fixed point ($\psi_+ = 0.0$), the action-angle variables oscillate with the 'free island oscillation frequency' ω_I

$$\omega_I = \sqrt{\frac{\partial^2 H_0}{\partial I_+^2}(I_{+,res}, I_{-,res}) \cdot \epsilon V_{l,m,k,\vec{n}}(I_{+,res}, I_{-,res})} \tag{4.15}$$

around the stable fixed point, and in the (I_+, ψ_+) phase space, the motion leads to resonance islands, which attain their maximum size at the separatrix of the pendulum motion. In terms of the action variable I_+, the maximum half width of the resonance island is

$$\Delta_{1/2} I = \sqrt{\frac{4\epsilon V_{l,m,k,\vec{n}}(I_{+,res}, I_{-,res})}{\frac{\partial^2 H_0}{\partial I_+^2}}}. \tag{4.16}$$

4.2 Converse KAM Theorem

It seems at first glance that while a system is near one particular resonance and the other perturbation terms are non-resonant, the system has an integrable Hamiltonian and is completely regular. However, the single resonance approximation (4.7) is only precise to a certain accuracy. In general, the non-resonant perturbation terms in (4.3) can not simply be neglected.

A more precise formulation of the averaging method uses an infinite sequence of canonical variable transformations for the elimination of the non-resonant Fourier components [36][13]. In such a perturbative formulation of the averaging method, the question of regular motion corresponds to the question of convergence in the sequence of variable transformations. The KAM theorem [15][16][17] states that for sufficiently small perturbations invariant surfaces exist for most initial conditions. However, there might also exist initial conditions for which the sequence of variable transformations does not converge and where no KAM surface exists. As the disappearance of invariant KAM surfaces is related to the onset of ergodic particle motion [35][64] a 'converse KAM theorem' which states the conditions under which the invariant KAM surfaces disappear would be useful for the analysis of the particle motion in non-linear systems. Such a 'converse KAM theorem' was first formulated for the area preserving 'standard map' [35][64][65][66][67]. Reintroducing the neglected non-resonant Fourier components as a perturbation to the single resonance Hamiltonian

$$H(p,\psi,s) = \frac{1}{2}G\cdot p^2 - F\cdot\cos\psi_+ + \epsilon\cdot\sum_{(r,t,u)\neq(l,m,k)} U_{r,t,u}(I_+,I_-,\psi_+,\psi_-,s), \qquad (4.17)$$

the motion near the pendulum separatrix can be locally approximated by the standard map

$$\begin{aligned} I_{n+1} &= I_n + K\cdot\sin\theta_n \qquad (4.18)\\ \theta_{n+1} &= \theta_n + I_{n+1}, \end{aligned}$$

where I corresponds to the relative oscillation energy of the pendulum and θ to the phase of the perturbing Fourier components. A detailed description of the approximation is given in Section (5.2). The pendulum motion is said to be globally stochastic if the relative oscillation energy of the pendulum changes from a bounded local oscillation to an unbounded motion. The mapping of Equation (4.18) is invariant under the transformations

$$\dot{I} = I + 2\pi, \qquad \dot{\theta} = \theta + 2\pi \qquad (4.19)$$

so that the phase space can be wrapped on the torus $0 \le I < 2\pi$, $0 \le \theta < 2\pi$.

In the absence of invariant surfaces, adjacent hyperbolic fixed points of the perturbed system are not connected by a smooth separatrix. Rather, the outgoing and incoming trajectories of two adjacent hyperbolic fixed points intersect infinitely often, leading to a homoclinic tangle of the trajectories. The intersection points are called homoclinic points [13][14] and the extraordinarily complicated motion resulting from the existence of homoclinic points leads to the generation of stochasticity near the separatrix of the unperturbed system [68][34][14][69][13]. The converse KAM theorem gives a criterion for the disappearance of all invariant circles and thus, for the onset of a global stochasticity in the standard map. The theorem states that the map has no invariant surface for parameter values K with [65]

$$|K| \ge \frac{63}{64} = 0.984375. \qquad (4.20)$$

This result agrees extremely well with the numerical work of Greene [35], which suggests a value of

$$K_c \sim 0.971635. \qquad (4.21)$$

Using the 'residue criterion', Greene also showed that there is at least one KAM surface for $|K| < K_c$. Fig.4.1 illustrates the converse KAM theorem for the standard map.

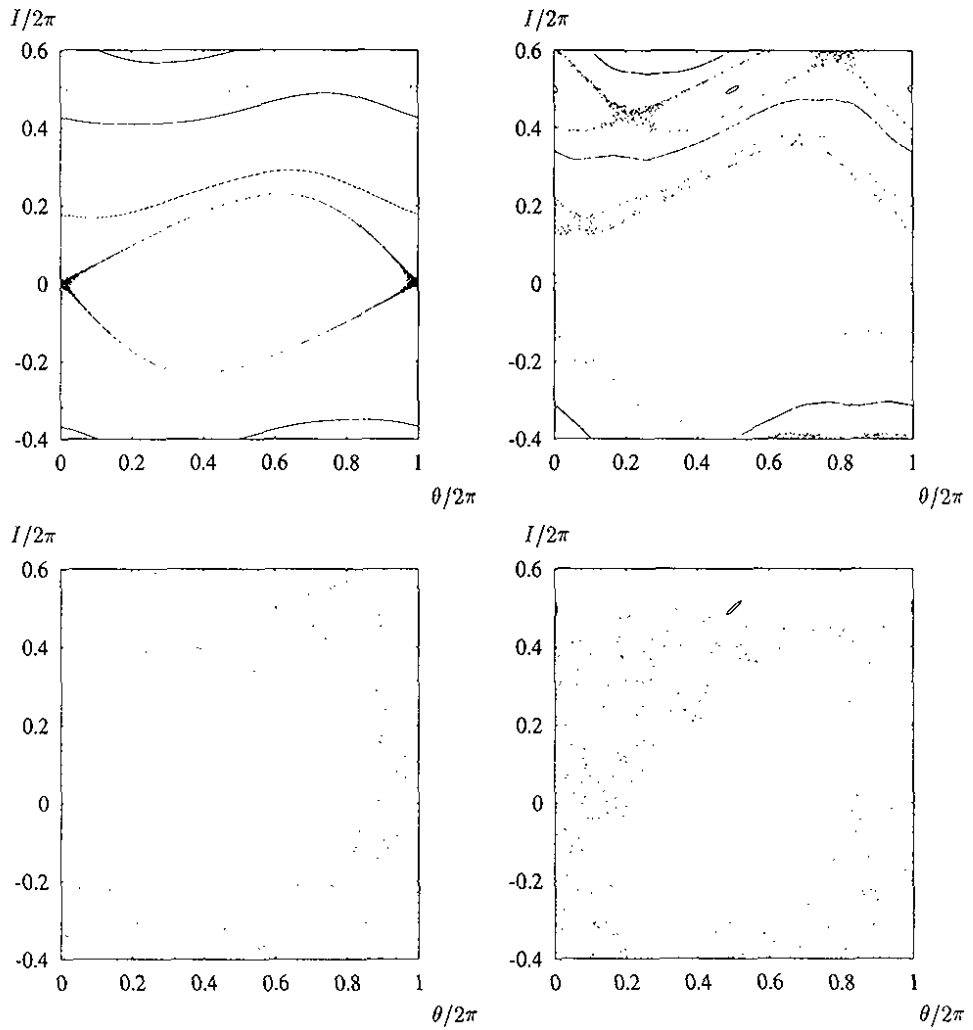

Figure 4.1:
Top: Five orbits of the standard map for two different parameter values K:
Left: $K = 0.5$.
Right: $K = 0.97$.
Bottom: One orbit of the standard map for two different parameter values K:
Left: $K = 0.99$.
Right: $K = 1.5$.
The transition from regular motion to global stochasticity for a parameter change from $K = 0.97$ to $K = 0.99$ is clearly recognizable.

The picture in the upper left corner of Fig.4.1 shows five orbits of the standard map for $K = 0.5$ and the picture in the upper right corner shows the orbits for $K = 0.97$. The picture in the lower left corner shows one orbit of the standard map for $K = 0.99$ and the picture in the lower right corner for $K = 1.5$. One clearly recognizes the transition from regular motion to global stochasticity for a parameter change from $K = 0.97$ to $K = 0.99$.

As long as rotational invariant circles exist, the I motion is limited to a subspace of the I domain. In the upper right corner of Fig.4.1 two invariant circles divide the I domain into two subspaces. One invariant circle starts at $(I \approx -0.3, \theta = 0.0)$ and the other circle starts at $(I \approx 0.35, \theta = 0.0)$. For $K > 63/64$, the invariant circles vanish and one trajectory can cover the whole I domain. The situation is illustrated in Fig.4.1. The picture in the lower left corner of Fig.4.1 shows one trajectory of the standard map with the initial conditions $(I_0 = 0.0027, \theta_0 = 0.0)$ which covers the whole I domain. Thus, treating the previously neglected non-resonant Fourier components of (4.3) as a perturbation to the single resonance approximation (4.14), one can use the converse KAM theorem for a quantitative estimate of the onset of irregular particle motion near the separatrix of the unperturbed Hamiltonian. The details of such an analysis are illustrated in Section (5.2). The main result of such an analysis is that no matter how small the perturbation, a domain with ergodic motion always exists sufficiently close to the separatrix of the unperturbed system. The domain is often called the 'stochastic layer' [13].

However, for small perturbations, the width of the stochastic layer might be small and invariant KAM surfaces continue to exist outside the stochastic layer. In the case of two-dimensional systems, the KAM surfaces outside the stochastic layer form an impenetrable barrier for the particle motion and limit the irregular motion to the stochastic layer. The right-hand side of Fig.3.1 shows the stochastic layer for the $(13, 0, -406)$ resonance of the HERA-p FODO cell with sextupole non-linearities in the two-dimensional subspace $(P_z \equiv 0 \equiv z)$. Compared to the accessible phase space, the size of the stochastic layer is small and the particle motion near the origin of the transverse phase space $(P_x = 0 = x)$ remains regular.

In the case of the full six-dimensional phase space for the particle motion in a storage ring, the KAM surfaces do not enclose the stochastic layers and the ergodic character of the particle motion inside the layer leads inevitably to a slow diffusion. However, the spread due to the Arnold diffusion occurs only slowly and is negligible as long as the stochastic layers are small.

4.3 The Overlap Criterion

A stochastic layer that covers a large fraction of the phase space and that leads to a fast particle diffusion might exist if the system has more than one strong resonance. In [36], Chirikov proposed a powerful approximate criterion for the existence of such a large stochastic layer in the case of two equally strong resonances. Introducing a second resonance to the Hamiltonian (4.7) one gets

$$\begin{aligned} H_{res}(I_x, I_z, \phi_x, \phi_z, s) &= H_0(I_x, I_z) \\ &\quad - \epsilon \cdot V_{l,m,k,\vec{n}} \cdot \cos\left(l\phi_x + m\phi_z + \frac{2\pi}{L}\left(k + \frac{\vec{n}\cdot\vec{f}_{mod}}{f_{rev}}\right)\cdot s + \delta_{l,m,k}\right) \\ &\quad - \epsilon \cdot V_{\tilde{l},\tilde{m},\tilde{k},\vec{n}} \cdot \cos\left(\tilde{l}\phi_x + \tilde{m}\phi_z + \frac{2\pi}{L}\left(\tilde{k} + \frac{\vec{n}\cdot\vec{f}_{mod}}{f_{rev}}\right)\cdot s + \delta_{\tilde{l},\tilde{m},\tilde{k}}\right). \end{aligned} \tag{4.22}$$

For the sake of simplicity, we assume

$$\left(\tilde{l}, \tilde{m}, \tilde{k}, \vec{\tilde{n}}\right) = \kappa \cdot \left(l, m, [k - \tilde{k}], \vec{n}\right). \tag{4.23}$$

and express the Hamilton function (4.22) in terms of the resonance variables (4.9):

$$H_{res} = \frac{1}{2}G \cdot p^2 - F \cdot \cos(\psi_+) - P \cdot \cos\left(\kappa\left[\psi_+ - \frac{2\pi}{L}\tilde{k}\cdot s\right]\right), \tag{4.24}$$

with

$$P := \epsilon \cdot V_{\tilde{l},\tilde{m},\tilde{k},\vec{\tilde{n}}}(I_{+,res}, I_{-,res}).$$

For $P = 0$, $F \neq 0$ one has again the pendulum Hamiltonian (4.14). The left-hand side of Fig.4.2 schematically shows the corresponding phase space structure in the (p, ψ_+) variables. For $P \neq 0$, $F = 0$ one obtains the Hamilton function of a particle in a longitudinal wave. Defining new variables (w, y) via a canonical transformation using the mixed variable generating function

$$\begin{aligned} F_2 &= \left(w + \frac{2\pi}{L}k\right)\cdot\left(\psi_+ - \frac{2\pi}{L}\tilde{k}\cdot s\right). \\ \rightarrow \quad & w = p - \frac{2\pi}{L}\tilde{k}, \quad y = \psi_+ - \frac{2\pi}{L}k\cdot s, \end{aligned} \tag{4.25}$$

one has again the Hamilton function of a pendulum

$$H(w, y) = \frac{1}{2}G \cdot w^2 - P \cdot \cos(\kappa y), \tag{4.26}$$

but this time the periodicity in y is $2\pi/\kappa$ and the resonance domain is moving with a velocity $2\pi\kappa \cdot \tilde{k}/L$ with respect to the ψ_+ axis. A simple way to visualize it in the variables (p, ψ_+), is to use a stroboscopic projection of the (w, y) trajectories, that shows the variables only at $s = n \cdot L$ $(n \in \mathbf{N})$ and that takes advantage of the 2π periodicity in ψ_+. (In other words, the map is wrapped onto a cylinder.) The right-hand side of Fig.4.2 schematically shows the corresponding phase space structure. The results from Section (4.1) yield for the resonance half-widths of the two resonances [Equation (4.16)]

$$\triangle_{1/2p} = \begin{cases} \sqrt{\frac{4\cdot F}{G}} & \text{for } P = 0 \text{ and } F \neq 0 \\ \sqrt{\frac{4\cdot P}{G}} & \text{for } P \neq 0 \text{ and } F = 0. \end{cases} \tag{4.27}$$

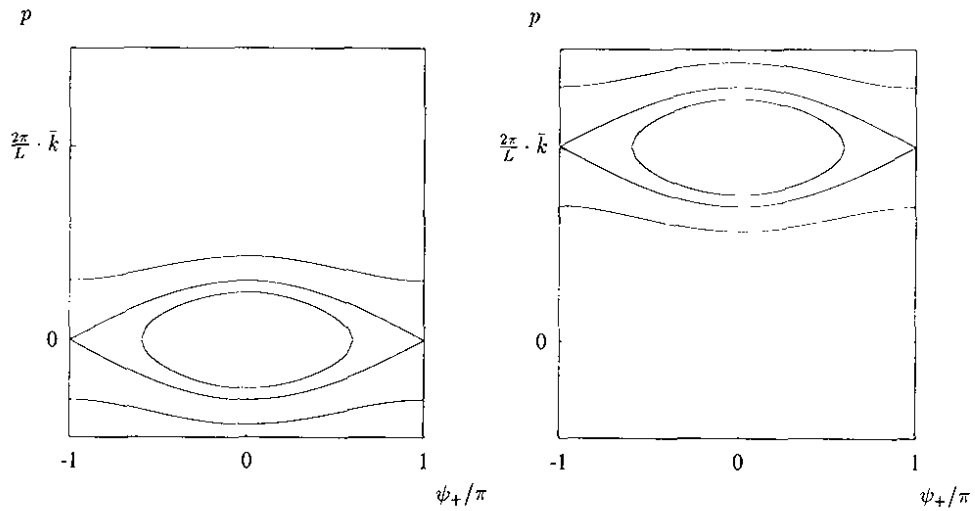

Figure 4.2:
Left: The phase space of the pendulum Hamiltonian for $P = 0$, $F \neq 0$.
Right: The phase space of a particle in a longitudinal wave $P \neq 0$, $F = 0$.

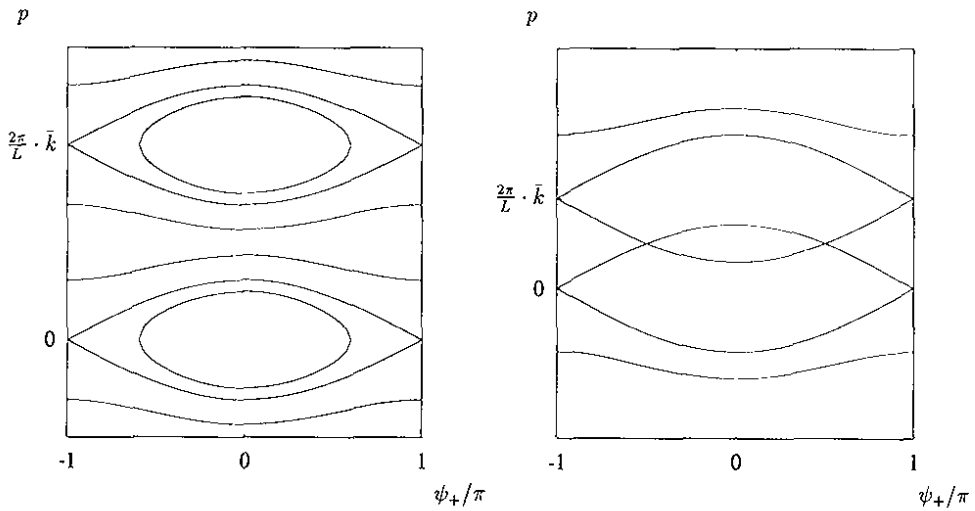

Figure 4.3:
Left: The phase space of two well-separated resonances.
Right: The phase space of two overlapping resonances.

When both F and P are non-zero, one can use Melnikov's method [13][70] for an analysis of the motion near the separatrices of the two resonances and show that the two-resonance system is non-integrable. However, one would intuitively expect that the surface of section of the two-resonance system looks like some kind of superimposition of the phase space portraits in Fig.4.2 if the two resonances are far from overlapping. Defining the 'overlap parameter' S [36] as the ratio between the sum of the half-widths (4.27) and the spacing between the two resonances, one would expect that for $S \ll 1$ the traces of passing tori are only slightly pinched between the two resonances and that invariant KAM surfaces continue to exist in the region between the two resonances. The left-hand side of Fig.4.3 illustrates this scenario. This simple picture is supported by the KAM theorem. Taking advantage of the 2π periodicity of the Hamiltonian (4.24) one can define a rotation number ρ for passing orbits as the average number of periods during the time period $T = L/(\kappa \cdot \bar{k})$

$$\rho = \frac{u \cdot T}{2\pi}, \tag{4.28}$$

where u is the average velocity of the particles

$$u = \lim_{T \to \infty} \frac{1}{T} \cdot \int_0^T p(s)ds. \tag{4.29}$$

For u or ρ irrational enough and $S > 0$ small enough, the set of trajectories characterized by u and ρ constitute a KAM torus [36][71]. The left-hand side of Fig.4.2 indicates the invariant torus corresponding to u as a straight line between the two resonances. The term 'irrational enough' corresponds to the Diophantine condition that there is a couple $(A > 0, \varepsilon)$, such that

$$\left|u - \frac{m}{n}\right| > \frac{A}{n^{2+\varepsilon}}, \tag{4.30}$$

for all $m, n \in \mathbf{Z}$.

On the other hand, if the overlap parameter S is larger than 1, the two resonances will overlap and the KAM torus between the two resonances will be destroyed. The right-hand side of Fig.4.3 shows the superimposition of the two pendulum phase spaces portraits for $S = 2/\sqrt{3}$. In this case, the simple superimposition of the two phase space portraits would be incorrect and the overlap of the two resonances results in a wide stochastic layer with ergodic particle motion. The critical value of S above which the invariant KAM surface disappears is $S = 2/\pi$, which is also called the 'two-thirds' rule [13]. The overlap criterion will be illustrated in Section (5), where the effect of an external tune modulation on the phase space structure is discussed. The particle diffusion due to such a wide stochastic layer is much faster than the 'Arnold diffusion' and can be fast enough to limit the stability time of the particle motion in a storage ring.

4.4 Renormalization Methods

A striking feature of the standard map is that it can be applied to describe its own motion near a resonance separatrix. The motion near one of the unstable fixed points of the standard map corresponds to the dynamics near a perturbed pendulum separatrix and can again be approximated by the standard map. This 'self-similarity' of the standard map is a generic property for non-linear dynamical systems and corresponds to the existence of infinitely nested subsystems near the separatrix of the unperturbed resonance [33][13][14]. Thus, non-linear systems are in some way scaling invariant. Magnifying the region between two resonance chains in the phase space portrait of a non-linear system results in new island chains. The important point of this magnification process is that the dynamics near the old and the new island chains are governed by the same paradigm Hamiltonian (4.24), differing only in the parameter values κ, $\bar{k}$, P and F. The idea of a renormalization method for describing the dynamics in such a nested system is to give an explicit rule for going from one system to the next nested one and to analyze whether the iterated process of rescaling the system preserves the invariant circle between neighbouring resonances. Thus the renormalization transform acts on the couple of a standard Hamiltonian and a KAM torus.

A thorough description of the renormalization theory for non-linear Hamilton systems will not be given here. For a detailed description of the renormalization theory we refer to the excellent review article by D.F. Escande [71] and to the original work in [72][73]. Rather, we want to emphasize its importance for a universal description of the onset of irregular particle motion in non-linear systems. While the converse KAM theorem of the standard map applies *only to the particle motion in the vicinity of a separatrix*, and while the overlap criterion applies only to the case of two approximate equally strong resonances, the renormalization approach offers a universal method for estimating the onset of irregular particle motion in non-linear two-dimensional Hamilton systems.

An accurate estimate of the transition to irregular particle motion using the renormalization method can be very difficult for complex systems, for example Hamilton systems with more than two degrees of freedom, and an analysis with the more graphic methods of the converse KAM theorem and the overlap criterion is much more convenient. Therefore, the following work will use the converse KAM theorem and the overlap criterion instead of the universal renormalization procedure. By comparing these criteria with the numerically determined surfaces of section, reasonably reliable quantitative estimates for the destruction of the KAM surfaces, and thus for the onset of irregular particle motion, can be obtained.

Section 5

The Effect of Tune Modulation on the Phase Space Structure

A first analysis of the particle diffusion due to the non-linear character of the particle dynamics showed that the diffusion rates in the HERA-p FODO cell without any tune modulation are negligible as long as the particle coordinates are within the accessible phase space of the HERA-p storage ring [62].

On the other hand, recent experiments at the Fermi National Accelerator Laboratory [7] and at the SPS at CERN [8] showed that an external tune modulation can drastically increase the particle diffusion and might limit the beam lifetime in the storage ring. Furthermore, R. Brinkmann [9] showed in a numerical simulation of the particle dynamics that a stochastic variation of the betatron tune as small as $\Delta Q = 10^{-4}$ in connection with the non-linear beam-beam interaction already leads to a serious emittance growth. All three examples for the increase of the particle diffusion due to an external tune modulation suggest a closer look at the effect of a tune modulation on the particle motion and the search for an analytical understanding of the causes for the emittance growth.

5.1 Modulation Sidebands

In the presence of a non-linear resonance, the tune modulation leads to a set of resonance sidebands around the primary resonance. Depending on the resonance strength and the modulation frequency and depth, the sidebands might overlap, leading to a wide stochastic layer. The various possibilities for such a resonance overlap are illustrated for a single resonance approximation of (4.3) with only one modulation frequency. The effect of a tune modulation with more than one modulation frequency will be discussed in Section (7). Assuming a constant resonance amplitude, a quadratic detuning term, and $I_z \equiv 0$ one has

$$\begin{aligned} H &= \frac{2\pi}{L} Q_x \cdot I_x + \frac{\pi}{L} \cdot A_{0,0,0} \cdot I_x^2 - \\ &\quad \frac{2\pi}{L} \sum_n \left[J_n \left(\frac{l \triangle Q_x f_{rev}}{f_{mod}} \right) \right] \cdot A_{l,0,k} \cdot cos \left(l\phi_x + \frac{2\pi}{L} \left(k + \frac{n f_{mod}}{f_{rev}} \right) \cdot s + \tau_0 \right). \end{aligned} \tag{5.1}$$

Without any tune modulation ($\triangle Q_x = 0$), the resonance condition can be written as

$$l \cdot Q_x + l \cdot A_{0,0,0} \cdot I_x + k = 0. \tag{5.2}$$

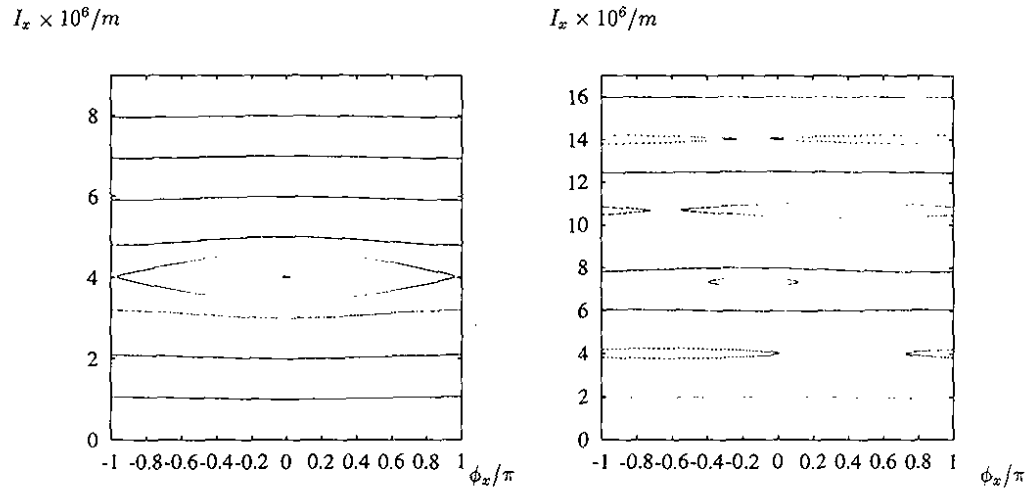

Figure 5.1:
The surfaces of section for the single resonance Hamiltonian.
Left: The surface of section without tune modulation.
Right: The surface of section for a fast tune modulation.

The left-hand side of Fig.5.1 shows the corresponding phase space for

$l = 1$	$k = -25$	$Q_x = 25.03$	$A_{0,0,0} = -7500.0m^{-1}$
$A_{1,0,-25} = 6.7 \cdot 10^{-10}m$	$L = 47 \cdot 10^2 m$	$f_{rev} = 61.3KHz$	

(5.3)

One clearly recognizes the island of the primary $(1, 0, -25)$ resonance. An additional tune modulation leads to resonance sidebands of the primary resonance in Fig.5.1. With tune modulation, the resonance condition reads

$$l \cdot Q_x + l \cdot A_{0,0,0} \cdot I_x + n \cdot \frac{f_{mod}}{f_{rev}} + k = 0. \tag{5.4}$$

Equation (5.4) shows that a slow tune modulation leads to a small, and that a fast tune modulation frequency leads to a large spacing of neighbouring sidebands. The right-hand side of Fig.5.1 shows the upper sidebands for a tune modulation with $f_{mod} = f_{rev}/40$ and $\Delta Q_x = 0.05$, where the sidebands are still well separated. The surface of section was constructed by numerically integrating the equations of motion with a variable-step Runge-Kutta algorithm [74]. In accordance with Equations (4.16) and (5.4), the sideband spacing and the maximum resonance half-width are

$$\Delta I_{res} \approx 3.5 \cdot 10^{-6}m, \qquad \Delta I_{1/2} \approx 0.6 \cdot 10^{-6}m, \tag{5.5}$$

and the overlap condition is not fulfilled. In this case, the tune modulation leads to a rich structure of resonance sidebands, but not to an extended irregular particle motion.

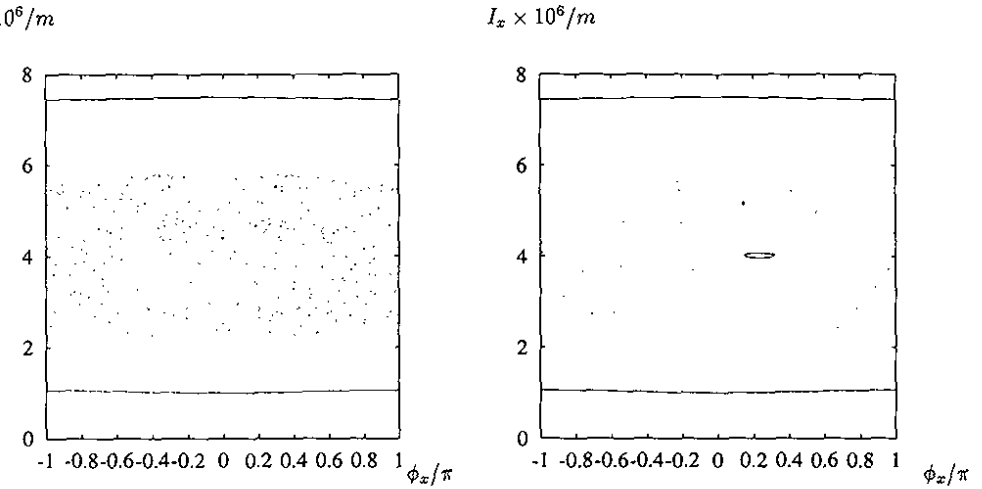

Figure 5.2:
The surfaces of section for the single resonance Hamiltonian.
Left: The surface of section for a slow tune modulation and sideband overlap ($f_{mod} = f_{rev}/2000, \Delta Q_x = 0.05$).
Right: The surface of section for a slow tune modulation and trapping ($f_{mod} = f_{rev}/4000, \Delta Q_x = 0.01$).

However, for a slow tune modulation, the overlap condition might be fulfilled, leading to irregular particle motion. For a slow tune modulation, the arguments of the Bessel functions become large and the Bessel functions may be approximated by their root-mean-square values for large arguments [58]

$$J_n(z) \approx \frac{1}{\sqrt{\pi z}}, \quad \text{for} \quad z \ll n. \tag{5.6}$$

With this approximation, the overlap condition for the modulation sidebands can be written as

$$16\pi^3 \cdot \frac{(A_{l,0,k} \cdot A_{0,0,0})^2}{l \Delta Q_x} \cdot \left(\frac{f_{rev}}{f_{mod}}\right)^3 > 1. \tag{5.7}$$

Thus, for the parameters (5.3) and a slow tune modulation with $\Delta Q_x = 0.05$ one expects a sideband overlap for modulation frequencies smaller than $f_{rev}/160$. The left-hand side of Fig.5.2 shows the surface of section for $f_{mod} = f_{rev}/2000$ and $\Delta Q_x = 0.05$. In this case, the tune modulation destroys the resonance structure of the primary resonance and forms a 'modulational layer' [54]. Inside the 'modulational layer' the irregular aspect of the particle motion can lead to a diffusion-like motion and to a reduction in the dynamic aperture. Both aspects of the motion inside the modulational layer will be discussed in the later sections.

Equation (5.7) indicates the formation of a modulational layer as long as the modulation frequency is sufficiently slow. However, the limit $f_{mod} \to 0$ does not always lead to a uniform modulational layer. In the limit $f_{mod} \to 0$ and constant modulation depth ΔQ_x, the chaotic

region of the modulational layer merges into a single-resonance layer and leaves a stable region around the stable fixed points of the seeding resonance [75][13]. In this case, the 'overlap criterion' (5.7) can not be applied. The region of regular particle motion is bounded by KAM tori [76] and oscillates inside the modulational layer. Because the particles inside this stable region can not leave the KAM tori, the phenomenon is called 'trapping' [75][77]. In comparison with the modulational diffusion [54], the single-resonance trapping layer corresponds to a much weaker diffusion. For one modulation frequency, the condition for trapping can be expressed as

$$l \cdot A_{l,0,k} \cdot A_{0,0,0} > \frac{\Delta Q_x f_{mod}}{f_{rev}}, \tag{5.8}$$

indicating trapping for a tune modulation with $\Delta Q_x = 0.01$ and $f_{mod} < f_{rev}/2000$. The right-hand side of Fig.5.2 shows the trapping phenomenon for a tune modulation with $\Delta Q_x = 0.01$ and $f_{mod} = f_{rev}/4000$. One clearly recognizes the region of regular particle motion inside the chaotic region of the modulational layer. For $f_{mod} = 0$, the single-resonance trapping layer disappears all together, and only the separatrix of the un-modulated primary resonance remains.

5.2 Stochastic Layer Width

In the direct neighbourhood of the stable fixed point of the primary resonance, the action-angle variables oscillate around the stable fixed point with the 'free island' oscillation frequency (4.15). With increasing distance from the stable fixed point, the oscillation frequency decreases and has a minimum for a particle motion inside the stochastic layer of the primary resonance. For the later analysis, it is convenient to express the 'free island' oscillation frequency in terms of the revolution frequency f_{rev} in the storage ring

$$\omega_I = 2\pi \cdot \frac{f_I}{f_{rev}}. \tag{5.9}$$

For the parameter values (5.3) the 'free island' oscillation frequency of the single resonance Hamiltonian becomes

$$\begin{aligned} f_I &= l \cdot f_{rev} \cdot \sqrt{A_{l,0,k} \cdot A_{0,0,0}} \\ f_I &\approx \frac{f_{rev}}{446} \end{aligned} \tag{5.10}$$

and a modulation frequency that satisfies

$$f_{mod} \lesssim N \cdot f_I, \quad N \in \mathbf{Z}, \tag{5.11}$$

is in resonance with the island oscillation frequency. Such a resonance will be called an N^{th}-order modulation resonance. The left-hand side of Fig.5.3 shows the first order modulation resonance for $f_{mod} = f_{rev}/560$ and $\Delta Q_x = 1.0 \cdot 10^{-5}$. Because the period of the island oscillation increases as the trajectory approaches the separatrix of the primary resonance ($\omega_I \to 0$)[13], the number of modulation resonance islands inside the primary resonance increases as well. In the vicinity of the separatrix, the resonance islands overlap and lead to a stochastic layer around the separatrix of the primary resonance. In the left-hand side of Fig.5.3 one clearly recognizes the stochastic layer around the separatrix of the unperturbed primary

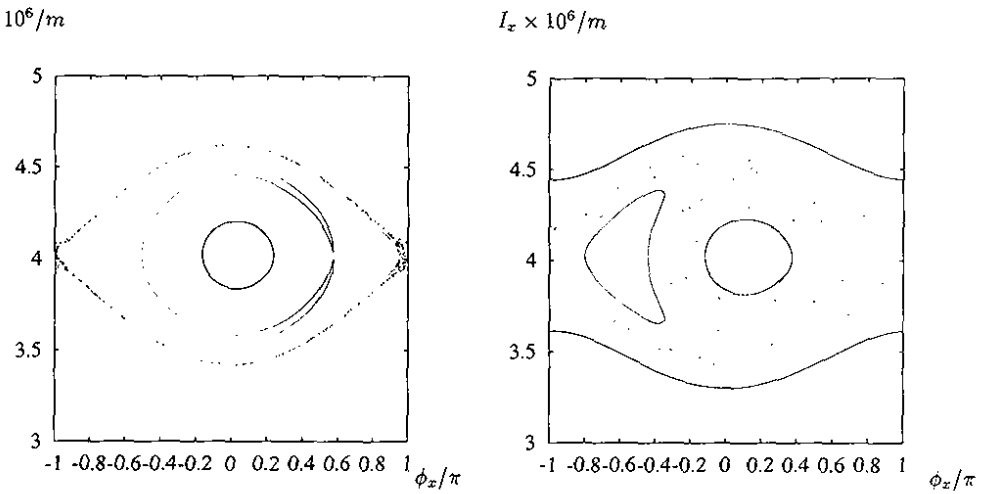

Figure 5.3:
The surfaces of section for the single resonance Hamiltonian.
Left: The surface of section for a tune modulation slightly above the 'free island' oscillation frequency with ($f_{mod} = f_{rev}/560, \Delta Q_x = 1.0 \cdot 10^{-5}$).
Right: The surface of section for a slow tune modulation slightly above the 'free island' oscillation frequency with ($f_{mod} = f_{rev}/560, \Delta Q_x = 3.0 \cdot 10^{-4}$).

resonance. If the modulation depth is increased, the island width of the modulation resonance also increases. For sufficiently large modulation depths, the first order modulation resonance becomes large enough to overlap with the separatrix of the primary resonance, leading to a wide stochastic layer. The right-hand side of Fig.5.3 shows the overlap of the first order modulation resonance with the separatrix of the primary resonance and the resulting wide stochastic layer for $f_{mod} = f_{rev}/560$ and $\Delta Q_x = 3.0 \cdot 10^{-4}$.

The width of the stochastic layer due to the external tune modulation can be estimated by dividing the Hamilton function into an integrable part and a small perturbation. In the following, the integrable part is given by the single resonance Hamiltonian and the perturbation term by the modulation sidebands. Calculating the change in the energy of the integrable part during the half period T of the phase oscillation inside the stochastic layer, one can approximate the motion inside the stochastic layer by the standard map [36]. The change in the unperturbed energy E_0 is given by

$$\Delta E_0 = \int_{-T/2}^{+T/2} ds \frac{\partial H}{\partial s} \tag{5.12}$$

$$= -\left(\frac{2\pi}{L}\right)^2 \cdot \sum_n \left(k + \frac{n f_{mod}}{f_{rev}}\right) \cdot \left[J_n\left(\frac{l \Delta Q_x f_{rev}}{f_{mod}}\right)\right] \cdot A_{l,0,k,n} \times \int_{-T/2}^{+T/2} ds \sin\left(l\phi_x + \frac{2\pi}{L}\left(k + \frac{n f_{mod}}{f_{rev}}\right) \cdot s + \tau_0\right). \tag{5.13}$$

One can evaluate the integral in (5.13) by approximating the motion of the angle variable inside the stochastic layer by the unperturbed motion on the pendulum separatrix

$$\phi_{sep}(s) = 4 \cdot \arctan\left[e^{\omega_I \cdot s}\right] - \pi \tag{5.14}$$

and extending the integrals in (5.13) from minus to plus infinity [36]. In this approximation, the integrals on the right-hand side of (5.13) are Melnikov-Arnold integrals (see Appendix B) and can be evaluated analytically. Defining the relative energy deviation from the separatrix energy as

$$W := \frac{E_{sep} - E_0}{E_{sep}}, \tag{5.15}$$

and taking only the first modulation sideband into account, the change in W per half period of the phase oscillation can be expressed as

$$\tilde{W} = W - \left(\frac{f_{mod}}{f_I}\right) \cdot \frac{J_{\pm 1}\left(\frac{l\Delta Q_x f_{rev}}{f_{mod}}\right)}{J_0\left(\frac{l\Delta Q_x f_{rev}}{f_{mod}}\right)} \cdot \mathcal{A}_2\left(\pm\frac{f_{mod}}{f_I}\right) \cdot \sin(\tau_0), \tag{5.16}$$

where $\mathcal{A}_2$ is the Melnikov-Arnold integral and can be written as (see Appendix B)

$$\mathcal{A}_2\left(\frac{f_{mod}}{f_I}\right) = 4\pi \cdot \left(\frac{f_{mod}}{f_I}\right) \frac{\exp\left[\frac{\pi f_{mod}}{2 f_I}\right]}{\sinh\left(\frac{\pi f_{mod}}{f_I}\right)}. \tag{5.17}$$

In order to construct a map for the change in W over one half-period of the phase oscillation inside the stochastic layer, one also needs the change in the phase τ_0, which is the canonical conjugate to W. The oscillation frequency in the vicinity of the perturbed separatrix is given by [36][13]

$$\omega = \frac{\pi \cdot \omega_I}{\ln(32/|W|)}, \tag{5.18}$$

and thus, one gets for the change in the phase τ_0

$$\tilde{\tau}_0 = \tau_0 + \left(\frac{f_{mod}}{f_I}\right) \cdot \ln\left(\frac{32}{\tilde{W}}\right). \tag{5.19}$$

Equations (5.16) and (5.19) describe the particle motion in the vicinity of the separatrix of the primary resonance. The corresponding map is called the 'whisker map' [36]. For

$$\tau_0 = n \cdot \pi, \qquad |\tilde{W}| = 32 \cdot \exp\left(-2\pi n \cdot \frac{f_I}{f_{mod}}\right) \tag{5.20}$$

the 'whisker map' has a resonance, and expanding the 'whisker map' around a fixed point (W_r, τ_r), one gets the standard map (ref. Section (4.2))

$$\begin{aligned} I_{n+1} &= I_n + K \cdot \sin\theta_n \\ \theta_{n+1} &= \theta_n + I_{n+1}, \end{aligned} \tag{5.21}$$

with

$$\begin{aligned} \theta &= \tau_0, \qquad I = -\frac{W - W_r}{W_r} \cdot \left(\frac{f_{mod}}{f_I}\right), \\ K &= \left(\frac{f_{mod}}{f_I}\right)^2 \cdot \frac{J_{\pm 1}\left(\frac{l\Delta Q_x f_{rev}}{f_{mod}}\right)}{J_0\left(\frac{l\Delta Q_x f_{rev}}{f_{mod}}\right)} \cdot \frac{\mathcal{A}_2\left(\pm\frac{f_{mod}}{f_I}\right)}{W_r}. \end{aligned} \tag{5.22}$$

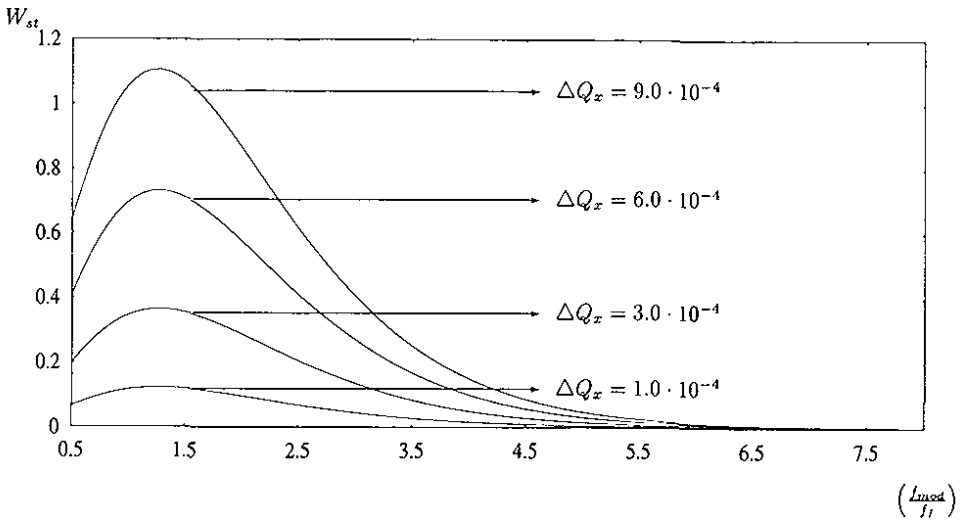

Figure 5.4:
The relative stochastic layer width W_{st} for the single resonance Hamiltonian and four different modulation depths.

An important feature of the standard map is that the motion becomes irregular for $K \gtrsim 1$ (see Section (4.2)). Thus, the relative width of the stochastic layer W can be estimated as the maximum value of W_r that satisfies the condition $K \gtrsim 1$. From (5.22) one gets for the stochastic layer width

$$W_{st} = 4\pi \cdot \left(\frac{f_{mod}}{f_I}\right)^3 \cdot \frac{J_{\pm 1}\left(\frac{l\Delta Q_x f_{rev}}{f_{mod}}\right)}{J_0\left(\frac{l\Delta Q_x f_{rev}}{f_{mod}}\right)} \cdot \frac{\exp\left[\frac{\pi f_{mod}}{2 f_I}\right]}{\sinh\left(\frac{\pi f_{mod}}{f_I}\right)}. \tag{5.23}$$

For $\Delta Q_x = 0$ the layer width becomes zero ($W_{st} = 0$) and for $W_{st} = \pm 1$ the stochastic layer covers the whole resonance area. Fig.5.4 shows the relative stochastic layer width W_{st} for the single resonance Hamiltonian (5.1) as a function of the modulation frequency for four different modulation depths. For ($f_{mod}/f_I < 0.5$), the argument of the Bessel functions in (5.23) becomes larger than two and Equation (5.23) can not be applied. It is interesting to note that the estimates for W agree well with tracking data. For example, for $\Delta Q_x = 3.0 \cdot 10^{-4}$ equation (5.23) predicts a stochastic layer which covers approximately half of the resonance area. This estimate agrees with the surface of section in the right-hand side of Fig.5.3. Furthermore, the analytical estimate for W_{st} predicts that the stochastic layer will cover the whole resonance area for $\Delta Q_x \geq 8.0 \cdot 10^{-4}$. The left-hand side of Fig.5.5 shows the surface of section of the single resonance Hamiltonian for $f_{mod} = f_{rev}/560$ and $\Delta Q_x = 6.0 \cdot 10^{-4}$, which is just below the critical value predicted by (5.23). One clearly recognizes the regions of regular motion around the stable fixed points of the primary resonance and the first-order modulation resonance. The right-hand side of Fig.5.5 shows the surface of section for $f_{mod} = f_{rev}/560$ and $\Delta Q_x = 8.0 \cdot 10^{-4}$. As was predicted by Equation (5.23), the stable fixed point of the primary

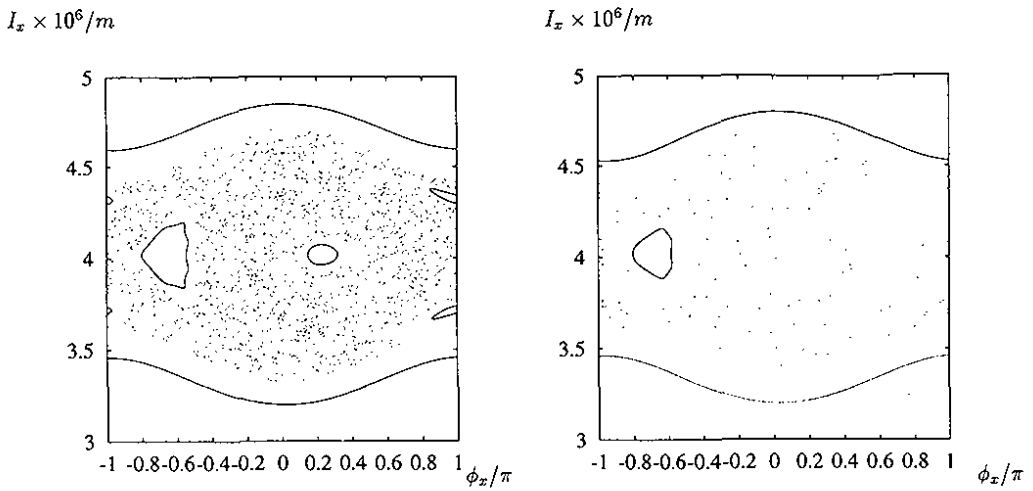

Figure 5.5:
The surfaces of section for the single resonance Hamiltonian.
Left: The surface of section for a tune modulation slightly above the 'free island' oscillation frequency with ($f_{mod} = f_{rev}/560, \triangle Q_x = 6.0 \cdot 10^{-4}$).
Right: The surface of section for a slow tune modulation slightly above the 'free island' oscillation frequency with ($f_{mod} = f_{rev}/560, \triangle Q_x = 8.0 \cdot 10^{-4}$).

resonance disappeared and only a small region of regular motion continues to exist around the stable fixed point of the first-order modulation resonance. Increasing the modulation depth even further, the last region of regular motion finally disappears for $\triangle Q_x = 3.0 \cdot 10^{-3}$. The left-hand side of Fig.5.6 shows the corresponding surface of section for $f_{mod} = f_{rev}/560$ and $\triangle Q_x = 4.0 \cdot 10^{-3}$.

Another interesting aspect of Equation (5.23) is that it has a distinct maximum for $f_{mod} \approx f_I$. For any other modulation frequency and the same modulation depth the stochastic layer width is smaller than for $f_{mod} \approx f_I$. The right-hand side of Fig.5.6 shows the surface of section for a tune modulation with $f_{mod} = f_{rev}/1120$ and $\triangle Q_x = 8.0 \cdot 10^{-4}$. Even though the modulation depth is the same as for the $f_{mod} = f_{rev}/560$ modulation in the right-hand side of Fig.5.5, the stochastic layer width is now much smaller.

5.3 Phase Diagrams

The qualitatively different modulation effects are related to distinct areas in the parameter space of the tune modulation. A convenient way to illustrate the different areas in the parameter space is a 'phase diagram', as it was first proposed in [78] and further modified in [53]. For a given primary resonance the Equations (5.7), (5.8), and (5.23) describe approximate boundaries between areas of different modulation effects in the $(f_{mod}, \triangle Q_x)$ space. Here, we present a slightly modified 'phase diagram', which incorporates the trapping condition. Ex-

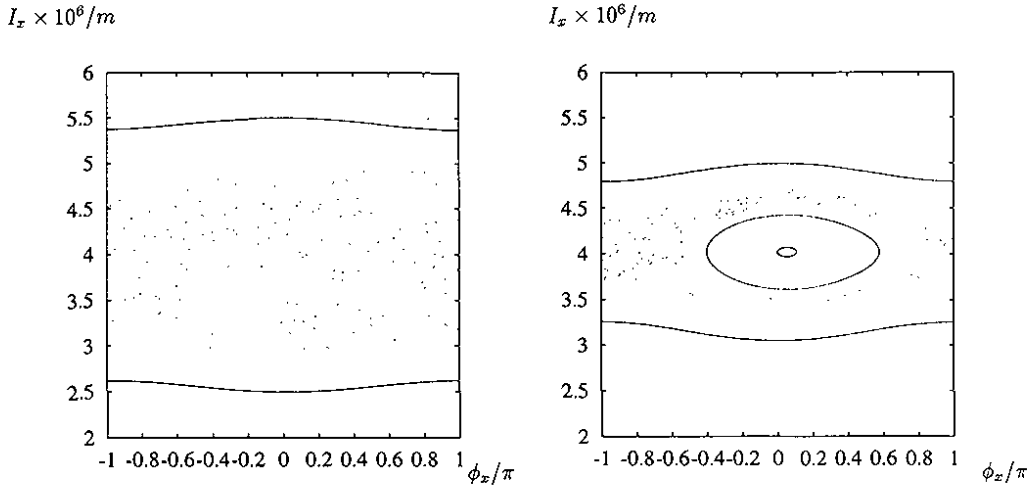

Figure 5.6:
The surfaces of section for the single resonance Hamiltonian.
Left: The surface of section for a tune modulation slightly above the 'free island' oscillation frequency with ($f_{mod} = f_{rev}/560, \triangle Q_x = 4.0 \cdot 10^{-3}$).
Right: The surface of section for a slow tune modulation with ($f_{mod} = f_{rev}/1120, \triangle Q_x = 8.0 \cdot 10^{-4}$).

pressing the overlap and trapping conditions in terms of the 'free island' oscillation frequency, one gets for the overlap condition (5.7)

$$\triangle Q_x < \frac{16\pi}{l} \cdot \left(\frac{f_I}{f_{rev}}\right)^4 \cdot \left(\frac{f_{rev}}{f_{mod}}\right)^3 \tag{5.24}$$

and for the trapping condition (5.8)

$$\triangle Q_x < \frac{1}{l} \cdot \left(\frac{f_I}{f_{rev}}\right)^2 \cdot \left(\frac{f_{rev}}{f_{mod}}\right). \tag{5.25}$$

Together with the condition $W_{st} = 1$, these inequalities describe boundaries in the parameter space that separate areas with distinct modulation effects. Fig.5.7 shows the resulting boundaries in the parameter space of the tune modulation for the single resonance Hamiltonian and the parameter values (5.3). The circles correspond to the modulation parameters for the surface of sections in Fig.5.1 - 5.3 and Fig.5.5 - 5.6, and Table (5.26) lists the corresponding modulation parameters and figures.

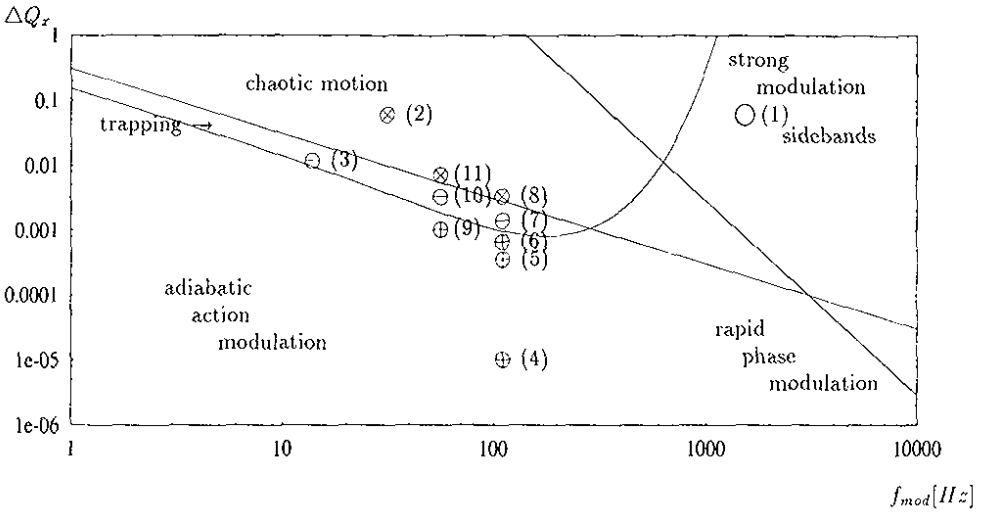

Figure 5.7:
The phase diagram for the single resonance Hamiltonian and the parameter values (5.3). The circles correspond to the modulation parameters for the surface of sections in Fig.5.1 - 5.3 and Fig.5.5 - 5.6. Table (5.26) lists the corresponding modulation parameters and figures.
$\bigcirc$*: strong modulation sidebands.*
$\oplus$*: resonance area with stable fixed point of the primary resonance and trapping.*
$\ominus$*: resonance area without stable fixed point of the primary resonance but with trapping.*
$\otimes$*: chaotic motion.*

Modulation Parameters for the Single Resonance Hamiltonian			
#	Figure	ΔQ_x	f_{mod}
(1)	right-hand side Fig.5.1	0.05	$1532.5Hz$
(2)	left-hand side Fig.5.2	0.05	$30.65Hz$
(3)	right-hand side Fig.5.2	0.01	$15.33Hz$
(4)	left-hand side Fig.5.3	$1.0 \cdot 10^{-5}$	$109.46Hz$
(5)	right-hand side Fig.5.3	$3.0 \cdot 10^{-4}$	$109.46Hz$
(6)	left-hand side Fig.5.5	$6.0 \cdot 10^{-4}$	$109.46Hz$
(7)	right-hand side Fig.5.5	$8.0 \cdot 10^{-4}$	$109.46Hz$
(8)	left-hand side Fig.5.6	$4.0 \cdot 10^{-3}$	$109.46Hz$
(9)	right-hand side Fig.5.6	$8.0 \cdot 10^{-4}$	$54.73Hz$
(10)	/	$4.0 \cdot 10^{-4}$	$54.73Hz$
(11)	/	0.01	$54.73Hz$

(5.26)

The 'phase diagram' has five distinct areas:

- Strong Modulation Sidebands:
  For a fast tune modulation with large modulation amplitudes the sidebands do not overlap and the motion remains regular.

- Rapid Phase Modulation:
  For a fast tune modulation with small modulation amplitudes the modulation sidebands are weak and can be ignored.

- Adiabatic Action Modulation:
  A slow tune modulation with small modulation amplitudes leads only to a narrow stochastic layer around the unperturbed separatrix and most of the phase space area is associated with a regular particle motion.

- Trapping:
  If the modulation amplitude is increased, the stochastic layer becomes wider until the stable fixed point of the primary resonance vanishes. However, as long as the trapping condition is fulfilled, some fraction of the resonance area corresponds still to regular particle motion.

- Chaotic Motion:
  If the modulation amplitude is even further increased to the point that the trapping condition is no longer fulfilled, the whole resonance area corresponds to an irregular particle motion.

At the end of this Section, the transition from 'adiabatic action modulation' to 'chaotic motion' is illustrated with the surface of sections in Fig.5.5-5.6 for $f_{mod} = f_{rev}/560$. The left-hand side of Fig.5.5 shows the surface of section for $f_{mod} = f_{rev}/560$ and $\Delta Q_x = 6.0 \cdot 10^{-4}$, which is just below the $W_{st} = 1$ curve in the phase diagram (data point (6) in Fig.5.7), so that the motion near the stable fixed point of the primary resonance is still regular. If the modulation depth is slightly increased, the modulation parameters lie inside the 'trapping' region of the 'phase diagram'. The right-hand side of Fig.5.5 shows the surface of section for $f_{mod} = f_{rev}/560$ and $\Delta Q_x = 8.0 \cdot 10^{-4}$, which is just inside the 'trapping' region (data point (7) in Fig.5.7). One clearly recognizes the wide stochastic layer and the small 'trapped' region of regular motion. If the modulation depth is even further increased, the modulation parameters lie inside the region of 'chaotic motion' and the small region of stable motion disappears. The left-hand side of Fig.5.6 shows the surface of section for $f_{mod} = f_{rev}/560$ and $\Delta Q_x = 4.0 \cdot 10^{-3}$, which corresponds to the data point (8) in Fig.5.7. As expected, the irregular motion covers the whole resonance area of the primary resonance.

The discussion of the various effects of a tune modulation on the phase space structure underlines the importance of the tune modulation for an analysis of the emittance growth in a storage ring and motivates a closer look at the origins of the tune modulation in a real storage ring like the proton ring in HERA.

Section 6

Origins of Tune Modulation in HERA

The last Section discussed the effect of an external tune modulation on the phase space structure of a storage ring and showed how the tune modulation can lead to irregular particle motion. In a real storage ring, a tune modulation is caused by the power supply ripples and by ground motion. While the imperfections of the d-c power supplies lead to a set of well-defined modulation frequencies, all larger or equal than $50Hz$, the ground motion leads to a time-dependent set of slow modulation frequencies below $50Hz$. The following overview summarizes the main sources for the tune modulation in the proton storage ring of HERA. The overview is organized in five parts. The first part summarizes the causes for current ripples in the d-c power supplies of HERA-p, and a second part discusses the effect of the ripples on the main dipole and quadrupole chains in HERA-p. A third part looks at the effect of the ground motion in the HERA tunnel on the betatron tune values, and a fourth part estimates the tune modulation in the proton beam due to the beam-beam interaction and a closed orbit oscillation in the proton and electron beam. A fifth part summarizes the measurements of the tune modulation and closed orbit oscillations in the proton beam of HERA.

6.1 Inherent Power Supply Ripples

The superconducting main circuit of the HERA-p storage ring requires a d-c current of high accuracy. To derive such a d-c current, the power supply uses twelve-phase (before September 1991 only six-phase) a-c power lines with a frequency of $50Hz$ and four three-phase full-wave rectifier circuits with thyristor bridges. Each rectifier is followed by a passive filter that suppresses frequencies above $30Hz$. A transformer which splits the incoming three-phase signal of 1000 Volt into two three-phase signals of 400 Volt with a 30° phase difference precedes each set of two rectifiers.

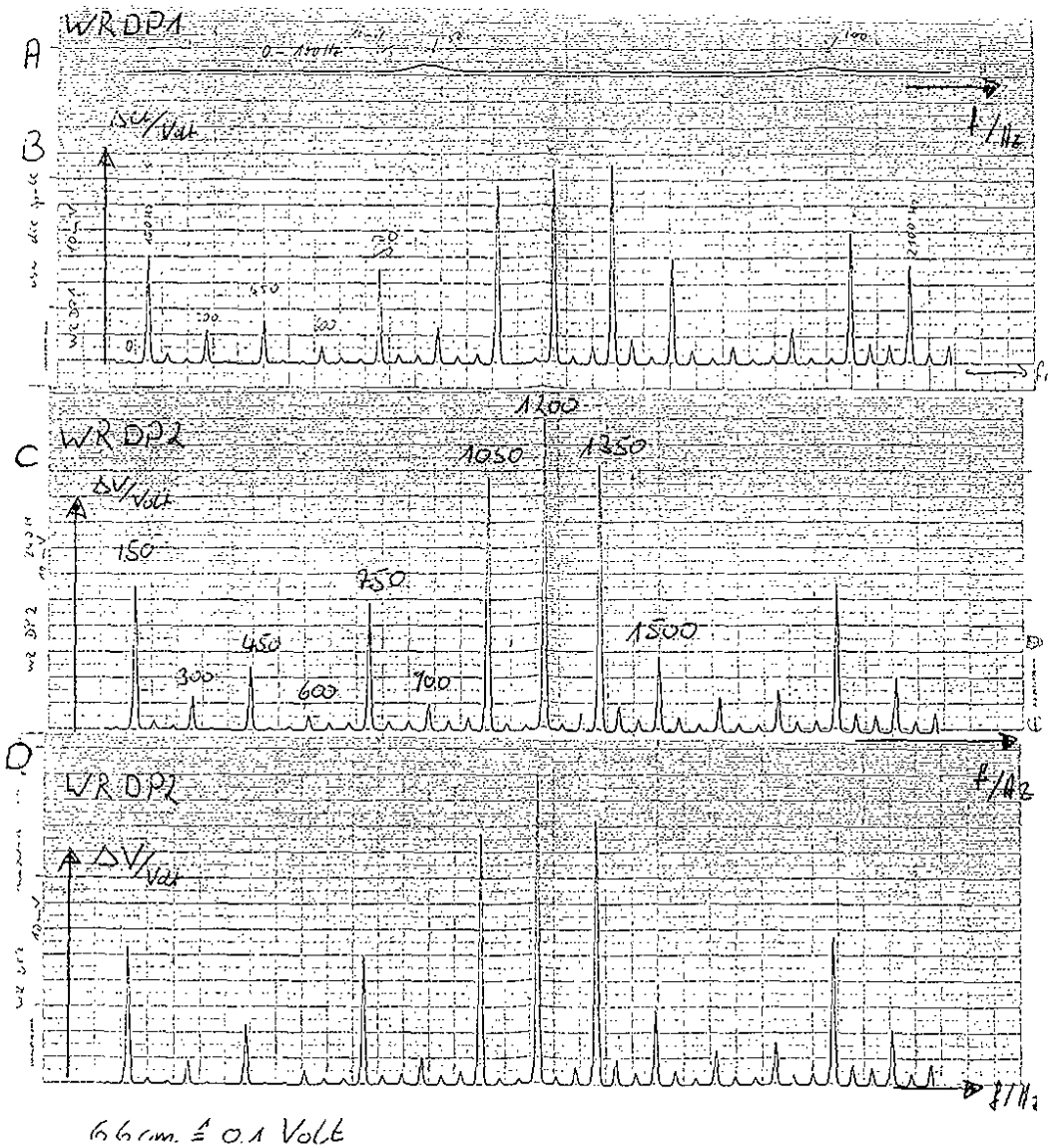

Figure 6.1:
Measurement of the voltage decrease over the WRDP1 and WRDP2 dipoles.
A: ΔV over WRDP1 for the frequency range 0Hz to 100Hz.
B: ΔV over WRDP1 for the frequency range 100Hz to 2200Hz.
C: ΔV over WRDP2 for the frequency range 100Hz to 2200Hz.
D: ΔV over WRDP2 during ramping for the frequency range 100Hz to 2200Hz.

Magnet type	Inductivity / mH	Capacity / nF
quadrupole	5	46
dipole	60	85

Table 6.1: Inductivity and capacity of the superconducting magnets.

Frequency / Hz	$\Delta U/mV$	$\Delta I/I$
50	4.5	$1.00 \cdot 10^{-06}$
150	60.6	$6.15 \cdot 10^{-06}$
300	19.7	$0.73 \cdot 10^{-06}$
450	25.8	$1.67 \cdot 10^{-06}$
600	10.6	$0.20 \cdot 10^{-06}$
750	54.5	$1.14 \cdot 10^{-06}$
900	21.2	$0.26 \cdot 10^{-06}$
1050	104.5	$1.59 \cdot 10^{-06}$
1200	112.1	$1.65 \cdot 10^{-06}$
1350	116.7	$1.29 \cdot 10^{-06}$
1500	62.1	$0.32 \cdot 10^{-06}$

Table 6.2: Frequency dependence of $\Delta I(f)/I$ measured at WRDP2.

The signals of the two transformers have again a 15° phase difference, so that the ideal power supply delivers a $1200Hz$ current output [80]. However, in a real power supply, the phase differences between the four three-phase full-wave rectifier circuits can not be adjusted with 100% accuracy. Therefore, in addition to the $1200Hz$ mode, the current output of the real power supply also has $300Hz$, $600Hz$, and $900Hz$ modes coming from an imperfect phase adjustment between the four rectifier circuits. In addition to these modes due to an imperfect phase adjustment, the outgoing signal will still have two additional modes. The first mode comes from the fact that the whole power supply circuit, due to its inductive and capacitive components, oscillates relative to the electric ground. The pulsed currents in the rectifier circuits excite these oscillations and lead to an additional $150Hz$ mode. A second additional mode will come from the $50Hz$ of the input signal. Furthermore, one expects harmonics of all the modes described above [79][80]. Fig.6.1 shows measurements of the voltage decrease over the dipole magnets WRDP1 and WRDP2 [81]. All measurements were done with the new twelve-phase power supply.

Due to the superconducting material of the magnets one expects no decrease of the voltage for a purely d-c current. A decrease in the voltage can only be the result of the oscillating component of the current and is therefore a clear measure for fluctuations in the power supply. The top three measurements were done at injection energy ($40GeV$, $I = 240A$), and the measurement at the bottom of Fig.6.1 was done during the process of ramping. One clearly sees the $150Hz$, $300Hz$, $600Hz$, $900Hz$, and $1200Hz$ modes and their harmonics. Knowing the dipole impedance, one can calculate the amplitude of the corresponding current ripple. The measured dipole and quadrupole inductivity and capacity are listed in Table (6.1)[81],

and the resulting relative current ripples $\Delta I(f)/I$ are listed in Table (6.2) for $I = 240A$. For all frequencies up to $1300Hz$ the maximum relative ripple $\Delta I(f)/I$ is of the order 10^{-6}. For frequencies above $5000Hz$, the current ripples are strongly suppressed by the skin effect in the copper layer inside the vacuum chamber. The frequency-dependent skin depth is given by

$$\delta(f) = \frac{1}{\pi f \mu_0 \sigma}, \tag{6.1}$$

where σ is the conductivity and μ_0 the magnetic permeability. The copper layer has a thickness $d = 10\mu m \pm 5\mu m$ at a radius $r = 27.5mm$ from the center of the vacuum chamber. The frequency-dependent 'shielding factor' $S(f)$ is defined as the ratio of the magnetic field inside the vacuum chamber to the field at a great distance from it. For the superconducting dipole magnets, the 'shielding factor' has the form [82][83]

$$S(f) = \left[\cosh(d \cdot k(f)) + 0.5 \cdot \left[K(f) + \frac{1}{K(f)}\right] \cdot \sinh(d \cdot k(f))\right]^{-1}, \tag{6.2}$$

where

$$\begin{aligned} k(f) &= \frac{1+i}{\delta(f)} \\ K(f) &= k(f) \cdot (r-d). \end{aligned}$$

Fig.6.2 shows the absolute value of the 'shielding factor' $S(f)$ as a function of the modulation frequency for a cold beam pipe ($\sigma = 4 \cdot 10^9$ at $4K$). The layer thickness can vary between $5\mu m$ and $15\mu m$ for each magnet and Fig.6.2 shows the resulting variation in the 'shielding factor'. Equation (6.2) indicates that all modulation frequencies above $5KHz$ are suppressed by more than one order of magnitude and can hence be neglected for an analysis of the tune modulation.

In order to estimate the resulting tune modulation of the main power supplies, one has to take into consideration how the superconducting magnets are connected to the power supplies. The superconducting magnets of the main circuit in the HERA-p storage ring are connected in series. In order to avoid an overall dipole moment in the circuit, the current flows first clockwise from the power supply in Halle West through all the main dipole magnets and then counter-clockwise through all quadrupole magnets back to the power supply. The dipole chain is therefore connected to the plus pole of the power supply and the quadrupole chain to the minus pole, so that the first magnets of both chains see current ripples of the same magnitude. As a consequence, a current ripple in the main circuit changes the focusing strength of the quadrupoles as well as the deflecting dipole field. In contrast to the ripples in the main quadrupole chain, the current ripples in the dipole chain decrease very rapidly with increasing distance if their frequency is not in resonance with the dipole chain impedance. Fig.6.3 shows the decrease of the ripple amplitude versus the distance traveled in the dipole chain for different frequencies[81]. The ripple amplitude in the quadrupole chain remains approximately constant for all magnets.

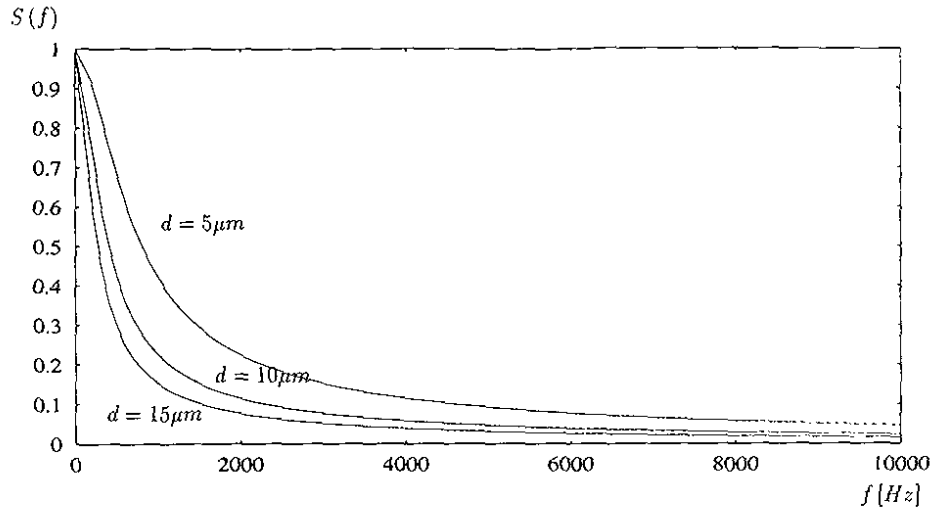

Figure 6.2:
The 'shielding factor' $S(f)$ as a function of the modulation frequency in the main dipole magnets and a cold beam pipe ($\sigma = 4 \cdot 10^9$ at $4K$).

6.2 Current Ripples in the Main Circuit

The current ripple in the quadrupole chain alters the betatron tune and the current ripple in the main dipole magnet changes the guiding dipole field. Since the ripple frequencies are much larger than the synchrotron frequency ($f_{syn} \sim 20Hz$), the particle momentum remains approximately constant so that the particle momentum and the main dipole field do not match. In the sextupoles, the resulting off-momentum trajectory leads to a change in the betatron tune, which partially compensates the tune change in the quadrupoles.

However, the fluctuations in the HERA-p power supplies result in a non-vanishing tune modulation for two reasons. First, the spatial decrease of the ripple amplitude in the dipole magnets leads to varying ripple amplitudes in the dipole and quadrupole magnets. As a consequence of this different behaviour of the main dipole and quadrupole chains, the compensation of the tune modulation is not perfect and results in a residual tune modulation[80].

Second, independent power supplies feed the normal-conducting quadrupoles in the straight sections. Since the sextupoles also compensate the chromaticity of the quadrupoles in the straight section, the tune modulation caused by the ripple in the cold quadrupoles is 'over-compensated'.

For the above reasons, only a partial compensation of the tune modulation is possible and the measured current fluctuations in Table (6.2) will lead to a net tune modulation of the order of [84][80][53]

$$\Delta Q = 10 \cdot \frac{\Delta I}{I}. \tag{6.3}$$

Depending on the ripple frequency, the tune modulation amplitude can be further amplified by the transmission line characteristics of the main circuit [85][86]. Hence, taking the largest $\Delta I/I$ value in Table (6.2) ($150Hz$) as a typical value for the ripple amplitude, it is realistic

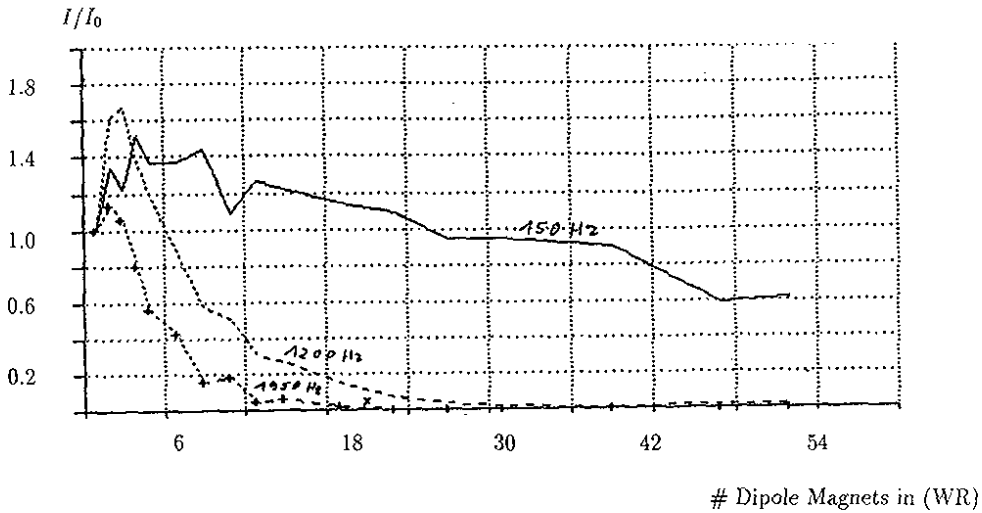

Figure 6.3:
Decrease of the ripple amplitude versus the distance traveled in the dipole chain in number of magnets [81]. The top curve shows the current decrease for a signal with $f = 150Hz$, the middle curve for $f = 1200Hz$, and the bottom curve for $f = 1950Hz$. One octant has 52 dipole magnets.

to expect a tune modulation as large as

$$\Delta Q_{MainCircuit} = 10^{-4}. \tag{6.4}$$

In addition to the current fluctuations in the main circuit, current ripples in the power supplies for the normal-conducting quadrupoles near the interaction regions (QS10 and QR10) are an additional source for a tune modulation in the HERA-p storage ring and can lead to a tune modulation of the same order of magnitude as the one caused by the main circuit [53]. While the current ripple in the main circuit is the dominant source for a tune modulation at injection energy, its contribution to the tune modulation at $820GeV$ is negligible because of the large d-c current ($I \approx 5000A \rightarrow \Delta I/I = O(10^{-7})$). At $820GeV$ the current ripple in the quadrupoles near the interaction regions and the closed orbit oscillations at the intersection points are the dominant source for a tune modulation.

6.3 Ground Motion Effects

The second source for a tune modulation in the storage ring is the ground motion [87][88][89]. Due to the ground motion, the magnets change their positions with time and the circulating beam experiences slightly misaligned magnets. The frequency spectrum of the ground motion covers almost all frequencies between $1.0Hz$ and $10.0Hz$ with the largest signals being between $3.0Hz$ and $6.0Hz$ [88]. In addition to this range, the spectrum has strong lines at $16Hz$, $22Hz$, and $32Hz$ coming from the vibrations of the vacuum pumps [88]. The rms amplitude of the ground motion is of the order of $\Delta x_{rms} \approx O(0.1\mu m)$ and fluctuates over the week depending

on the day and the hour. On the magnets, the effect of the ground motion is amplified by approximately one order of magnitude due to the suspension of the magnets [89]. Assuming an uncorrelated motion of the magnets, one can calculate the effect of the magnet misalignment on the beam and obtains for the root-mean-square (rms) tune modulation amplitude [88]

$$\triangle_{rms}Q_{GroundMotion} \approx 10^{-4}[\mu m^{-1}] \times \triangle y_{rms}. \tag{6.5}$$

Taking $0.1\mu m$ as a typical rms amplitude of the ground motion, one expects a tune modulation of the order of

$$\triangle_{rms}Q_{GroundMotion} \sim 10^{-5}. \tag{6.6}$$

6.4 Closed Orbit Oscillations and the Beam-Beam Interaction

The combined effect of closed orbit oscillations and the beam-beam interaction can lead to an additional tune modulation. The closed orbit oscillation can be caused either by the current ripple in the main dipole magnets or by uncorrelated vibrations of the quadrupole magnets and a resulting dipole field error.

The linear particle motion in a changing dipole field is governed by the differential equation

$$x''(s) + \left(\rho^{-2}(s) + k(s)\right) \cdot x(s) = \frac{\triangle B(s)}{B} \cdot \frac{1}{\rho(s)}, \tag{6.7}$$

where the prime denotes differentiation with respect to the arc length s, $\rho(s)$ is the radius of curvature, and $k(s)$ is the quadrupole strength. The homogeneous part of the equation has the solution

$$x(s) = A \cdot \sqrt{\beta(s)} \cdot \cos\left(\phi(s) + \theta\right) \tag{6.8}$$

and the constants A and θ are adjusted such that the closed orbit solution $Y(s)$ satisfies the boundary condition

$$Y(s + L) = Y(s). \tag{6.9}$$

The closed orbit solution to Equation (6.7) is given by [90]

$$Y(s) = \frac{\sqrt{\beta(s)}}{2\sin\pi Q} \cdot \int_s^{s+L} dt \frac{\sqrt{\beta(t)}}{\rho(t)} \cdot \frac{\triangle B(t)}{B} \cdot \cos\left(\phi(t) - \phi(s) - \pi Q\right). \tag{6.10}$$

Assuming a dipole modulation which is much slower than the revolution frequency ($f_{rev} \approx 47.3KHz$) and which extends spatially only over one dipole magnet ($l_{Dip} \sim 10m$), one gets for the rms closed orbit oscillation amplitude

$$Y_{rms,ripple}(s) = \frac{\sqrt{\beta(s)} \cdot \sqrt{<\beta>}}{2\sin\pi Q} \cdot \frac{\cos\pi Q}{\rho} 2\sin\pi Q \cdot \frac{\triangle_{rms} I}{I} \cdot l_{Dip}. \tag{6.11}$$

where Q is the betatron Q-value.

Assuming an uncorrelated motion of M quadrupole magnets due to the ground motion in the HERA tunnel, one gets for the rms closed orbit oscillation amplitude [88]

$$Y_{rms,groundmotion} \approx \frac{\sqrt{\beta(s)} \cdot \sqrt{<\beta>}}{2\sin\pi Q} \cdot k \cdot l_{Quad} \cdot \triangle_{rms} y \cdot \sqrt{M}. \tag{6.12}$$

where l_{Quad} is the length of the quadrupole magnets, k the focusing strength, M the number of magnets, and $\triangle_{rms}y$ the rms amplitude of the quadrupole oscillations.

In both cases one gets for the rms amplitude of the closed orbit oscillation at the interaction regions [88][89]

$$Y_{rms} = O\left(10\mu m\right), \tag{6.13}$$

which is about 30% of the vertical electron beam size and about 3% of the horizontal electron beam size. The closed orbit oscillation leads to an off-center collision of the electron and the proton beam at the interaction regions and thus to a change in the beam-beam detuning term. In the case of round beams, one can analytically calculate the detuning term from the beam-beam potential (3.6). Differentiating (3.6) with respect to the action variable I and averaging over the angle variable ϕ, one gets for the beam-beam detuning term

$$\triangle Q = 2 \cdot \xi \frac{4\pi\sigma^2}{\beta^* I} \cdot \left[1 - \exp\left(-\frac{\beta^* I}{2\sigma^2}\right) \cdot \exp\left(-\frac{d^2}{2\sigma^2}\right) I_o\left(\frac{\beta^* I}{2\sigma^2}\right) \cdot I_o\left(\frac{2d\sqrt{2\beta^* I}}{2\sigma^2}\right)\right], \tag{6.14}$$

where $I_0(z)$ is the modified Bessel function and d is the beam offset. In the case of a flat electron beam one can calculate the beam-beam detuning term by integrating the integral in the derivative of the beam-beam potential with respect to the action variable numerically and using an FFT. Varying the horizontal and vertical beam offsets over the range of the closed orbit oscillation amplitude (6.13), one gets in both cases

$$\triangle Q \sim 5 \cdot 10^{-5}. \tag{6.15}$$

Hence, the closed orbit oscillation due to the ground motion in combination with the beam-beam interaction can lead to a significant tune modulation.

The combination of the beam-beam interaction with the electron closed orbit oscillation also implies an additional tune modulation in the proton beam, in the same way as the combination of the beam-beam interaction with a proton closed orbit oscillation leads to an additional tune modulation. Thus, via the beam-beam interaction, the power supply ripple in the electron machine and the resulting electron closed orbit oscillation couples to the proton beam and can lead to a tune modulation in the proton beam.

6.5 Measurement of the Modulation Frequencies in the Proton Beam

During the 1993 luminosity run, H. Meß and M. Seidel analyzed the loss rates at the proton loss monitors. During their measurement a horizontal collimator was moved to a position of approximately 8σ into the beam halo and the resulting proton losses were recorded at the loss monitors near the collimator. Subsequently, the loss rates were analyzed by an FFT. Superimposing several FFT measurements, one clearly recognizes individual frequency components in the loss rates. Fig.6.4 shows the resulting frequency components of the loss rates [91]. The measurement was done during a luminosity run in October 1993 and confirms the existence of the inherent power supply frequencies between $100Hz$ and $2000Hz$ and the ground motion frequencies between $1Hz$ and $24Hz$. However, it is not clear whether the measured frequency spectrum comes from a modulation of the diffusion rates due to a residual tune modulation in the storage ring, or from a closed orbit oscillation at the collimators.

Assuming a tune modulation as the cause of the frequency components, one can compare the measured amplitudes with the amplitude of an external tune modulation with a given amplitude. During the machine shifts in the fall of 1993, a pair of superconducting quadrupole magnets was used ($WRQP62$) for an external tune modulation with $46.4Hz$. The $46.4Hz$ frequency was chosen because it does not appear in the natural spectrum in Fig.6.4. A comparison of the $46.4Hz$ signal with the frequency components between $1Hz$ and $50Hz$ indicated a tune modulation of [92]

$$\triangle Q \approx 5.0 \cdot 10^{-5}, \tag{6.16}$$

which agrees nicely with the predicted values in Equations (6.5) and (6.15). Unfortunately, the fast frequency components could not be measured because of the low electron beam current and the resulting low loss rates during the measurement.

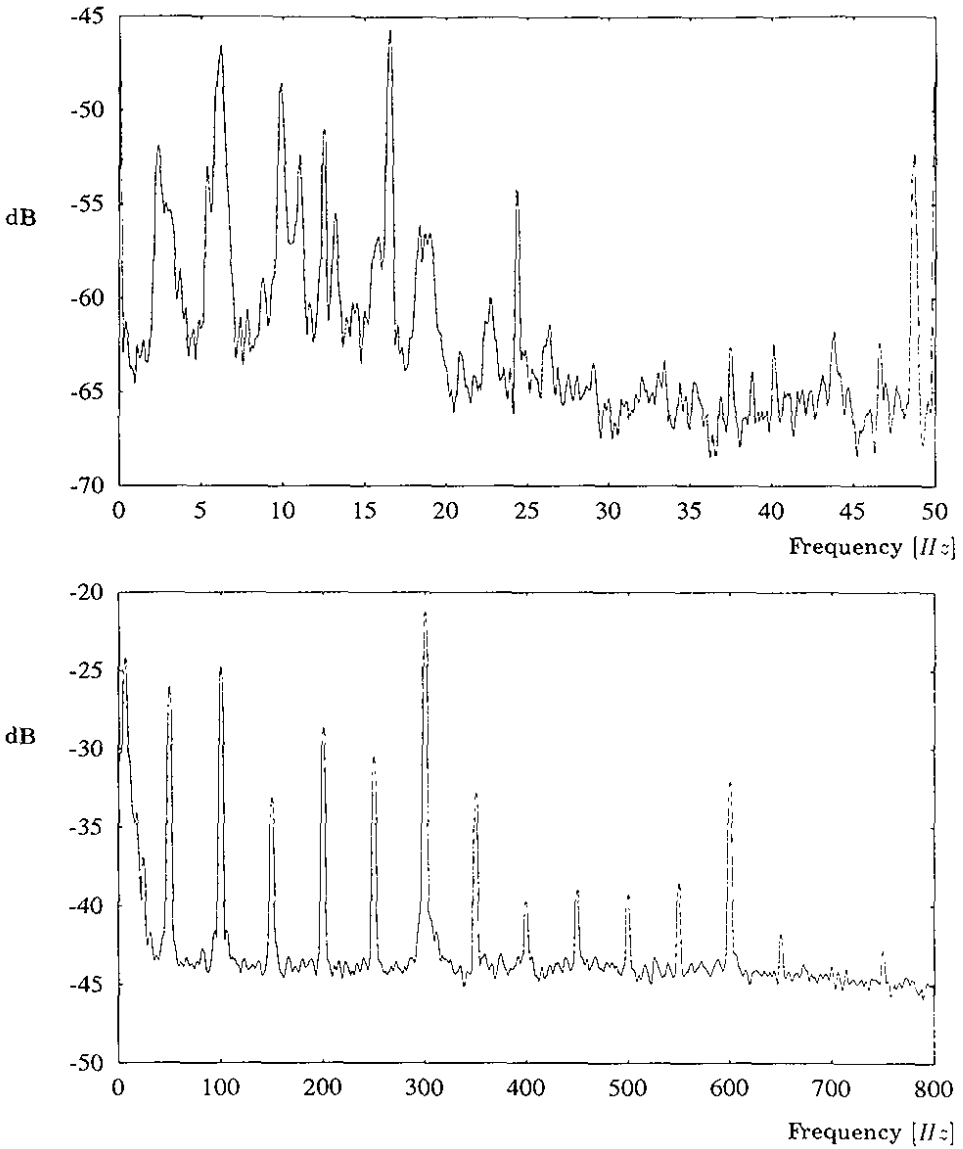

Figure 6.4:
Measurement of the frequency components in the loss rate at the pin-diodes during a luminosity run in October 1993 [91]. The frequency spectrum shows all the frequencies of the main circuit and the ground motion.
Top: the low frequency components in the loss rate.
Bottom: the high frequency components in the loss rate.

Section 7

Dynamic Aperture

This section aims to illustrate how one can use the overlap criterion in Section (4.3) in combination with perturbation theory for an estimate of the dynamic aperture in a storage ring. The Section consists of two parts. In a first part a simple model for the particle motion inside a storage ring is analyzed. Looking at a linear transfer map with sextupole kicks the dynamic aperture is estimated with the help of perturbation theory. A perturbative procedure for an estimate of the dynamic aperture is particularly useful for low-emittance light sources, which require strong sextupole magnets for the chromaticity corrections [93]. Introducing an additional tune modulation as it is caused by the power supply ripples and the ground motion, the dynamic aperture becomes smaller.

The second part of this section illustrates the limiting effect of a tune modulation with more than one modulation frequency on the dynamic aperture and outlines the main differences to the case of a tune modulation with one frequency component only. The particularly harmful effect of a tune modulation with more than one frequency component was first observed in a recent experiment in the SPS at CERN [8]. The contents of this Section summarizes the work in [94] and presents a qualitative picture for the increase of the particle diffusion in the presence of more than one modulation frequency.

As the particles remain only a few minutes at injection energy, one is not interested in the evaluation of diffusion coefficients which describe a slow emittance growth, but rather in a criterion for a quick particle loss. Thus, this Section describes only the criteria for the onset of unstable particle motion and does not evaluate diffusion and drift coefficients. A detailed evaluation of diffusion and drift coefficients is given in the next sections, where the effect of the tune modulation on the particle motion in HERA at luminosity conditions is discussed.

7.1 Model Analysis

Starting point for the model analysis is the Hamilton function (3.12) in action-angle variables for a harmonic tune modulation and sextupole kicks with the parameter values

$Q_x = 25.158$	$Q_y = 25.252$	$L = 47.018 \cdot 10^2 m$	$\lambda = 3.0 m^{-2}$	$f_{rev} = 61.3 KHz.$

(7.1)

L is 100 times the HERA-p FODO cell length, λ is about 8% of the sextupole strength of the sextupole correction coils in these 100 HERA-p FODO cells [95], and f_{rev} the revolution frequency in the model structure.

In order to estimate the dynamic aperture analytically, one has to analyze the resonance structure of the Hamilton function with the help of perturbation theory. Neglecting all the vertical Fourier modes for the sake of simplicity ($I_z \equiv 0$) one gets

$$H = \nu_x \cdot I_x + \frac{1}{2}\varepsilon^2 \nu_{x,2} \cdot I_x^2 + \frac{1}{3}\varepsilon^4 \nu_{x,4} \cdot I_x^3 + \tag{7.2}$$

$$\sum_{\alpha,l,m,k,\vec{n}} \left[\prod_{p=1}^{N} J_{n_p}\left(\frac{l \Delta Q_p f_{rev}}{f_{mod,p}} \right) \right] \cdot \varepsilon^{\alpha} \cdot A_{l,m,k}(I_x) \cdot \cos\left(l\phi_x + m\phi_z + \frac{2\pi}{L}\left(k + \frac{\vec{n} \cdot \vec{f}_{mod}}{f_{rev}} \right) \cdot s \right),$$

where α indicates the order in the perturbation series and $\nu_{x,2}$ and $\nu_{x,4}$ are the second and fourth order horizontal detuning terms respectively. For the convergence of the perturbation series it is also required that the perturbing Fourier modes are small compared to the linear part in (7.2). Because the sextupole potential increases with increasing action values, this condition is not satisfied for large action values and one can not analyze the resonance structure for action values larger than $10 \cdot 10^{-6} m$. In the following, the horizontal resonances are characterized by the parameter vector $(l, k, \vec{n})$, where l gives the horizontal resonance order in x, k the revolution harmonics, and $\vec{n}$ the order of the modulation sidebands. For the calculation of the non-linear detuning terms and resonance amplitudes in the Hamilton function (7.2), a computer algorithm based on Deprit perturbation theory [94] was used (see Appendix C), yielding the following non-linear detuning terms

Non Linear Detuning Terms in 4^{th} Order Perturbation Theory	
$\varepsilon^2 \cdot \nu_{x,2} = -9.0 m^{-2}$	$\varepsilon^2 \cdot \nu_{z,2} = -10.0 m^{-2}$
$\varepsilon^2 \cdot \nu_{xz,2} = +11.6 m^{-2}$	$\varepsilon^4 \cdot \nu_{x,4} = -0.12 \cdot 10^7 m^{-3}.$

(7.3)

Compared to the second-order detuning terms in the proton storage ring of HERA at $40 GeV$ [53], the second-order detuning terms in Table (7.3) are approximately three times larger than the values in HERA.

Solving the fixed point equations

$$\frac{\partial H}{\partial I_x} = 0, \qquad -\frac{\partial H}{\partial \phi_x} = 0, \tag{7.4}$$

for I_x, one can calculate the resonance positions in the transverse phase space. In the case of a purely horizontal resonance and small Fourier Amplitudes $\varepsilon^{\alpha} \cdot A_{l,m,k}$ one gets

$$I_{x,res} = \sqrt{\left(\frac{\varepsilon^2 \nu_{x,2}}{2\varepsilon^4 \nu_{x,4}} \right)^2 - \left(\frac{\nu_x + \frac{2\pi}{l \cdot L} \cdot \left[k + \frac{\vec{n} \cdot \vec{f}_{mod}}{f_{rev}} \right]}{\varepsilon^4 \nu_{x,4}} \right)} - \frac{\varepsilon^2 \nu_{x,2}}{2\varepsilon^4 \nu_{x,4}}. \tag{7.5}$$

For the first order resonances $(l = 1, m = 0, k = -25)$ and $(l = 3, m = 0, k = -74)$ the Fourier modes are of the same order of magnitude as the nonlinear detuning terms and have to be included in the fixed point equation. Equation (7.5) shows again that a slow modulation frequency leads to a small, and that a fast modulation frequency leads to a large spacing of neighbouring sidebands.

From Equation (7.5), one gets for the first eleven resonance positions

Analytically Calculated Resonance Positions	
$(l=1, k=-25, \vec{n}=\vec{0})$	$I_{x,res-1} = 11.2 \cdot 10^{-6} m$
$(l=2, k=-49, \vec{n}=\vec{0})$	$I_{x,res-1} = 23.6 \cdot 10^{-6} m$
$(l=3, k=-74, \vec{n}=\vec{0})$	$I_{x,res-3} = 22.8 \cdot 10^{-6} m$
$(l=4, k=-99, \vec{n}=\vec{0})$	$I_{x,res-4} = 17.9 \cdot 10^{-6} m$
$(l=5, k=-124, \vec{n}=\vec{0})$	$I_{x,res-5} = 16.6 \cdot 10^{-6} m$
$(l=6, k=-149, \vec{n}=\vec{0})$	$I_{x,res-6} = 15.63 \cdot 10^{-6} m$
$(l=7, k=-176, \vec{n}=\vec{0})$	$I_{x,res-7} = 1.80 \cdot 10^{-6} m$
$(l=8, k=-201, \vec{n}=\vec{0})$	$I_{x,res-8} = 3.75 \cdot 10^{-6} m$
$(l=9, k=-226, \vec{n}=\vec{0})$	$I_{x,res-9} = 4.39 \cdot 10^{-6} m$
$(l=10, k=-251, \vec{n}=\vec{0})$	$I_{x,res-10} = 5.12 \cdot 10^{-6} m$
$(l=11, k=-276, \vec{n}=\vec{0})$	$I_{x,res-11} = 5.67 \cdot 10^{-6} m.$

(7.6)

For all resonances in Table (7.6), the revolution harmonics k was chosen such that Equation (7.5) yields the smallest non-negative resonance value for the action variable. The $(8,0,-201)$, $(9,0,-226)$, and the $(10,0,-251)$ resonances lie particularly close to each other and the resonance islands will overlap if the corresponding Fourier modes satisfy

$$\varepsilon^o \cdot A_{l,m,k}(I_x) > 10^{-12}. \tag{7.7}$$

For the $(8,0,-201)$, $(9,0,-226)$, and the $(10,0,-251)$ resonances, the perturbative treatment indicates mode amplitudes of the order of

$$\varepsilon^o \cdot A_{l,m,k}(I_x) \sim 10^{-11}$$

and it is reasonable to expect unstable particle motion for $I_x > I_{max}$ with

$$I_{max} \approx 4.0 \cdot 10^{-6} m. \tag{7.8}$$

Fig.7.1 shows the numerically constructed surface of section for the Hamilton function (7.2). The left-hand side of Fig.7.1 shows the resonances in the P_x and x variables and the right-hand side of Fig.7.1 shows the resonances in the horizontal action-angle space. One clearly recognizes the $(7,-176,\vec{0})$, $(8,-201,\vec{0})$, and $(9,-226,\vec{0})$ resonances. For all action values larger than the action values of the $(9,0,-226)$ resonance the particle motion becomes unstable.

In order to compare the tracking data with the analytical estimates in Tables (7.6) it is helpful to transform the tracking data to a set of coordinates that does not show the large fluctuations in the action values. Using the transformations of the Deprit perturbation series up to second-order in the perturbation parameter ε one can bring the tracking data into second-order normal form [13][20][59], which clearly reduces the fluctuations in the action variable. The left-hand side of Fig.7.2 shows the second-order normal from of the surface of section in the Cartesian P_x and x variables, and the right-hand side of Fig.7.2 shows the second-order normal form of the surface of section in the corresponding action-angle variables. The numerical data in the right-hand side of Fig.7.2 yields for the resonance positions

Numerically Calculated Resonance Positions	
$(l=7, k=-176, \vec{n}=\vec{0})$	$I_{x,res-7} \approx 2.0 \cdot 10^{-6} m$
$(l=8, k=-201, \vec{n}=\vec{0})$	$I_{x,res-8} \approx 3.8 \cdot 10^{-6} m$
$(l=9, k=-226, \vec{n}=\vec{0})$	$I_{x,res-9} \approx 4.5 \cdot 10^{-6} m.$

(7.9)

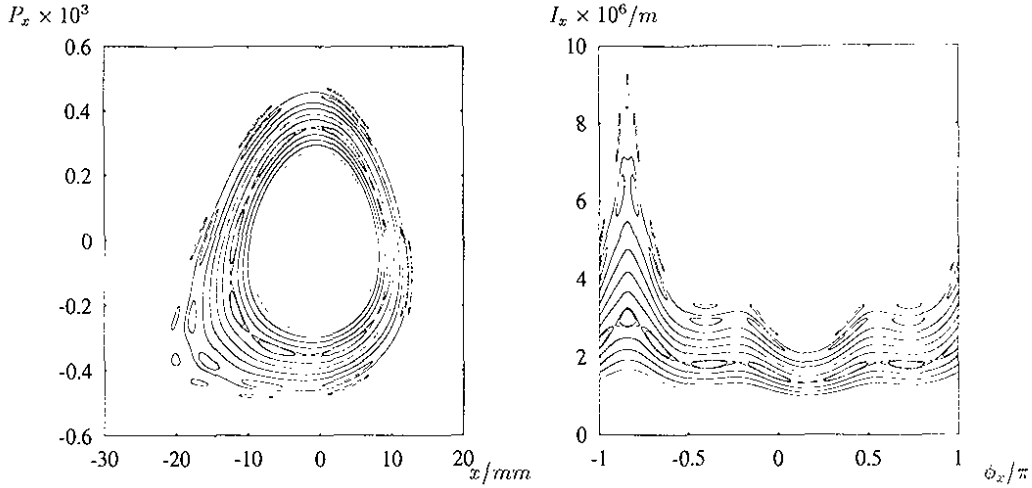

Figure 7.1:
The surfaces of section without tune modulation.
Left: The horizontal surface of section in the P_x and x variables.
Right: The horizontal surface of section in the action angle variables.

For all three resonances, the numerical data in Table (7.9) agree nicely with the analytical estimates in Table (7.6) and the particle motion becomes unstable for action values larger than $4 \cdot 10^{-6} m$. For all action values smaller than $4 \cdot 10^{-6} m$ the particle motion remains stable and the onset of unstable motion corresponds to the analytical estimate (7.8).

It is interesting to note that the fourth-order detuning term $\nu_{x,4}$ has a considerable contribution to Equation (7.5). Without the fourth-order detuning term, the analytical estimates of the action values for the $(8,-201,\vec{0})$ and $(9,-226,\vec{0})$ resonances are approximately twice as large as the values in the numerically constructed surface of section. Furthermore, it is interesting to note that the coordinate transformations do not converge up to second-order in the perturbation parameter ε if the action values are larger than the values of the $(9,-226,\vec{0})$ resonance. Thus, the onset of unstable particle motion coincides with a divergent second-order coordinate transformation.

In other words, outside the dynamic aperture, the system can not be transformed to second-order normal form. One could attempt to estimate the dynamic aperture by looking at the radius of convergence of the second-order normal form transformation. However, for storage rings with high-order multipole errors, a second-order normal form transformation can not be used for a calculation of the dynamic aperture. In this case, the convergence of the normal form transformation has to be analyzed to the order of the significant multipole errors. A detailed description of the methods to estimate the dynamic aperture in storage rings with high-order multipole errors is given in [53].

With the help of the surface of section in its second-order normal form, one can estimate the resonance half widths of the resonance islands and calculate the corresponding resonance

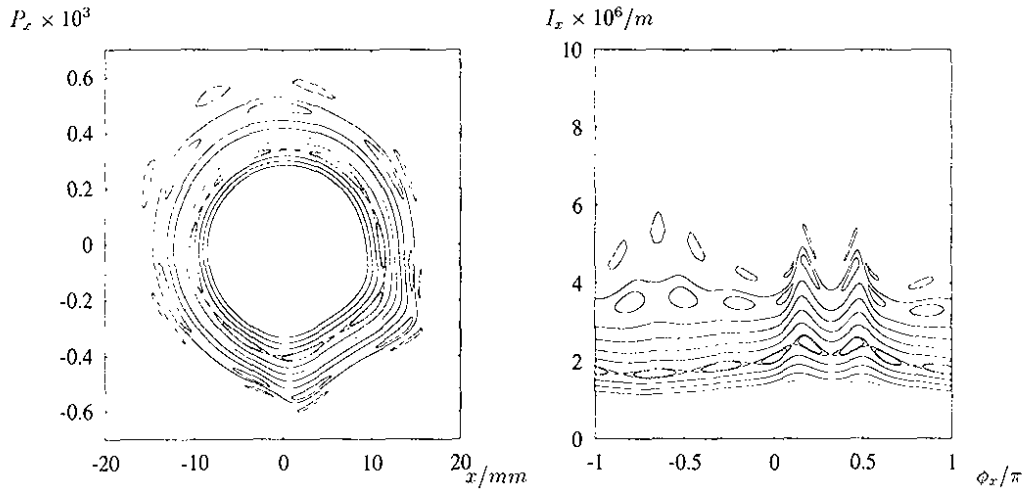

Figure 7.2:
The surfaces of section in second-order normal form.
Left: The horizontal surface of section in the P_x and x variables.
Right: The horizontal surface of section in the action angle variables.

amplitudes numerically. Approximating the Hamilton function (7.2) by the single resonance approximation and expanding the resulting Hamilton function into a Taylor series around a stable resonance fixed point one gets for the half width of the sextupole resonances

$$\triangle_{1/2} I = \sqrt{\left| \frac{4 \cdot A_{l,m,k}}{\varepsilon^2 \nu_{x,2} + 2\varepsilon^4 \nu_{x,4} \cdot I_{x,res}} \right|}. \tag{7.10}$$

Table (7.11) shows the resulting resonance amplitudes for the resonance islands in Fig.7.2.

Numerically calculated Resonance Amplitudes	
$(l=7, k=-176, \vec{n}=\vec{0})$	$\varepsilon^3 \cdot A_{7,0,-176} = 3.33 \cdot 10^{-14}$
$(l=8, k=-201, \vec{n}=\vec{0})$	$\varepsilon^4 \cdot A_{8,0,-201} = 7.59 \cdot 10^{-14}$
$(l=9, k=-226, \vec{n}=\vec{0})$	$\varepsilon^3 \cdot A_{9,0,-226} = 3.57 \cdot 10^{-14}$.

(7.11)

Defining the perturbation parameter ε such that

$$A_{l,m,k}(I_x, I_z) \sim \nu_x \cdot I_x, \tag{7.12}$$

all resonances in Table (7.11) fulfill the condition of moderate nonlinearity (4.11) and justify the use of the single resonance approximation in (7.10).

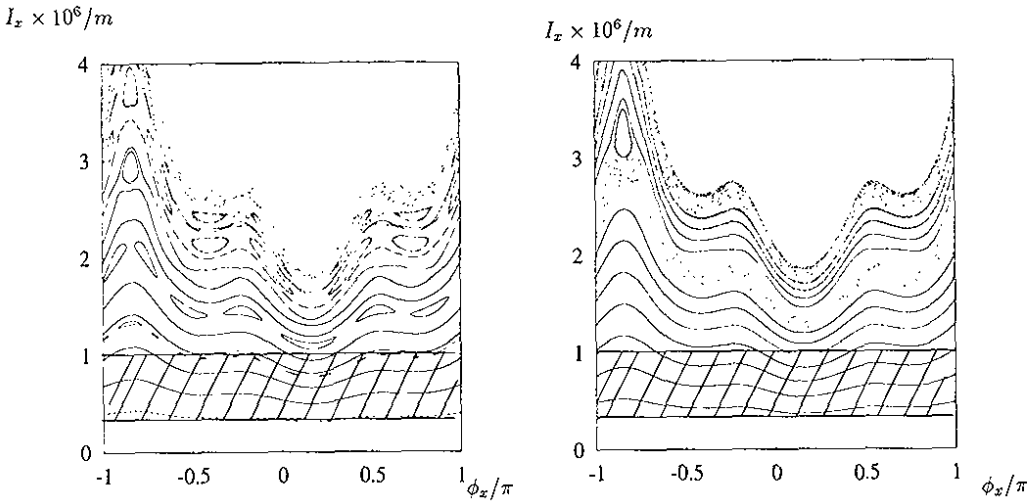

Figure 7.3:
The surfaces of section with tune modulation. The shaded area indicates the phase space volume occupied by a particle distribution.
Left: a fast tune modulation with $f = 1350Hz$ and $\Delta Q = 3.0 \cdot 10^{-3}$.
Right: a slow tune modulation with $f = 9Hz$ and $\Delta Q = 1.0 \cdot 10^{-3}$.

7.2 Tune Modulation with more than one Frequency Component

For action values smaller than $1.0 \cdot 10^{-6} m$, the particles experience no low-order resonances and are stable for more than 10^8 turns through the model structure. Thus, an efficient operation of the storage ring is possible as long as the stored particles lie inside the volume V_{beam}, given by

$$(I_x, I_z) \quad \text{with} \quad \begin{cases} 0.4 \cdot 10^{-6} m \leq I_x \leq 1.0 \cdot 10^{-6} m \\ 0.9 \cdot 10^{-7} m \leq I_z \leq 1.0 \cdot 10^{-7} m. \end{cases} \tag{7.13}$$

However, this situation changes if a tune modulation is turned on. A horizontal tune modulation leads to resonance sidebands of the resonances in Table (7.6) that can reach into the volume V_{beam} and reduce the dynamic aperture. The following discussion considers three different cases for the modulation frequencies:

a) a tune modulation with one fast and one slow modulation frequency;
b) a tune modulation with two fast modulation frequencies;
c) a tune modulation with frequencies near the free island oscillation frequency.

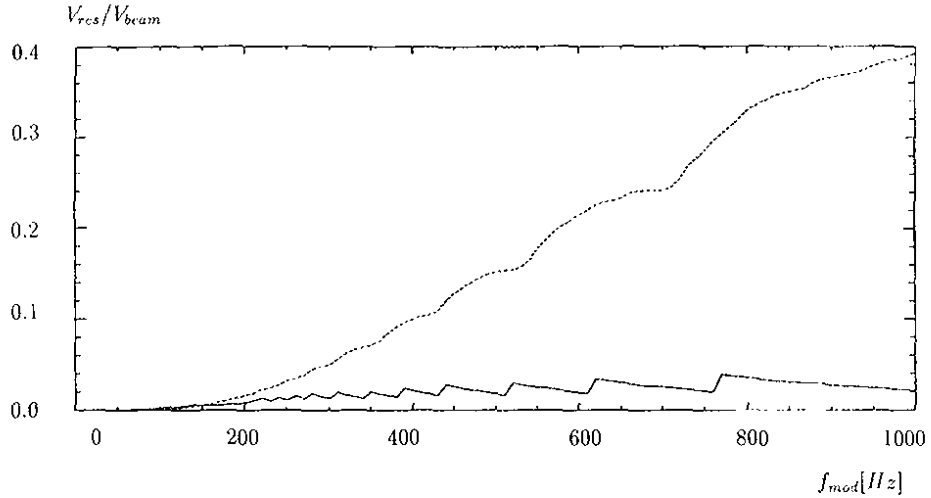

Figure 7.4:
The quotient V_{res}/V_{beam} vs. the modulation frequency. The solid line shows the relative volume for a tune modulation with one frequency only and the dashed line shows the relative volume for a modulation with two frequencies. For the latter, the slow modulation frequency was kept at $9Hz$ (the slowest modulation frequency used in the SPS experiment) and only the second frequency was varied.

a) Tune modulation with fast and slow modulation frequencies:

For a fast tune modulation ($f = O(100Hz)$) the distance of neighbouring sidebands is large (see Equation (7.5)), and the resonance amplitudes decrease very rapidly with increasing sideband order n_p

$$\hat{A}_{l,m,k}(I_x, I_z) = \sum_{n_p} \left[\prod_{p=1}^{N} J_{n_p} \left(\frac{l \Delta Q_p f_{rev}}{f_{mod,p}} \right) \right] \cdot A_{l,m,k}(I_x, I_z) . \qquad (7.14)$$

Hence, a fast tune modulation might only lead to a small number of well-separated sidebands which reach into the volume V_{beam}. The left-hand side of Fig.7.3 shows the surface of section for a fast tune modulation with $1350Hz$ and $\Delta Q = 3.0 \cdot 10^{-3}$. One clearly recognizes the $1350Hz$ modulation sidebands of the $(7, -176, \vec{0})$ resonance. The shaded area indicates the volume V_{beam} in the horizontal phase space. The modulation sidebands of the $(7, -176, \vec{0})$ resonance reach into the volume V_{beam}, but as the sidebands do not overlap, the phase space structure inside V_{beam} remains mainly regular. Only for action values outside the volume V_{beam} does the particle motion become irregular over a large regions of the phase space.

For a slow tune modulation ($f = O(1Hz)$) the behaviour is reversed. The distance of neighbouring sidebands is small, and the amplitudes decrease only slowly with increasing sideband order n_p. A slow tune modulation might therefore lead to a rich structure of overlapping sidebands, but no sidebands with a significant amplitude which can reach into the volume V_{beam}. The right-hand side of Fig.7.3 shows the surface of section for a slow tune modulation with $f = 9Hz$ and $\Delta Q = 1.0 \cdot 10^{-3}$. One recognizes the overlapping modulation

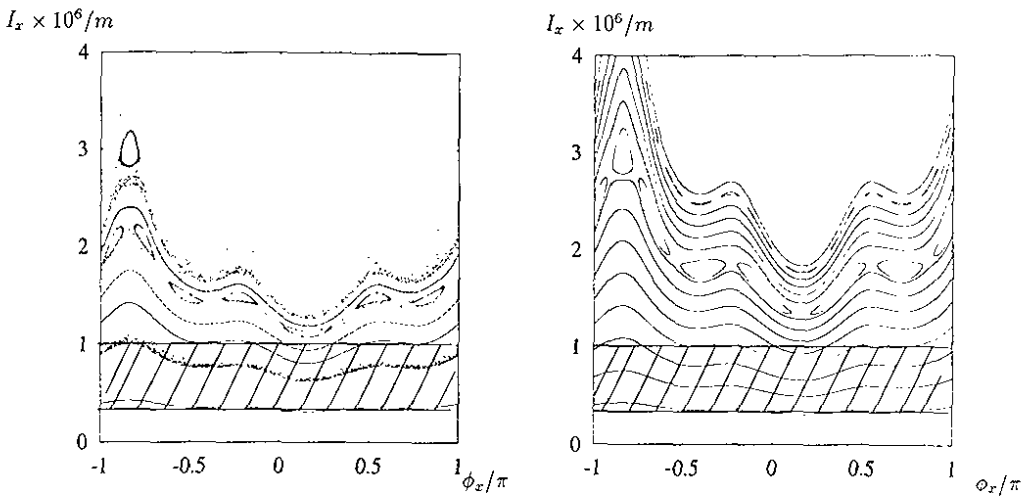

Figure 7.5:
The surface of section for two modulation frequencies. The shaded area indicates the phase space volume occupied by a particle distribution.
Left: a tune modulation with $1350Hz$ and $9Hz$ and $\Delta Q_{1350Hz} = 3.0 \cdot 10^{-3}$ and $\Delta Q_{9Hz} = 1.0 \cdot 10^{-3}$.
Right: the surface of section without any tune modulation.

sidebands around the initial sextupole resonances in Table (7.6), but no sideband reaches into the volume V_{beam}. Either of the modulation frequencies alone does not lead to a wide stochastic layer inside the volume V_{beam}. Consequently, a tune modulation with either frequency alone does not lead to a significant reduction in the dynamic aperture. For the case of a tune modulation with a fast and a slow frequency the situation changes drastically. The sidebands of the fast modulation frequency act as resonance seeds for the slow modulation frequency, i.e., the slow tune modulation leads to a rich structure of sidebands around the sidebands of the fast modulation. As a result, one expects a large number of resonance sidebands with non-vanishing amplitudes inside the volume V_{beam}, and hence, an increased emittance growth.

In order to illustrate this seeding effect, the resonance widths of all modulation sidebands that reach into the volume V_{beam} are added together. Fig.7.4 shows the quotient of the total volume covered by the modulation sidebands

$$V_{res} = 2 \cdot \sum_{I_{x,(o,l,k,\vec{s})} \in V_{beam}} \Delta_{1/2} I_{x,o,l,k,\vec{s}} \qquad (7.15)$$

and the volume V_{beam} occupied by the particles as a function of the modulation frequencies. The solid line shows the relative volume for a tune modulation with one frequency only, and the dashed line shows the relative volume for a modulation with two frequencies. For the latter the slow modulation frequency was kept at $9Hz$ (the slowest modulation frequency

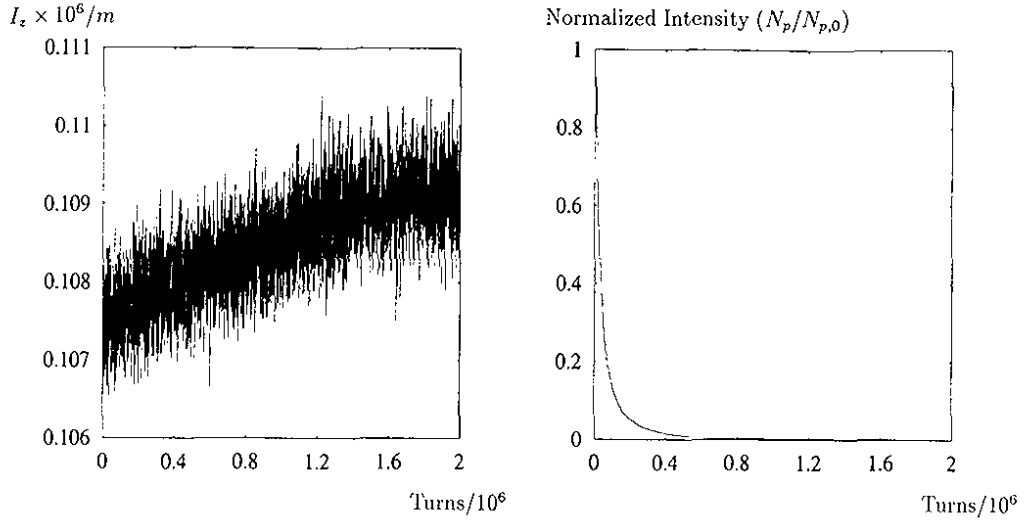

Figure 7.6:
Left hand side: The vertical emittance vs. the number of turns for a tune modulation with one frequency component and $f = 875Hz$, $\triangle Q = 5 \cdot 10^{-3}$.
Right hand side: The normalized number of particles vs. the number of turns for a tune modulation with two frequency components ($f_1 = 875Hz$ and $f_2 = 9Hz$) and a net modulation depth of $\triangle Q = 5 \cdot 10^{-3}$.

used in the SPS experiment) and only the second frequency was varied. In both cases the net modulation depth was $\triangle Q_x = 5.0 \cdot 10^{-3}$, which is approximately twice the modulation depth used in the SPS experiment. Fig.7.4 shows clearly that the relative volume V_{res}/V_{beam} is approximately 14 times larger for a modulation with $9Hz$ and $750Hz$ than for any single modulation frequency and suggests a drastic increase of the particle diffusion due to an increased number of resonances inside the volume V_{beam} and to an overlap of resonance sidebands. Qualitatively, one observes the same effect for any modulation depth, but the volume gain becomes smaller with decreasing modulation depth.

Another way to illustrate the seeding effect and the resulting overlap of resonances inside the volume V_{beam}, is to look at the surface of section. The left-hand side of Fig.7.5 shows the horizontal surface of section for a simultaneous tune modulation with $1350Hz$ and $9Hz$. The modulation depth for the $1350Hz$ signal was $\triangle Q_{1350Hz} = 3.0 \cdot 10^{-3}$ and the modulation depth for the $9Hz$ signal was $\triangle Q_{9Hz} = 1.0 \cdot 10^{-3}$. Even though the modulation depth of each frequency is the same as the ones in Fig.7.3, where no stochastic layer reached inside the volume V_{beam}, the combined effect of both modulation frequencies leads to a stochastic layer inside the volume V_{beam} and thus to a reduction in the dynamic aperture. The right-hand side of Fig.7.5 shows again the horizontal phase space without any tune modulation in order to emphasize the drastic decrease in the dynamic aperture due to the tune modulation.

In the next step the specific effect of the tune modulation on the particle diffusion is analyzed. Using a Gaussian distribution in the action variables, 3000 particles with initial

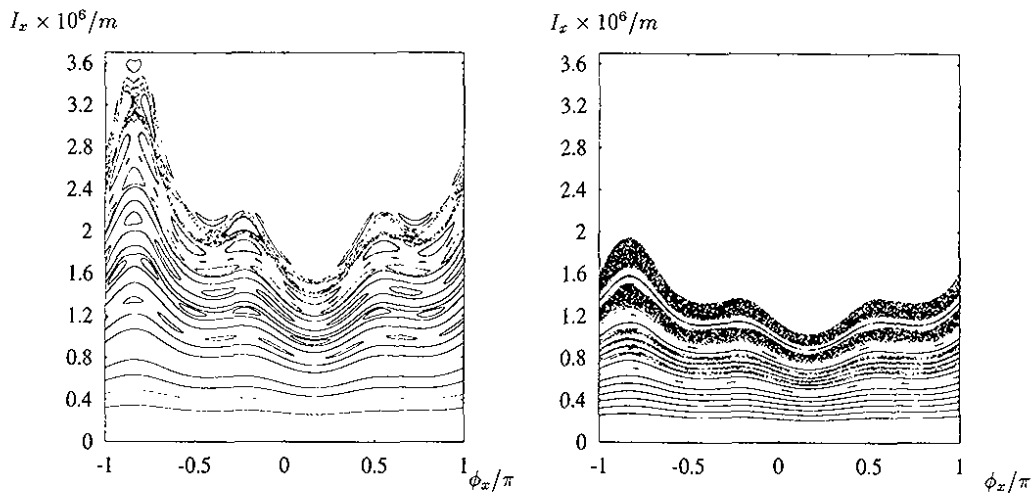

Figure 7.7:
The surfaces of section in the presence of a tune modulation with two approximately equal frequencies.
Left: Tune modulation with $875Hz$ and $\triangle Q = 7.5 \cdot 10^{-3}$.
Right: A tune modulation with $875Hz$ and $766Hz$, and with a net modulation depth of $\triangle Q = 7.5 \cdot 10^{-3}$.

conditions inside the volume V_{beam} are tracked for three different tune modulations. For the numerical simulation a horizontal and vertical aperture limitation of $\pm 40.0mm$ is assumed for the x and z variables. First, the effect of a single modulation frequency is analyzed. For a tune modulation with $\triangle Q = 5 \cdot 10^{-3}$ and a modulation frequency of either $9Hz$ or $875Hz$ the emittance growth is less than 3% and one observes no particle loss over the first $2.0 \cdot 10^6$ turns. The left-hand side of Fig.7.6 shows the vertical emittance as a function of the number of turns for $f = 875Hz$. However, for a simultaneous tune modulation with both frequencies, each having a modulation depth $\triangle Q = 2.5 \cdot 10^{-3}$, all 3000 particles are lost during the first $2.0 \cdot 10^6$ turns. The right-hand side of Fig.7.6 shows the normalized number of particles versus the number of turns. The drastic increase in the particle loss nicely illustrates the seeding effect for a tune modulation with a fast and a slow frequency.

b) Tune modulation with two fast modulation frequencies:

For the following analysis, the two frequencies

$$f_1 = 875Hz, \qquad f_2 = 766Hz$$

are considered. For a tune modulation with $f = 875Hz$ one observes modulation sidebands of the $(7, -176, \vec{0})$ resonance, which reach into the volume V_{beam}. With the help of Equations (7.14), (7.5) and (7.10) one can calculate the position and resonance width of the modulation

sidebands in the horizontal action space.

The $875Hz$ Modulation Sidebands of the $(7,-176,\vec{0})$ Sextupole Resonance			
Sideband Order n	Sign BF	Sideband Action Value I_x	Sideband Width
$+2$	$+$	$2.21 \cdot 10^{-6}m$	$0.07 \cdot 10^{-6}m$
$+1$	$-$	$2.01 \cdot 10^{-6}m$	$0.03 \cdot 10^{-6}m$
0	$-$	$1.80 \cdot 10^{-6}m$	$0.07 \cdot 10^{-6}m$
-1	$+$	$1.60 \cdot 10^{-6}m$	$0.03 \cdot 10^{-6}m$
-2	$+$	$1.39 \cdot 10^{-6}m$	$0.08 \cdot 10^{-6}m$
-3	$-$	$1.16 \cdot 10^{-6}m$	$0.08 \cdot 10^{-6}m$
-4	$+$	$0.92 \cdot 10^{-6}m$	$0.06 \cdot 10^{-6}m$

(7.16)

Table (7.16) lists the corresponding values for the $875Hz$ tune modulation with $\triangle Q = 7.5 \cdot 10^{-3}$. The first column gives the order of the modulation sideband and the order of the Besselfunction in Equation (7.14). The second column lists the sign of the Besselfunction in (7.14). Each change in the sign of the Besselfunction corresponds to a transition of a elliptic fixed point to a hyperbolic fixed point and vice versa. For example, the elliptic fixed points of the $(7,-176,-1)$ resonance sideband have the same angle values as the hyperbolic fixed points of the $(7,-176,0)$ resonance.

The left-hand side of Fig.7.7 shows the modulation sidebands in the horizontal surface of section. The island chain with the smallest action value in the surface of section corresponds to the $(7,-176,-4)$ modulation sideband and the island chain with the largest action value to the $(7,-176,+2)$ modulation sideband of the primary $(7,-176,0)$ resonance. The sideband spacing is determined by the

$$\frac{f_{mod}}{f_{rev}} = 0.0185 \tag{7.17}$$

term in Equation (7.5). Because the spacing of two neighbouring sidebands is larger than the sum of their half-widths, the sidebands do not overlap. Only for action values larger than $1.5 \cdot 10^{-6}m$, the $(7,-176,n)$ modulation sidebands overlap with the sidebands of the other resonances in Table (7.6) and the particle motion becomes irregular. Consequently, one expects only a slow emittance growth for the particles inside the volume V_{beam}.

On the other hand, for a simultaneous tune modulation with both frequencies and with the same net modulation depth, the situation is quite different. The smallest sideband spacing is now determined by

$$\frac{f_{mod,1} - f_{mod,2}}{f_{rev}} = 0.0023. \tag{7.18}$$

The small sideband spacing has two main effects. First, the number of sidebands reaching into the volume V_{beam} increases, and second, neighbouring sidebands might now overlap. Because of the increased number of sidebands and because of the sideband overlap one expects a fast emittance growth for a tune modulation with two approximately equal modulation frequencies.

The right-hand side of Fig.7.7 shows the surface of section for the horizontal particle motion in the presence of the $875Hz$ and the $766Hz$ tune modulation with a total net modulation depth of $\triangle Q = 7.5 \cdot 10^{-3}$. One clearly recognizes the appearance of new resonance sidebands and the wide stochastic layers due to an overlap of the sidebands for a tune modulation with both frequencies. For action values larger than $I = 2.0 \cdot 10^{-6}m$, there is no stable particle motion and the particles are lost within a few thousand turns.

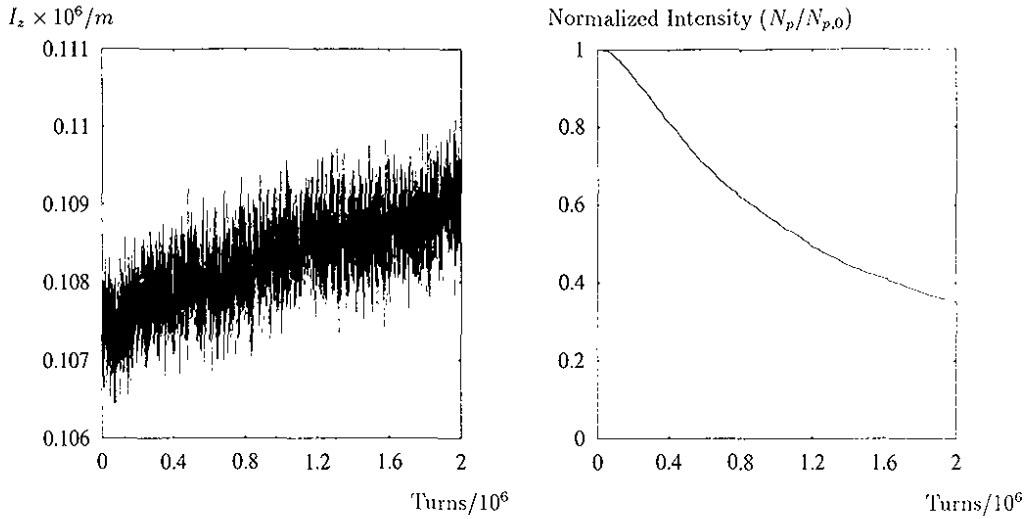

Figure 7.8:
The particle loss due to a tune modulation with two approximately equal frequencies.
Left: The vertical emittance growth for one modulation frequency with $f = 766Hz$ and $\triangle Q = 7.5 \cdot 10^{-3}$.
Right: The normalized intensity for a tune modulation with $875Hz$ and $766Hz$, and with a net modulation depth of $\triangle Q = 7.5 \cdot 10^{-3}$.

Again, the effect of the tune modulation on a particle distribution is illustrated for both frequencies. Choosing again a Gaussian distribution in the action variables with initial coordinates inside the volume V_{beam}, no particles are lost during the first $2.0 \cdot 10^6$ turns for a tune modulation with one frequency only and with $\triangle Q = 7.5 \cdot 10^{-3}$. However, for the simultaneous modulation with both frequencies and with the same net modulation depth, 65% of the particles are lost during the first $2.0 \cdot 10^6$ turns. The right-hand side of Fig.7.8 shows the normalized number of particles versus the number of turns for the simultaneous tune modulation with both frequencies and a net modulation depth of $\triangle Q = 7.5 \cdot 10^{-3}$.

c) Tune modulation with modulation frequencies near the free island oscillation frequency:

The last effect in the discussion of the tune modulation is the widening of the stochastic layers due to a tune modulation with a frequency near the free island oscillation frequency. Choosing the $(7,-176,\vec{0})$ sextupole resonance, the free island oscillation frequency (4.15) becomes

$$\omega_{7,0,-176} = 7 \cdot \sqrt{[\varepsilon^2 \nu_{x,2} + I_{x,res-7} \cdot \varepsilon^4 \nu_{x,4}] \cdot \varepsilon^3 A_{7,0,-176}}. \tag{7.19}$$

Inserting the corresponding values from Tables (7.3) and (7.11), one gets

$$\omega_{7,0,-176} = \frac{2\pi}{L} \cdot \frac{1}{265}. \tag{7.20}$$

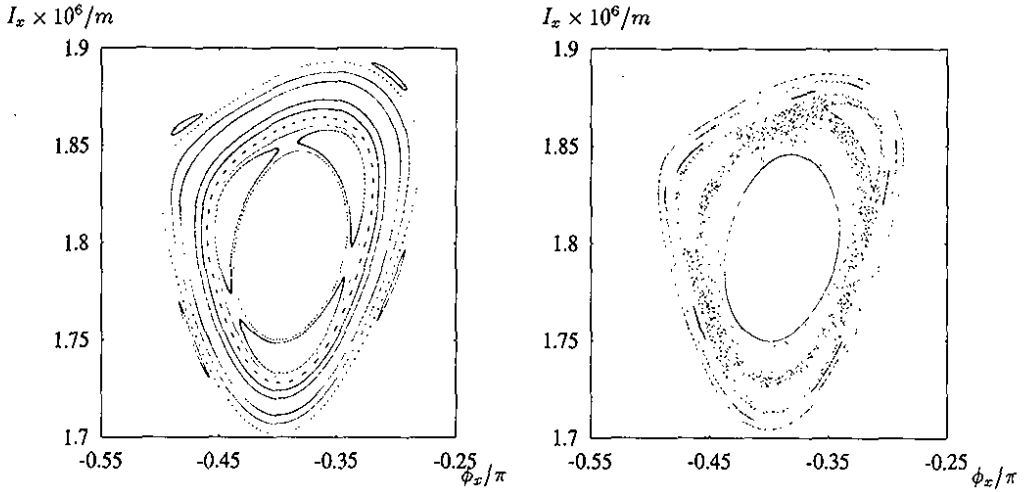

Figure 7.9: *The modulation resonances for a tune modulation with* $754Hz$ *and* $696Hz$*, and with a net modulation depth of* $\Delta Q = 5.0 \cdot 10^{-5}$.
Left: tune modulation with $754Hz$.
Right: tune modulation with both frequencies.

which corresponds to a oscillation frequency of approximately $230Hz$:

$$f_{I,0} = \frac{f_{rev}}{265}. \tag{7.21}$$

Taking the particle coordinates after each passage through the FODO structure, one obtains a stroboscopic projection of the phase space trajectory onto the horizontal phase space. In such a stroboscopic projection, the coordinates circulate around the stable fixed point of the $(7, -176, \vec{0})$ resonance. In the direct neighbourhood of the stable fixed point, the revolution frequency is equal to the free island oscillation frequency $f_{I,0}$. With increasing distance from the stable fixed point, the revolution frequency f_I decreases and reaches its minimum value near the stochastic layer of the resonance.

In case of an external tune modulation that satisfies the relation

$$f_{mod} = N \cdot f_I, \tag{7.22}$$

the tune modulation is in resonance with the oscillation frequency around the stable fixed point of the primary resonance. The islands of such a 'modulational resonance' are depicted in the left-hand side of Fig.7.9. Fig.7.9 shows an enlargement of one of the seven $(7, -176, 0)$ resonance islands in the horizontal surface of section. The left-hand side of Fig.7.9 shows the surface of section in action angle variables for a modulation frequency of $754Hz$ and $\Delta Q = 5.0 \cdot 10^{-5}$. Inside the island of the primary $(7, -176, \vec{0})$ sextupole resonance one recognizes three smaller islands surrounding the stable fixed point of the $(7, -176, \vec{0})$ resonance. For the

fixed points of the three smaller islands, the revolution frequency is related to the modulation frequency by

$$f_I = f_{mod}/3,$$

so that the resonance will be called a third-order modulation resonance. For a modulation with more than one frequency, modulation resonances of the different modulation frequencies can overlap even if they are not close to the separatrix of the sextupole resonance. This overlap of modulation resonances leads to a widening of the stochastic layers even if the modulation frequency is not close to the 'free island' oscillation frequency. Such a widening of the stochastic layer due to an overlap of modulation resonances is depicted in the right-hand side of Fig.7.9 for the two modulation frequencies $f_1 = 754Hz$ and $f_2 = 674Hz$.

The various examples of a tune modulation with more than one frequency component illustrate the damaging effect of an external tune modulation on the particle motion in a storage ring and show how the dynamic aperture can be drastically reduced if the particles are subject to a tune modulation with more than one frequency component. Because one expects in a real storage ring a natural tune modulation with a large number of frequency components (see Section 6), the results of this section suggest the consideration of more than one modulation frequency for a realistic estimate of the dynamic aperture. The following analysis of the drift and diffusion coefficients in the proton beam of HERA assumes the existence of at least two modulation frequencies.

Section 8

Beam-Beam Interaction

A prerequisite for the calculation of drift and diffusion coefficients is the applicability of the single resonance approximation to a Hamilton function with beam-beam potential and an accurate analytical understanding of the resonance structure. Because the beam-beam potential contains an infinite set of Fourier modes, the validity of such an approximation must be carefully analyzed. Furthermore, because the horizontal and vertical tune values of the proton beam in HERA are very close to the coupling resonance, the effect of the coupling resonance on the single resonance approximation must also be taken into consideration. The following two sections discuss these aspects for the beam-beam interaction in HERA and a subsequent third section illustrates the effect of a tune modulation with more than one frequency component for the beam-beam interaction. Because the results of such a discussion should not differ qualitatively for a beam-beam interaction with round or flat electron beams, and because the numerical simulation for a beam-beam interaction with flat beams is much more time consuming than the simulations for round beams, the following sections consider only the case of a beam-beam interaction with round beams. The analysis of a beam-beam interaction with flat beams will be given in Sections (11) and (12), where the analytical estimates of the diffusion rates are compared to the measured drift coefficients in HERA.

8.1 Single Resonance Approximation

Before one can start a diffusion analysis for the beam-beam interaction with tune modulation, one must approximate the Hamiltonian function (3.12) by the standard form of the pendulum Hamiltonian (4.14). This is only possible if the Hamilton function has a non-linear detuning term which fulfills the condition of 'moderate non-linearity' (4.11). This is a severe restriction. Because (3.12) corresponds to a perturbed linear system, the non-linear detuning term might only be of the same order of magnitude as the resonance amplitudes. For this reason, one must carefully analyze the applicability of the pendulum approximation and see whether the approximated Hamiltonian still corresponds to the original system. A convenient way to verify the validity of the single resonance approximation is to compare the resonance structure in the numerically constructed surface of section of (3.12) with the analytic estimates for the single resonance approximation. The following analysis summarizes the work in [60].

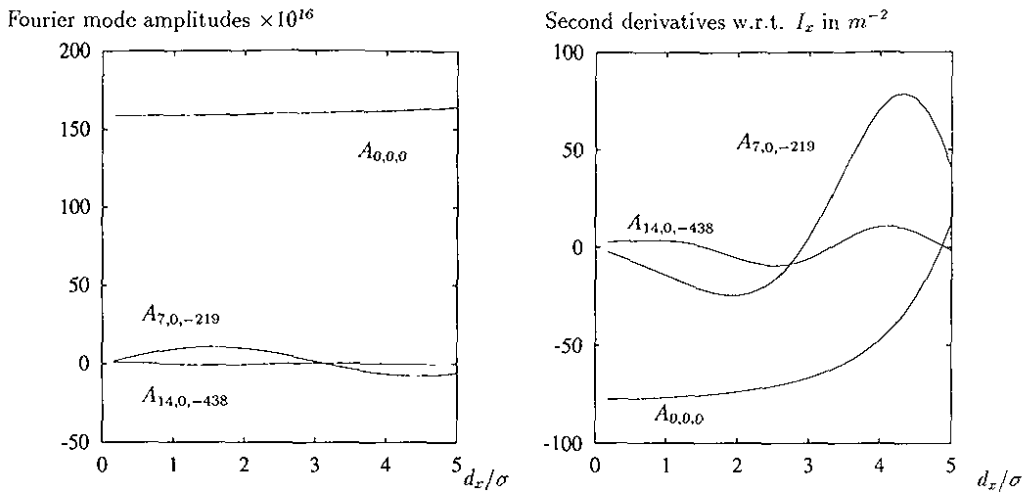

Figure 8.1:
Left: The Fourier mode amplitudes of the $(7,0,-219)$, $(14,0,-438)$, *and* $(0,0,0)$ *resonances for* $I_x = 8.0 \cdot 10^{-9} m, I_z = 0$ *as functions of the beam offset.*
Right: The second derivatives of the mode amplitudes in m^{-2}.

Starting point for the analysis is the beam-beam interaction for round beams with the following parameter values:

Parameter Values		
$Q_x = 31.285$	$L = 6.3 \cdot 10^3 m$	$P_0 = 820 GeV/c$
$f_{rev} = 47.3 KHz$	$\beta_x = 32.04m$	$\beta_y = 31.04m$
$\xi = 0.0015$	$\beta^* = 10.0m$	$\sigma = 0.1mm$
Position of the Beam-Beam Kicks		
$L_1 = 20.13m$	$L_4 = 3154.72m.$	

(8.1)

In order to construct a surface of section for the particle motion in (3.12), the vertical action variable is set to zero ($I_y \equiv 0$).

The starting point for the single resonance approximation is to ignore all but one resonance and the horizontal beam-beam detuning term in (3.12). For the parameter values (8.1), the horizontal particle motion is close to the $(7,0,-219)$ resonance of the beam-beam interaction. Transforming the system to resonance variables via a canonical transformation using the mixed variable generating function

$$F_2 = \dot{I}_x \cdot \left(7\phi_x - \frac{2\pi}{L} \cdot 219 s\right), \tag{8.2}$$

one gets for the single resonance approximation of (3.12):

$$H \approx \nu_x \cdot 7I_x - 219 \cdot \frac{2\pi}{L} \cdot I_x + A_{0,0,0}(I_x, I_z) + \sum_{n=1}^{\infty} A_{n\cdot 7,0,-n\cdot 219} \cdot \cos\left(n\phi_x + \delta\phi_{n\cdot 7,0,-n\cdot 219}\right), \tag{8.3}$$

where the tilde on the new variables has been omitted. The Fourier mode amplitudes $A_{0,0,0}$ and $A_{n\cdot 7,0,-n\cdot 219}$ are calculated by numerical integration of Equation (3.6) and a subsequent FFT. The left-hand side of Fig.8.1 shows the mode amplitudes from the FFT as a function of the beam offset d_x at the interaction region and the right-hand side of Fig.8.1 shows their second derivative with respect to the horizontal action variable I_x. For a beam offset smaller than 0.1σ or approximately equal to 3.0σ, the amplitude of the $(14,0,-438)$ mode is of the same order of magnitude as the one of the $(7,0,-219)$ mode and cannot be neglected in the single resonance approximation. For $d_x < 0.1\sigma$ the single resonance approximation is dominated by the $(14,0,-438)$ Fourier mode and not by the $(7,0,-219)$ mode. If the $(7,0,-219)$ and $(14,0,-438)$ have comparable amplitudes, an analysis of the single resonance approximation must be undertaken with some care. Such a situation is illustrated later on in this section. Furthermore, the right-hand side of Fig.8.1 shows that even if the $(7,0,-219)$ Fourier mode dominates the $(14,0,-438)$ mode, the second derivatives of the mode amplitudes can be of the same order of magnitude and must be included in the single resonance analysis. All other Fourier modes $A_{n\cdot 7,0,-n\cdot 219}$ with $n > 2$ are small compared to the $(7,0,-219)$ and $(14,0,-438)$ modes and can be neglected.

In order to examine the validity of the single resonance approximation, the analytical estimates for the horizontal fixed point values are compared with values obtained by numerical tracking where the full beam-beam interaction is taken into consideration. Using the analytical expression for the horizontal beam-beam detuning (6.14)

$$\frac{\partial A_{0,0,0}}{\partial I_x} = 2 \cdot \xi \frac{4\pi\sigma^2}{\beta^* I_x} \cdot \left[1 - \exp\left(-\frac{\beta^* I_x}{2\sigma^2}\right) \cdot \exp\left(-\frac{d_x^2}{2\sigma^2}\right) I_o\left(\frac{\beta^* I_x}{2\sigma^2}\right) \cdot I_o\left(\frac{2d_x\sqrt{2\beta^* I_x}}{2\sigma^2}\right)\right], \tag{8.4}$$

one can solve the fixed point equations

$$\frac{\partial H}{\partial I_x} = 0; \qquad \frac{\partial H}{\partial \phi_x} = 0. \tag{8.5}$$

As long as the single resonance approximation (8.3) is dominated by only one mode, the fixed point values for the angle variable ϕ_x do not vary with d_x and I_x, and depend only on the position of the beam-beam kicks. The fixed points can be classified according to the linearized equations of motion. Expanding the Hamilton function (8.3) around a fixed point solution of the action-angle variables one gets for the linearized equations of motion

$$\begin{pmatrix} \dot{\Delta I_x} \\ \dot{\Delta\phi_x} \end{pmatrix} = \underline{M} \cdot \begin{pmatrix} \Delta I_x \\ \Delta\phi_x \end{pmatrix}, \tag{8.6}$$

with

$$\underline{M} = \begin{pmatrix} 0 & A \\ B & 0 \end{pmatrix} \tag{8.7}$$

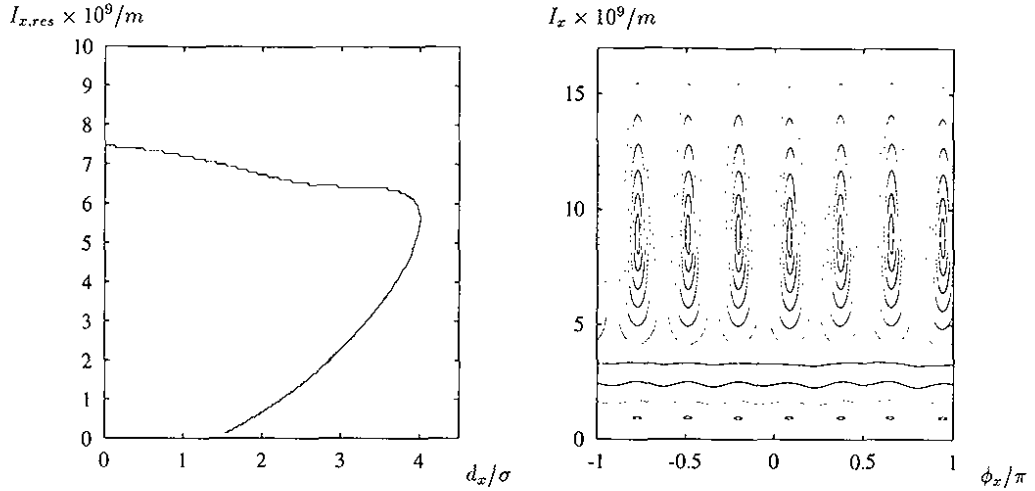

Figure 8.2:
Left: The hyperbolic fixed point value of the action I_x as a function of the beam offset d_x. Right: The surface of section in the action angle variables for $d_x = 2.2\sigma$.

$$A = 49 \cdot \left(\nu_{x,2} + \frac{\partial^2 A_{0,0,0}}{\partial I_x^2} + \sum_{n=1}^{\infty} \frac{\partial^2 A_{n\cdot 7,0,-n\cdot 219}}{\partial I_x^2}\right) \tag{8.8}$$

$$B = \sum_{n=1}^{\infty} \left(n^2 \cdot A_{n\cdot 7,0,-n\cdot 219}\right). \tag{8.9}$$

For $A \cdot B \geq 0$ the two eigenvalues of the matrix (8.7) are real and for $A \cdot B < 0$ the eigenvalues are both purely imaginary. For real eigenvalues the fixed point is of hyperbolic type and for imaginary eigenvalues the fixed point is of elliptic type [14]. Table (8.10) shows the analytically and numerically calculated resonance values of ϕ_x for $d_x = \sigma$ and $I_x = 7 \cdot 10^{-9} m$. The good agreement of the theoretically and numerically calculated values confirms nicely the validity of the single resonance approximation for $d_x = \sigma$ and $I_x = 7 \cdot 10^{-9} m$.

Analytic		Tracking	
$\phi_{elliptic}/\pi$	$\phi_{hyperbolic}/\pi$	$\phi_{elliptic}/\pi$	$\phi_{hyperbolic}/\pi$
−0.771	−0.914	−0.767	−0.907
−0.486	−0.629	−0.480	−0.614
−0.200	−0.343	−0.200	−0.333
0.086	−0.057	0.087	−0.051
0.371	0.229	0.373	0.227
0.657	0.514	0.660	0.520
0.943	0.800	0.947	0.800

(8.10)

The left-hand side of Fig.8.2 shows the fixed point solutions $I_{x,res}$ as a function of the horizontal beam offset d_x with $d_z = 0$ and no tune modulation. It is interesting to note

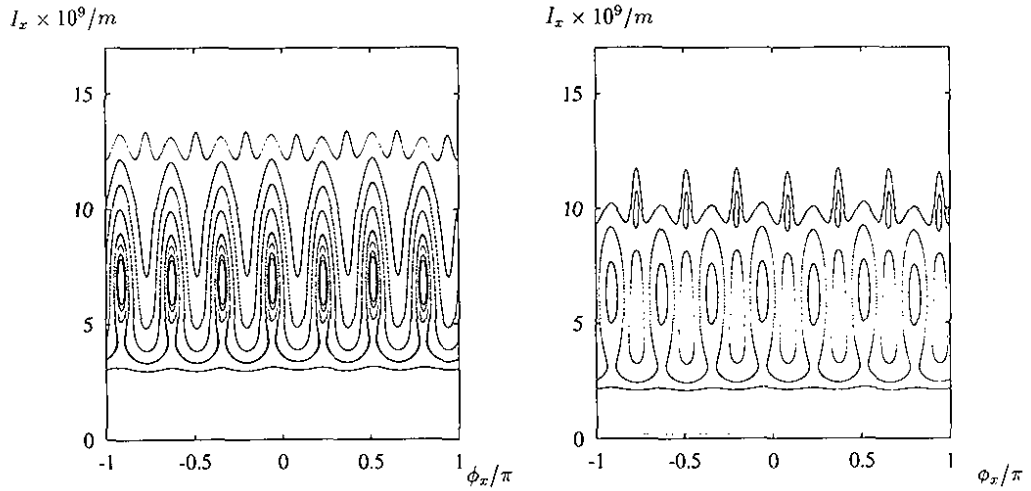

Figure 8.3:
Left: One of the $(7,0,-219)$ *resonances in the surface of section for* $d_x = 4.2\sigma$.
Right: The surface of section in the action angle variables with both $(7,0,-219)$ *resonances for* $d_x = 3.5\sigma$.

that one finds two $(7,0,-219)$ resonances for a horizontal beam offset larger than 1.5σ. The numerical tracking data confirms the appearance of two resonances. The right-hand side of Fig.8.2 shows the surface of section in action angle variables (I_x, ϕ_x) for $d_x = 2.2\sigma$ and clearly shows the two island structures related to these two resonances. With increasing beam offset the two resonances approach each other and finally coincide with one another for $d_x = 4.0\sigma$. According to the analytical solutions of the fixed point equations in the left-hand side of Fig.8.2, the $(7,0,-219)$ resonances should disappear altogether for a beam offset larger than $d_{x,max} = 4.0\sigma$. The numerical data in the left-hand side of Fig.8.3 show the last $(7,0,-219)$ resonance for $d_{x,max} = 4.2\sigma$. The upper resonance has already vanished, but the lower $(7,0,-219)$ resonance is still visible. Because the resonance value of I_x is highly sensitive to the beam offset for $d_x \approx 4.0\sigma$, the minor discrepancy between the analytical and the numerical values for $d_{x,max}$ does not distract from the rather good agreement between the analytical and the numerical data. The lower $(7,0,-219)$ resonance disappears in the numerically constructed surface of section for a beam offset $d_x > 4.2\sigma$. In the right-hand side of Fig.8.3 one sees how the two resonances approached each other for $d_x = 3.5\sigma$.

Motivated by the good agreement of the analytical and numerical results for the fixed point values, the resonance widths and the free island oscillation frequencies of the $(7,0,-219)$ resonance are next calculated and compared with numerical data. First, the resonance half-width is calculated. Neglecting the first derivatives of the Fourier modes in (8.3) and all

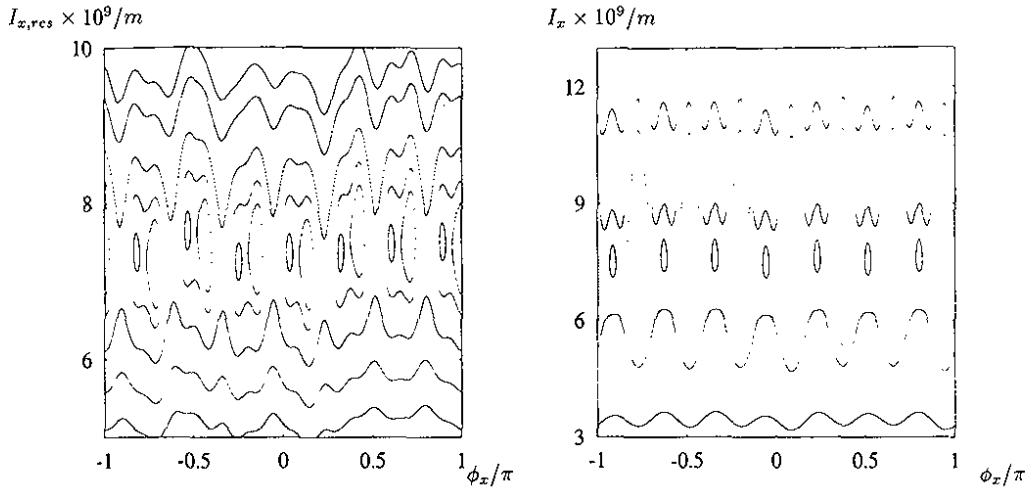

Figure 8.4:
The resonance islands of the $(7,0,-219)$ *and* $(14,0,-438)$ *mode in the horizontal surface of section.*
Left: The resonance islands for a beam offset of $d_x = 0.1\sigma$ *and Fourier mode amplitudes with opposite sign.*
Right: The resonance islands for a beam offset of $d_x = 0.02\sigma$ *and Fourier mode amplitudes with the same sign.*

Fourier modes $A_{n\cdot 7,0,-n\cdot 219}$ with $n > 2$ one gets for the resonance half width

$$\triangle_{\frac{1}{2}} I_{x,max} = \sqrt{\left| \frac{4 \cdot (A_{7,0,-219} + A_{14,0,-438})}{(\nu_{x,2} + \frac{\partial^2 A_{0,0,0}}{\partial I_x^2} + \frac{\partial^2 A_{7,0,-219}}{\partial I_x^2} + \frac{\partial^2 A_{14,0,-438}}{\partial I_x^2})} \right|}. \tag{8.11}$$

Inserting the FFT values for the mode amplitudes and their derivatives into (8.11), the half width $\triangle_{\frac{1}{2}} I_{x,max}$ of the upper resonance in Fig.8.2 varies between $2.0 \cdot 10^{-9} m$ and $7.5 \cdot 10^{-9} m$ for $0.1\sigma < d_x < 1.5\sigma$. The analytical estimate agrees again nicely with the tracking data. Table (8.12) lists the analytical estimate for $d_x = 2.2\sigma$.

The upper $(7,0,-219)$ resonance with $I_{res} = 8.5 \cdot 10^{-9} m$.	
The analytical value $\triangle_{\frac{1}{2}} I_{x,max}$	The numerical value $\triangle_{\frac{1}{2}} I_{x,max}$
$7.0 \cdot 10^{-9} m$	$6.55 \cdot 10^{-9} m$
The lower $(7,0,-219)$ resonance with $I_{res} = 0.9 \cdot 10^{-9} m$.	
The analytical value $\triangle_{\frac{1}{2}} I_{x,max}$	The numerical value $\triangle_{\frac{1}{2}} I_{x,max}$
$0.25 \cdot 10^{-9} m$	$0.22 \cdot 10^{-9} m$

(8.12)

As long as the single resonance approximation (8.3) is dominated by only one Fourier mode, all resonance islands have the same resonance half width. If on the other hand more

than one Fourier mode in (8.3) are of the same order of magnitude, the resonance half width can vary significantly with the angle variable and an analysis of the single resonance approximation must be undertaken with some care. The complexity of this situation is illustrated for the $(7,0,-219)$ and $(14,0,-438)$ mode with approximately equal amplitudes. Depending on whether the $(7,0,-219)$ mode has the same sign as the $(14,0,-438)$ mode, one has to distinguish between two situations. If the mode amplitudes have opposite signs, each resonance island of the $(7,0,-219)$ mode contains two resonance islands of the $(14,0,-438)$ mode. This situation is illustrated in the left-hand side of Fig.8.4 for a beam offset $d_x = 0.1\sigma$ and the parameter values (8.1). If the mode amplitudes have the same sign, the resonance islands are not nested as in the case of mode amplitudes with opposite signs, but the size of the resonance islands changes now considerably with the angle variable. This situation is illustrated in the right-hand side of Fig.8.4 for a beam offset $d_x = 0.02\sigma$ and the parameter values (8.1). One clearly recognizes fourteen resonance islands, half of which are small and the other half are large.

The sign of the $(7,0,-219)$ mode was changed using a tune modulation with

$$\Delta Q_x \cdot f_{rev}/f_{mod} = 0.27. \tag{8.13}$$

Without any tune modulation the $(7,0,-219)$ and $(14,0,-438)$ mode amplitudes have the same sign. With tune modulation the mode amplitudes become

$$\hat{A}_{n\cdot 7,0,-n\cdot 219} = J_0\left(\frac{n\cdot 7\cdot \Delta Q_x \cdot f_{rev}}{f_{mod}}\right)\cdot A_{n\cdot 7,0,-n\cdot 219}. \tag{8.14}$$

While the $(7,0,-219)$ mode amplitude keeps its initial sign for a tune modulation with (8.13), the $(14,0,-438)$ mode amplitude changes its sign under the influence of the tune modulation.

Next, the free island oscillation frequency is calculated. The linearized equations of motion (8.6) can be written as

$$\ddot{\Delta_{\pm}\phi_x} = -\Lambda_{\pm}\cdot \Delta_{\pm}\phi_x, \tag{8.15}$$

with

$$\Lambda_{\pm} = -49\cdot\left(\nu_{x,2} + \frac{\partial^2 A_{0,0,0}}{\partial I_x^2} \pm \frac{\partial^2 A_{7,0,-219}}{\partial I_x^2} + \frac{\partial^2 A_{14,0,-438}}{\partial I_x^2}\right)\cdot(\pm A_{7,0,-219} + 4A_{14,0,-438}) \tag{8.16}$$

and where Δ_+ indicates the expansion of (8.3) around an elliptic fixed point, and Δ_- the expansion around a hyperbolic fixed point. A elliptic fixed point is characterized by $\Lambda \geq 0$ and a hyperbolic fixed point by $\Lambda < 0$. In the case of a elliptic fixed point the free island oscillation frequency ω_0 is equal to the square root of Λ

$$\omega_0 = \sqrt{\Lambda}. \tag{8.17}$$

Inserting the FFT values for the mode amplitudes and their derivatives into (8.16), the resulting free island oscillation frequency of the upper resonance in Fig.8.2 varies between $\omega_0 = 2\pi/(400L)$ and $\omega_0 = 2\pi/(700L)$ for $0.1\sigma < d_x < 1.5\sigma$, which is also in good agreement with the tracking data. For $d_x = 1.5\sigma$ the analytical value of $\omega_0 = 2\pi/(490L)$ agrees nicely with the measured value of $\omega_0 = 2\pi/(475L)$.

An interesting aspect of Equation (8.16) is that for $d_x > 3.3\sigma$ Λ is always positive. This implies that there are no hyperbolic fixed points for $d_x > 3.3\sigma$ and $I_x = I_{x,rms}$. This false

prediction of the single resonance approximation is a consequence of the large second derivatives of the mode amplitudes with respect to the action variable. Looking at the right-hand side of Fig.8.1, one sees that for $d_x > 3.5\sigma$ the absolute value of the second derivative of the $(7,0,-219)$ resonance with respect to the action variable becomes larger than the nonlinear detuning term of the beam-beam kick. Because the second derivative of the $(7,0,-219)$ Fourier mode is larger than the detuning term $A_{0,0,0}$, the condition of moderate nonlinearity (4.11) is not fulfilled and one can not use the single resonance approximation (8.3). The invalidity of the single resonance approximation is also supported by the tracking data. If one looks at the lower resonance structure in the right-hand side of Fig.8.3, the hyperbolic fixed points appear for action values smaller than the resonance action values of the elliptic fixed points but with the same angle values. This discrepancy of the phase space structure in the right-hand side of Fig.8.3 from the resonance structure of the standard pendulum is a consequence of perturbing an integrable linear system with a large non-linear potential.

The above results showed that the applicability of the single resonance approximation must be carefully analyzed for the particle motion in a storage ring with beam-beam interaction and can be summarized as follows [60]. Only for

$$\left|\frac{\partial A_{l,m,k}}{\partial I_x}\right| \ll \frac{1}{2}\left|\frac{\partial^2 A_{0,0,0}}{\partial I_x^2}\cdot \Delta I_x\right| \tag{8.18}$$

$$\left|\frac{\partial^2 A_{l,m,k}}{\partial I_x^2}\right| \ll \left|\frac{\partial^2 A_{0,0,0}}{\partial I_x^2}\right| \tag{8.19}$$

$$\left|\frac{\partial A_{l,\mathrm{m},k}}{\partial I_x}\cdot \Delta I_x\right| \ll |A_{l,m,k}| \tag{8.20}$$

$$\tag{8.21}$$

can one approximate the Hamilton function (3.12) with a single resonance Hamiltonian (8.3). The first two inequalities are generally fulfilled for beam offsets smaller than two sigma. If the condition

$$|A_{n\cdot(l,m,k)}| \ll |A_{l,m,k}| \tag{8.22}$$

is fulfilled, one can furthermore neglect all but one Fourier mode in (8.3).

8.2 Coupling Resonance

Because the proton distribution in HERA lies close to the coupling resonance, one has to include the coupling resonance in the diffusion analysis. Choosing representative proton tunes from the 1993 luminosity runs

Horizontal and Vertical Tune Values in the 1993 Luminosity Runs	
$Q_x = 31.297$	$Q_y \in [32.290, 32.299]$

(8.23)

and the parameter values (8.1), this section looks at the effect of the coupling resonance on the particle motion. For the tune values (8.23), the working point lies close to the coupling resonance and is located between the 7^{th} and 10^{th} order sum resonances. The analysis consists of two parts. In a first step, the work neglects the $A_{l,m,k}$ mode of the single resonance approximation and discusses the particle motion on the unperturbed coupling resonance. In

a second step (Section (8.3)), the $A_{l,m,k}$ mode is reintroduced and the combined effect of an additional tune modulation and the coupling resonance on the single resonance approximation is studied.

For the tune values (8.23) and the parameter values (8.1), the mode amplitudes of the dominating 10^{th} and 7^{th} order sum resonances are much smaller than the coupling mode amplitude and the zeroth order Fourier mode amplitude $A_{0,0,0}$. In a first approximation one can therefore neglect the $A_{l,m,k}$ modes in (3.12). Transforming to new coordinates with a canonical transformation using the mixed variable generating function

$$F_2 = I_+ \cdot \frac{(\phi_x + \phi_z)}{2} + I_- \cdot \left[\frac{(\phi_x - \phi_z)}{2} + \frac{\pi \cdot s}{L}\right], \tag{8.24}$$

one obtains the new variables

$$I_- = (I_x - I_z), \qquad \phi_- = \frac{(\phi_x - \phi_z)}{2} + \frac{\pi \cdot s}{L} \tag{8.25}$$

$$I_+ = I_x + I_z, \qquad \phi_+ = \frac{(\phi_x + \phi_z)}{2}, \tag{8.26}$$

where I_+ corresponds to the sum of the old actions and I_- to the difference of the horizontal and vertical actions. Reintroducing a horizontal tune modulation with one frequency component, one gets for the Hamilton function (3.12) in the new variables (8.25) and (8.26)

$$\begin{aligned} H &= \frac{I_+}{2} \cdot (\nu_x + \nu_z) + \frac{I_-}{2} \cdot \left(\nu_x - \nu_z + \frac{\pi}{L}\right) + A_{0,0,0} \\ &+ \sum_r \left[J_r\left(\frac{2\Delta Q_x f_{rev}}{f_{mod}}\right)\right] \cdot A_{2,-2,2} \cdot \cos\left(4\phi_- + \frac{2\pi}{L} \cdot r \cdot \frac{f_{mod}}{f_{rev}} \cdot s + \delta_{2,-2,2}\right). \end{aligned} \tag{8.27}$$

As the new Hamilton function does not depend on the angle ϕ_+, the total action is a constant of the motion.

Neglecting the tune modulation in (8.27) for the moment and expanding the Equations of motion around the stable fixed points $I_{-,res+}$ and $\phi_{-,res+}$, the equations of motion reduce to the differential equations of a harmonic oscillator with oscillation frequency

$$\omega_{lib} = 2 \cdot \sqrt{\left|A_{2,-2,2} \cdot \left(\frac{\partial^2 A_{0,0,0}}{\partial I_-^2} + \frac{\partial^2 A_{2,-2,2}}{\partial I_-^2} \cdot \cos\left(4\phi_{-,res+} + \delta_{2,-2,2}\right)\right)\right|}, \tag{8.28}$$

and with the linear solutions

$$I_{-,0}(s) = I_{-,res+} - \Delta I_{-,lib} \cdot \cos\left(\omega_{lib} \cdot s + \theta_0\right) \tag{8.29}$$

$$\phi_{-,0}(s) = \phi_{-,res+} + \frac{\omega_{lib}}{A_{2,-2,2}} \Delta I_- \cdot \sin\left(\omega_{lib} \cdot s + \theta_0\right). \tag{8.30}$$

With increasing distance from the stable fixed point, the frequency decreases and approaches zero as I_- reaches the separatrix of the coupling resonance. The motion inside the separatrix is called 'libration' and the motion outside the separatrix 'rotation' [13]. For the parameter

values (8.1) and for ($I_x = I_z$) one gets for example [96]

$I_x = 4.0 \cdot 10^{-9} m = I_z$		
$A_{0,0,0} = 58.4 \cdot 10^{-16}$	$A_{2,-2,2} = -4.41 \cdot 10^{-16}$	$A_{10,0,-313} = 0.0345 \cdot 10^{-16}$
$\frac{\partial^2 A_{0,0,0}}{\partial I_x^2} = -30.0$	$\frac{\partial^2 A_{0,0,0}}{\partial I_x I_z} = -19.0$	$\frac{\partial^2 A_{0,0,0}}{\partial I_z^2} = -30.0$
$\frac{\partial^2 A_{2,-2,2}}{\partial I_x^2} = 1.68$	$\frac{\partial^2 A_{2,-2,2}}{\partial I_x I_z} = -4.22$	$\frac{\partial^2 A_{2,-2,2}}{\partial I_z^2} = 1.35$
$\frac{\partial^2 A_{10,0,-313}}{\partial I_x^2} = -0.29$	$\frac{\partial^2 A_{10,0,-313}}{\partial I_x I_z} = -0.319$	$\frac{\partial^2 A_{10,0,-313}}{\partial I_z^2} = 0.06$
$I_x = 2.4 \cdot 10^{-9} m = I_z$		
$A_{0,0,0} = 48.7 \cdot 10^{-16}$	$A_{2,-2,2} = -3.8 \cdot 10^{-16}$	$A_{10,0,-313} = 0.01 \cdot 10^{-16}$
$\frac{\partial^2 A_{0,0,0}}{\partial I_x^2} = -81.3$	$\frac{\partial^2 A_{0,0,0}}{\partial I_x I_z} = -50.5$	$\frac{\partial^2 A_{0,0,0}}{\partial I_z^2} = -82.3$
$\frac{\partial^2 A_{2,-2,2}}{\partial I_x^2} = 6.85$	$\frac{\partial^2 A_{2,-2,2}}{\partial I_x I_z} = -10.2$	$\frac{\partial^2 A_{2,-2,2}}{\partial I_z^2} = 5.51$
$\frac{\partial^2 A_{10,0,-313}}{\partial I_x^2} = -0.295$	$\frac{\partial^2 A_{10,0,-313}}{\partial I_x I_z} = -0.34$	$\frac{\partial^2 A_{10,0,-313}}{\partial I_z^2} = 0.05$

(8.31)

and thus, for the free island oscillation frequency of the libration

$I_x = 4.0 \cdot 10^{-9} m = I_z$	
Theory	Tracking
$\omega_{lib} \approx 2\pi/(L \cdot 4100)$	$\omega_{lib} \approx 2\pi/(L \cdot 3900)$
$I_x = 2.4 \cdot 10^{-9} m = I_z$	
Theory	Tracking
$\omega_{lib} \approx 2\pi/(L \cdot 2600)$	$\omega_{lib} \approx 2\pi/(L \cdot 2500)$

(8.32)

The tracking data was obtained by a successive application of the map (3.18) to the particle coordinates. The data agree nicely with the analytically calculated values and illustrate the validity of the approximations. Outside the separatrix the ϕ_- phase no longer oscillates but increases with every turn. However, I_- might still oscillate with a small amplitude if the particle motion is close to the separatrix. The frequency for the I_- oscillation during rotation is given by the difference in the horizontal and vertical tunes

$$\begin{aligned} \omega_{rot} &= \frac{4\pi}{L} \cdot \left[Q_x(I_x, I_z) - Q_z(I_x, I_z) + 1\right] \\ &= \frac{2\pi}{L} \cdot \Omega_{rot}, \end{aligned} \tag{8.33}$$

and one can write the linear solutions of the action-angle variables as

$$I_{-,0} = I_{-,rot} + \Delta I_{-,rot} \cdot \cos\left(\omega_{rot} \cdot s + \theta_0\right) \tag{8.34}$$

$$\phi_{-,0} = \phi_{res,rot} + \frac{\omega_{rot}}{4} \cdot s. \tag{8.35}$$

In other words: without any tune modulation the total action I_+ is a constant of motion and the energy of the transversal motion oscillates between the horizontal and vertical plane with a frequency ω_{lib} or ω_{rot}. The action dependent Q-values in equation (8.33) are defined as

$$Q_y(I_x, I_z) = Q_{y,0} + \frac{\partial A_{0,0,0}}{\partial I_y}, \qquad y = x, z; \tag{8.36}$$

where $Q_{y,0}$ are the linear Q-values.

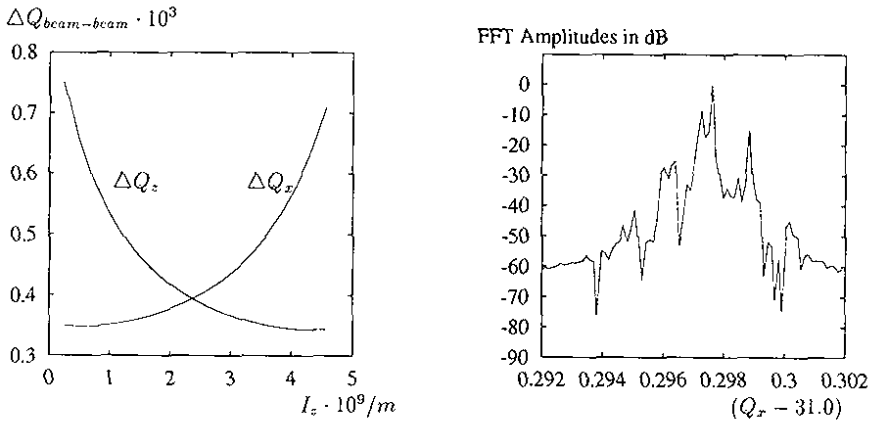

Figure 8.5:
Left: The horizontal and vertical beam-beam detuning ΔQ due to the I_- oscillation on the beam-beam coupling resonance for $(I_x + I_z) = 4.8 \cdot 10^{-9}m$.
Right: The horizontal Fourier spectrum for the particle motion on the coupling resonance with tune modulation and beam-beam interaction.

The energy oscillation has a dramatic effect on the horizontal and vertical tunes. Because of the change in I_x and I_z during the I_- oscillation, the horizontal and vertical Q-values also oscillate due to the beam-beam detuning and change the resonance positions in the action space. For example, for $(< I_x >= 2.4 \cdot 10^{-9}m =< I_z >)$, the horizontal and vertical detuning ΔQ varies between $(\Delta Q_x = 0.35 \cdot 10^{-3})$ and $(\Delta Q_x = 0.7 \cdot 10^{-3})$. The left-hand side of Fig.8.5 shows the horizontal and vertical detuning as a function of the vertical action I_z with the constraint $(I_x + I_z) = 4.8 \cdot 10^{-9}m$. The right-hand side of Fig.8.5 shows the horizontal FFT spectrum of one particle on the coupling resonance with a fast tune modulation of $1200Hz$ and $50Hz$. (The spectrum shows the fractional part of the horizontal Q_x-value.) One clearly recognizes the first two upper and lower $50Hz$ sidebands around the horizontal Q-value $(Q_x = 31.2978)$. Each sideband has a spacing of $\Delta Q_x(50Hz) \approx 1.25 \cdot 10^{-3}$ and splits again into sidebands of a $16.5Hz$ modulation due to the motion on the coupling resonance. The spacing of these additional sidebands is $\Delta Q_x(16Hz) \approx 1/2900$, which corresponds nicely to the free island oscillation frequency in Table (8.32).

In a second step, a horizontal tune modulation is reintroduced. For the fast tune modulation $(f_{mod} > 50Hz)$, the sidebands of the coupling resonance might overlap, but because of the small argument in the Bessel functions, the overlap can only lead to a small stochastic layer around the separatrix of the coupling resonance. For a slow tune modulation $(f_{mod} < 10Hz)$, the trapping condition is fulfilled and the tune modulation leads again only to a small stochastic layer around the separatrix of the coupling resonance. The tune modulation leads to a wide stochastic layer only for a modulation frequency close to the free island oscillation frequency. The 'phase diagram' of the coupling resonance illustrates the situation in Fig.8.6. For the parameter values (8.1) the 'free island' oscillation frequency is close to one of the strong

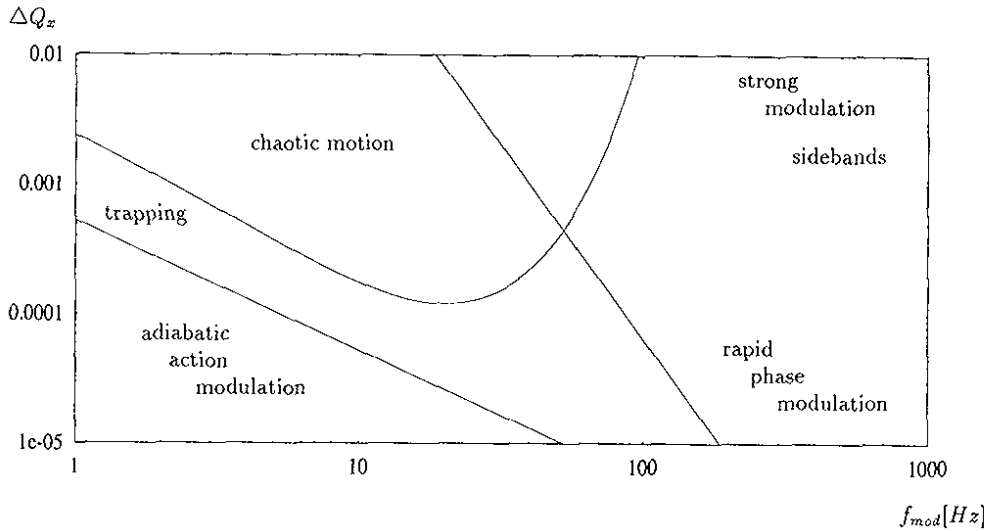

Figure 8.6: *The phase diagram for the coupling resonance of the beam-beam interaction.*

resonance lines from the vibrations of the vacuum pumps and one expects a wide stochastic layer of the coupling resonance for a tune modulation with $f_{mod} \approx 16Hz$ and $\Delta Q_x > 10^{-4}$. If one introduces an additional linear coupling of $\Delta Q_{coup.} \approx 3.0 \cdot 10^{-3}$, the 'free island' oscillation frequency of the coupling resonance is of the order of $100Hz$ and one expects a wide stochastic layer for a tune modulation with the free island oscillation frequency.

Another important quantity for the diffusion analysis is the resonance width in the transverse Q-space. For $I_x \approx I_z$ and $(Q_x - Q_z + 1 = 0)$, the particles are right on the $(2, -2, 2)$ coupling resonance. Keeping the Q_x-value constant and decreasing Q_z, the particles will leave the coupling resonance for $(Q_x - Q_z + 1 > \Delta Q_{res})$. ΔQ_{res} represents the width of the coupling resonance in the transverse Q-space. The tracking data yields for the resonance width

$$\Delta Q_{res} = 2.8 \cdot 10^{-4}. \tag{8.37}$$

For $(Q_x - Q_z + 1 > \Delta Q_{res})$ the motion changes from libration to rotation and one has to use (8.34) and (8.35) rather than the linear solutions (8.29) and (8.30).

8.3 Tune Modulation

The particles inside the proton beam can not probe the whole range of the transverse phase space but only a small fraction of it. The phase space volume V_{beam} accessible to the particles inside the proton beam can be expressed in terms of the action-angle variables by

$$I_y \in [0.0m; 10.0 \cdot 10^{-9}m], \qquad \phi_y \in [-\pi; +\pi], \qquad y = x, z, \tag{8.38}$$

where the upper boundary for the action variables corresponds to a normalized beam emittance of $17 \cdot 10^{-6}m$. Without any tune modulation and the parameter values (8.1), the

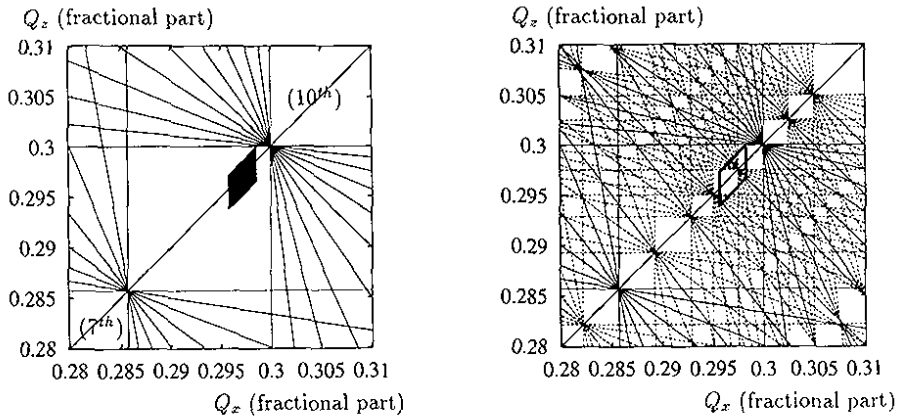

Figure 8.7: *A particle distribution in the transverse Q-diagram.*
Left: The resonance lines up to 10^{th} order in x and z without any tune modulation.
Right: The resonance lines and their sidebands for a fast tune modulation with $1200Hz$.

phase space volume V_{beam} occupied by the particles and given by (8.38) contains no low-order sum resonances. The left-hand side of Fig.8.7 shows a proton distribution in the transverse Q-space. The particles are located in the direct neighbourhood of the coupling resonance, between the 7^{th} and 10^{th} order sum resonances. The Q-diagram shows the horizontal and vertical resonances up to 10^{th} order in x and z. Without tune modulation the resonance condition reads

$$l \cdot Q_x(I_x, I_z) + m \cdot Q_y(I_x, I_z) + k = 0, \qquad l, m, k \in \mathbf{Z}. \tag{8.39}$$

In the case of a harmonic tune modulation the situation is quite different. With tune modulation the resonance condition reads

$$l \cdot Q_x(I_x, I_z) + m \cdot Q_y(I_x, I_z) + n \cdot \frac{f_{mod}}{f_{rev}} + k = 0, \qquad l, m, k, n \in \mathbf{Z}, \tag{8.40}$$

and the tune modulation leads to a set of additional resonance sidebands. For a tune modulation with more than one modulation frequency the sidebands are characterized by the vector

$$(f_1, n_1, f_2, n_2, ..., f_N, n_N), \tag{8.41}$$

where n_j labels the order of the modulation sideband of the frequency f_j.

For a fast tune modulation the modulation sidebands might not overlap, but reach into the phase space volume V_{beam}, so that the particle motion might lie on a sideband of a non-linear sum resonance. In the following these modulation sidebands are called 'seeding resonances', as they form the resonance seeds for the stochastic layer due to an additional slow tune modulation. The right-hand side of Fig.8.7 shows the Q-diagram for the same particle distribution as in the left-hand side of Fig.8.7, but with the resonance sidebands of a fast tune

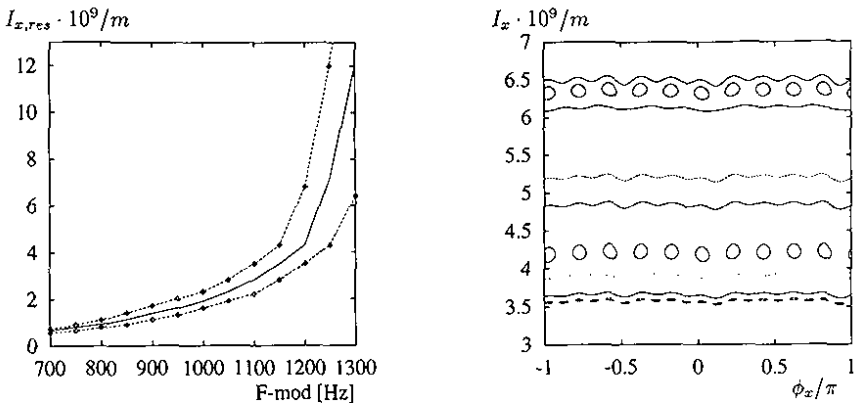

Figure 8.8: *The position of the seeding sidebands for the horizontal $(10, 0, -313)$ resonance of the beam-beam potential and the parameter values (8.1).*
Left: The position as a function of the modulation frequency. The solid line shows the position of the $(f_1 = 1200Hz, n_1 = 1, f_2 = 50Hz, n_2 = 0)$ seeding resonance, and the lines with dots show the positions of the lower and upper $50Hz$ sidebands: $(f_1 = 1200Hz, n_1 = 1, f_2 = 50Hz, n_2 = \pm 1)$.
Right: The corresponding resonance islands in the surface of section for $I_z \equiv 0$ and $\triangle Q_{1200Hz} = 1.25 \cdot 10^{-4}$ and $\triangle Q_{50Hz} = 3.13 \cdot 10^{-4}$.

modulation with $1200Hz$. One clearly recognizes the new resonance lines in the area covered by the particle distribution.

The following analysis considers a fast tune modulation with

$f_{fast,1} = 1200Hz$	$\triangle Q_{fast,1} \in [1.25 \cdot 10^{-4},\ 1.25 \cdot 10^{-3}]$
$f_{fast,2} = 50Hz$	$\triangle Q_{fast,2} \in [0,\ 4.38 \cdot 10^{-4}]$

(8.42)

as it might occur due to the imperfections of the HERA-p power supplies (see Section 6).

Using the expression of the non-linear detuning term of the beam-beam interaction (6.14), one can calculate the resonance position as a function of the modulation frequency. The left-hand side of Fig.8.8 shows the position of the horizontal $(10, 0, -313)$ seeding resonances for the parameter values (8.1) and $(I_z \equiv 0)$ as a function of the modulation frequency. The solid line shows the position of the $(f_1 = 1200Hz, n_1 = 1, f_2 = 50Hz, n_2 = 0)$ seeding resonance and the dashed lines with dots show the upper and lower $50Hz$ sidebands around the $1200Hz$ seeding resonance: $(f_1 = 1200Hz, n_1 = 1, f_2 = 50Hz, n_2 = \pm 1)$. As the fast modulation frequency increases, the seeding resonances move to larger I_x values and the $(f_1 = 1200Hz, n_1 = 1, f_2 = 50Hz, n_2 = \pm 1)$ seeding resonances move away from each other. In the right-hand side of Fig.8.8 one sees the corresponding resonance islands for $\triangle Q_{1200Hz} = 1.25 \cdot 10^{-4}$ and $\triangle Q_{50Hz} = 3.13 \cdot 10^{-4}$ in the horizontal surface of section. The island chain in the middle corresponds to the $(f_1 = 1200Hz, n_1 = 1, f_2 = 50Hz, n_2 = 0)$ seeding resonance

and the island chains at the top and bottom of Fig.8.8 are the ($f_1 = 1200Hz, n_1 = 1, f_2 = 50Hz, n_2 = \pm 1$) sidebands of the $50Hz$ modulation. For $I_x = 3.4 \cdot 10^{-9}m$ the $(20, 0, -626)$ resonance sideband becomes more dominant than the one of the $(10, 0, -313)$ mode, and one sees twenty resonance islands, rather than ten for the lower $50Hz$ sideband. Fig.8.8 illustrates the good agreement between the resonance positions calculated with the FFT mode amplitudes and the tracking data. For $I_z = 0$ the analytically calculated resonance positions from the left-hand side of Fig.8.8 agree nicely with the island positions in the right-hand side of Fig.8.8. With increasing ΔQ_{1200Hz} the widths of the seeding sidebands increase, but they will never overlap with each other unless an additional modulation frequency is introduced. Thus, without any additional tune modulation, the seeding resonances have only a small stochastic layer and do not lead to a drastic increase in the particle diffusion. Only in combination with an additional slow tune modulation or an explicitly stochastic signal can the seeding resonances of the fast tune modulation cause a strong particle diffusion.

Because the low order sidebands of the $(7, 0, -219)$ resonance can not reach into the volume V_{beam} for the parameter values (8.1), the following analysis considers only the $(10, 0, -313)$ resonance. However, for other parameter values other sum resonances might also gain importance and require inclusion in the diffusion analysis.

With the help of the numerical integration of the beam-beam potential (3.6) and a subsequent FFT, one can calculate the mode amplitudes of the coupling and the $(10, 0, -313)$ resonance. Table (8.44) lists the amplitudes for a non-vanishing vertical action, and Table (8.43) lists the amplitudes for ($I_x = 4.8 \cdot 10^{-9}m, I_z \equiv 0$), as it applies for the $1200Hz$ modulation sideband in the right-hand side of Fig.8.8.

$I_x = 4.8 \cdot 10^{-9}m;$	$I_z = 0.0m$
$A_{0,0,0} = 44.0 \cdot 10^{-16}$	$A_{10,0,-313} = 0.26 \cdot 10^{-16}$
$\frac{\partial^2 A_{0,0,0}}{\partial I_x^2} = -37.0$	$\frac{\partial^2 A_{10,0,-313}}{\partial I_x^2} = -1.28$

(8.43)

$I_x = 4.0 \cdot 10^{-9}m = I_z$		
$A_{0,0,0} = 58.4 \cdot 10^{-16}$	$A_{2,-2,2} = -4.41 \cdot 10^{-16}$	$A_{10,0,-313} = 0.0345 \cdot 10^{-16}$
$\frac{\partial^2 A_{0,0,0}}{\partial I_x^2} = -30.0$	$\frac{\partial^2 A_{0,0,0}}{\partial I_x I_z} = -19.0$	$\frac{\partial^2 A_{0,0,0}}{\partial I_z^2} = -30.0$
$\frac{\partial^2 A_{2,-2,2}}{\partial I_x^2} = 1.68$	$\frac{\partial^2 A_{2,-2,2}}{\partial I_x I_z} = -4.22$	$\frac{\partial^2 A_{2,-2,2}}{\partial I_z^2} = 1.35$
$\frac{\partial^2 A_{10,0,-313}}{\partial I_x^2} = -0.29$	$\frac{\partial^2 A_{10,0,-313}}{\partial I_x I_z} = -0.319$	$\frac{\partial^2 A_{10,0,-313}}{\partial I_z^2} = 0.06$
$I_x = 2.4 \cdot 10^{-9}m = I_z$		
$A_{0,0,0} = 48.7 \cdot 10^{-16}$	$A_{2,-2,2} = -3.8 \cdot 10^{-16}$	$A_{10,0,-313} = 0.01 \cdot 10^{-16}$
$\frac{\partial^2 A_{0,0,0}}{\partial I_x^2} = -81.3$	$\frac{\partial^2 A_{0,0,0}}{\partial I_x I_z} = -50.5$	$\frac{\partial^2 A_{0,0,0}}{\partial I_z^2} = -82.3$
$\frac{\partial^2 A_{2,-2,2}}{\partial I_x^2} = 6.85$	$\frac{\partial^2 A_{2,-2,2}}{\partial I_x I_z} = -10.2$	$\frac{\partial^2 A_{2,-2,2}}{\partial I_z^2} = 5.51$
$\frac{\partial^2 A_{10,0,-313}}{\partial I_x^2} = -0.295$	$\frac{\partial^2 A_{10,0,-313}}{\partial I_x I_z} = -0.34$	$\frac{\partial^2 A_{10,0,-313}}{\partial I_z^2} = 0.05$

(8.44)

Table (8.45) lists the resulting values of the free island oscillation frequencies.

Free Island Oscillation Frequencies of the Resonance Sidebands		
$I_x = 4.8 \cdot 10^{-9}m, I_z \equiv 0$	$I_x = 2.4 \cdot 10^{-9}m = I_z$	$I_x = 4.0 \cdot 10^{-9}m = I_z$
$f_{I,res} = 3.7Hz$	$f_{I,res} = 1.0Hz$	$f_{I,res} = 1.2Hz$
Free Island Oscillation Frequencies for the Coupling Resonance		
$I_x = 4.8 \cdot 10^{-9}m, I_z \equiv 0$	$I_x = 2.4 \cdot 10^{-9}m = I_z$	$I_x = 4.0 \cdot 10^{-9}m = I_z$
/	$f_{I,coup} = 18.2Hz$	$f_{I,coup} = 11.8Hz$

(8.45)

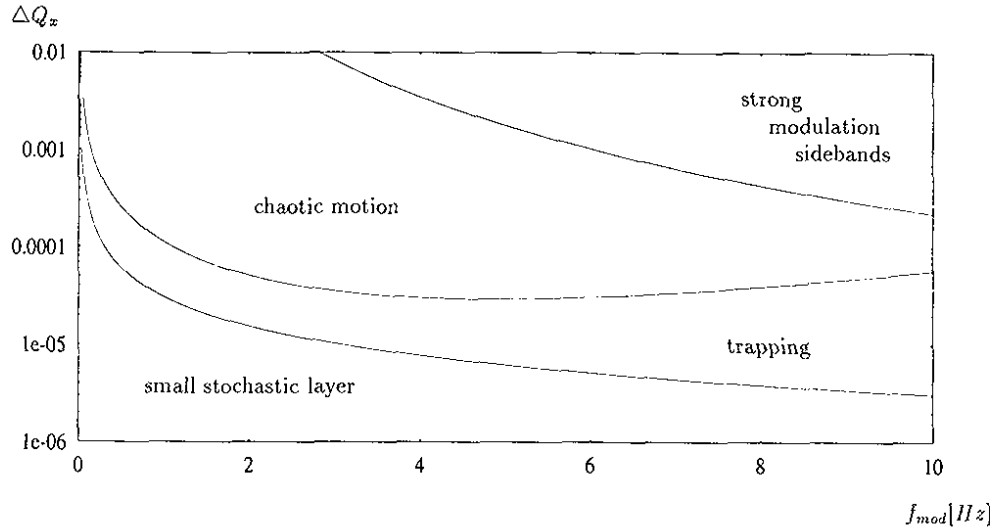

Figure 8.9:
The phase diagram for the $1200Hz$ *modulation sideband of the* $(10, 0, -313)$ *sum resonance of the beam-beam interaction with* $\Delta Q_{1200Hz} = 3.13 \cdot 10^{-4}$.

Depending on the number of modulation frequencies, their depths and values, an additional slow tune modulation can lead to three qualitatively different situations, as it was discussed in Section (5):

a) the tune modulation leads to a small stochastic layer around the separatrix of a nonlinear resonance,
b) the overlap of a large number of modulation sidebands leads to a homogeneous modulational layer,
c) the sideband overlap leads to a non-uniform modulational layer, which captures regions of stable motion.

Again, the different regions in the parameter space of the slow tune modulation can be nicely illustrated with a phase diagram. Fig.8.9 shows the phase diagram for the $1200Hz$ modulation sideband of the $(10, 0, -313)$ resonance with $\Delta Q_{1200} = 3.13 \cdot 10^{-4}$. For a given set of machine parameters the phase diagram depends only on the free island oscillation frequency of the fast modulation sideband. Consequently, one expects qualitatively similar phase diagrams for all modulation sidebands. With decreasing modulation depth of the fast tune modulation, the free island oscillation frequency of the resonance sideband decreases, shifting the region of chaotic particle motion in the phase diagram to lower modulation frequencies and depths. This shift can be seen by comparing Fig.8.9 to the phase diagram of the coupling resonance in Fig.8.6. Both phase diagrams use the same parameter values (8.1) and differ only in the free island oscillation frequency of the primary resonance. While the free island oscillation frequency of the coupling resonance is $f_{I,coup.} \approx 16Hz$, the corresponding frequency in Fig.8.9

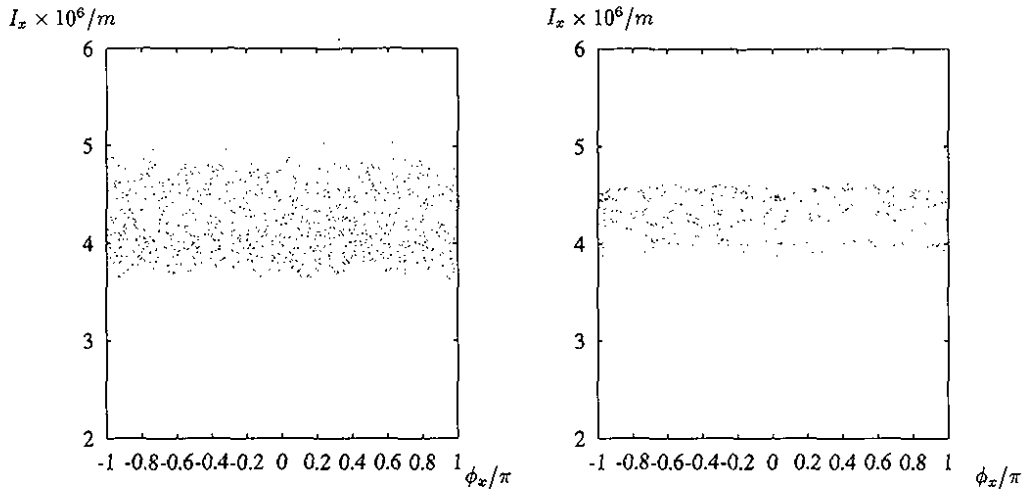

Figure 8.10:
The surface of section for the horizontal particle motion.
Left: A tune modulation with one fast ($f_{fast} = 1200Hz$) and one slow ($f_{slow} = 6Hz$) frequency component with $\Delta Q_{1200Hz} = 3.13 \cdot 10^{-4}$ and $\Delta Q_{6Hz} = 3.13 \cdot 10^{-5}$.
Right: A tune modulation with one fast ($f_{fast} = 1200Hz$) and two slow ($f_{1,slow} = 6Hz$, $f_{2,slow} = 9Hz$) frequency components with $\Delta Q_{1200Hz} = 5.0 \cdot 10^{-5}$ and $\Delta Q_{slow} = 5.0 \cdot 10^{-5}$.

is $f_{1,res} \approx 4Hz$. Because of the much smaller free island oscillation frequency in Fig.8.9, the region of chaotic motion clearly is shifted to lower modulation frequencies and depths, in comparison to the phase diagram of the coupling resonance Fig.8.6.

It is interesting to note that the frequency spectrum of the tune modulation caused by the ground motion falls right into the region of chaotic particle motion in Fig.8.9. As was shown in Section (6), the frequency spectrum of the slow tune modulation covers the whole frequency range [88]:

$$f_{slow} \in [0Hz, 10Hz], \qquad \Delta Q_{slow} \sim 5 \cdot 10^{-5}, \tag{8.46}$$

with a particularly large modulation depth for $f_{slow} = 6Hz$. Consequently, one expects a wide modulational layer around the $1200Hz$ seeding resonance for an additional slow tune modulation with $f_{slow} = 6Hz$. The left-hand side of Fig.8.10 shows the resulting modulational layer in the horizontal surface of section for $\Delta Q_{1200Hz} = 3.13 \cdot 10^{-4}$ and $\Delta Q_{6Hz} = 3.13 \cdot 10^{-5}$.

The fact that the spectrum of the slow tune modulation covers the whole frequency range between $1Hz$ and $10Hz$ has another interesting implication. Even if the tune modulation with one single frequency does not lead to a modulational layer, the combined effect of more than one slow modulation frequency can lead to a wide modulational layer. For example, for a seeding resonance with $f_{fast} = 1200Hz$ and $\Delta Q_{fast} = 5 \cdot 10^{-5}$, one single modulation frequency in the range between $1Hz$ and $10Hz$ and a modulation depth of $\Delta Q_{slow} = 5 \cdot 10^{-5}$ does not lead

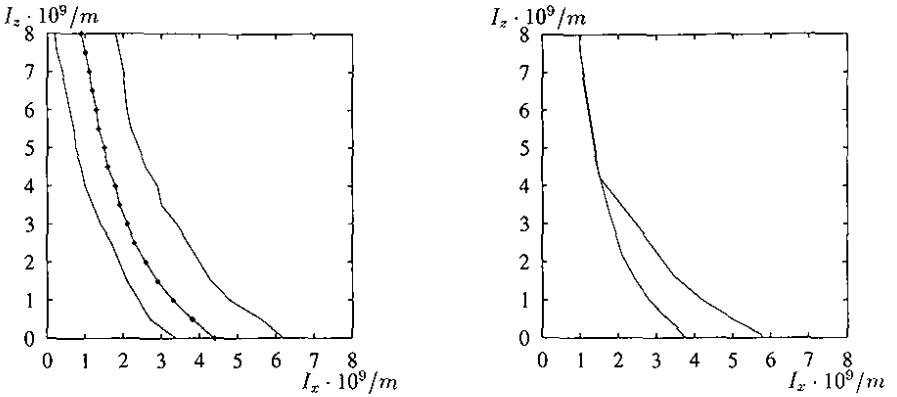

Figure 8.11:
Left: The position of the $(10, 0, -313)$ resonance sidebands in the horizontal action space for $Q_x = 31.297$ and $Q_z = 32.297$. The line with dots shows the positions of the ($f_1 = 1200Hz, n_1 = 1, f_2 = 50Hz, n_2 = 0$) seeding resonance, and the two solid lines the position of the ($f_1 = 1200Hz, n_1 = 1, f_2 = 50Hz, n_2 = \pm 1$) seeding resonances.
Right: The modulational layer around the ($f_1 = 1200Hz, n_1 = 1, f_2 = 50Hz, n_2 = 0$) seeding resonance. The solid lines represent the upper and lower boundary of the modulational layer.

to chaotic particle motion. However, for a simultaneous slow tune modulation with $f_{slow,1} = 9Hz$ and $f_{slow,2} = 6Hz$, both having a modulation depth of $\Delta Q_{slow} = 5 \cdot 10^{-5}$, the tune modulation leads to a wide modulational layer around the $1200Hz$ seeding resonance. This aspect is again illustrated with the surface of section for the purely horizontal particle motion. The right-hand side of Fig.8.10 shows the resulting modulational layer for a simultaneous slow tune modulation with $f_{slow,1} = 9Hz$ and $f_{slow,2} = 6Hz$. A remarkable aspect of the data in the right-hand side of Fig.8.10 is that even modulation amplitudes as small as $\Delta Q = 5.0 \cdot 10^{-5}$ can lead to a wide modulational layer.

The above examples show that a fast tune modulation as it is caused by the ripples in the HERA-p power supplies, together with an additional slow tune modulation due to the ground motion in the HERA tunnel, can lead to an irregular particle motion and thus to emittance growth. If additional frequency components are included, as for example the strong $50Hz$ and $150Hz$ components in the HERA-p power supplies, the resulting modulational layer can cover large regions of the phase space. But before one can analyze the resulting emittance growth in the proton beam, one has to look at the effect of the coupling resonance on the seeding resonance.

Because the action variables I_x and I_z oscillate on the coupling resonance, one can not limit the resonance analysis to one resonance position in the action space but must examine the position and width of the modulational layer in the whole horizontal action space. The left-hand side of Fig.8.11 shows the resulting positions of the $1200Hz$ and $50Hz$ sidebands

in the transverse action space for the horizontal $(10, 0, -313)$ sum resonance. The abscissa corresponds to the horizontal and the ordinata to the vertical action. The solid line with dots shows the $(f_1 = 1200Hz, n_1 = 1, f_2 = 50Hz, n_2 = 0)$ seeding resonance and the two lines without dots show the upper and lower $(f_1 = 1200Hz, n_1 = 1, f_2 = 50Hz, n_2 = \pm 1)$ sidebands. The right-hand side of Fig.8.11 shows the resonance width of the modulational layer around the $1200Hz$ seeding resonance with $(\triangle Q_{i200Hz} = 3.2 \cdot 10^{-4})$ for a slow tune modulation with $0.6Hz$ and $\triangle Q_{0.6Hz} = 6.25 \cdot 10^{-5}$. The solid lines represent the upper and lower boundaries of the modulational layer. Because the horizontal and vertical tunes change during the action oscillations on the coupling resonance, the particles periodically leave the modulational layer. For $I_x > I_z$, the particles are inside the layer, and for $I_x < I_z$, the particles are outside the layer. Hence, for large oscillation amplitudes, the particles experience the random motion inside the modulational layer only during every second half period of the I_x/I_z oscillation. For all other 10^{th} order sum resonances a similar resonance pattern results.

We are now ready to analyze the particle diffusion and to calculate estimates of the drift and diffusion coefficients. In the next sections, the diffusion mechanisms are introduced and the resulting analytical estimates are compared with tracking data.

Section 9

Diffusion Mechanisms

The discussion of the drift and diffusion coefficients consists of fife parts. The first part presents the mechanism of the modulational diffusion due to the combined effect of non-linear fields and a harmonic tune modulation and a second part discusses the effect of an additional random tune modulation. The third part briefly summarizes the main aspects of the stochastic pump diffusion. A fourth part discusses the stochastic excitation of the proton beam due to the combined effect of RF-noise in the electron cavities and the beam-beam interaction and the fifth part summarizes the particle diffusion due to intra-beam scattering.

9.1 Modulational Diffusion

In this Section the main aspects of the modulational diffusion are summarized. A detailed description of the diffusion mechanism can be found in [54][13][97][98]. However, there are three important differences between the particle dynamics in our model structure and the assumptions made in [54][13][97] and [98]. In [54][13], the authors assume a perturbed non-linear system with a coupling that is small in relation to the driving resonance and look only at one modulation frequency. In our model structure, we are dealing with a perturbed linear system and a coupling that is large in relation to the driving resonance. Furthermore, our diffusion analysis is not limited to only one modulation frequency, but incorporates the combined effect of slow and fast frequency components. Therefore, the diffusion analysis must be modified before it can be applied to the Hamilton function (3.12).

The time evolution of the actions I_x and I_z is determined by Hamilton's equations

$$\frac{dI_y}{ds} = -\frac{\partial H}{\partial \phi_y}, \quad y = x, z. \tag{9.1}$$

Looking only at the change in the total action I_+ (8.26), one can define a scalar diffusion and drift coefficient

$$D(I_x, I_z) = \frac{< \triangle I_+^2 >_\phi}{2T}, \tag{9.2}$$

$$B(I_x, I_z) = \frac{< \triangle I_+ >_\phi}{2T},$$

with

$$\triangle I_+ = -\int_{-T}^{T} \frac{\partial H}{\partial \phi_+}. \tag{9.3}$$

For Hamiltonian systems the drift coefficient can be calculated using the partial derivative of the diffusion coefficient with respect to the diffusing action variable [13]:

$$B(I_x, I_z) = \frac{1}{2} \cdot \frac{\partial D}{\partial I_+}(I_x, I_z). \tag{9.4}$$

Using Equations (9.2), (9.3), and (9.4) one can derive analytical estimates for the emittance growth due to the non-linear aspects of the particle motion.

The results of Sections (4) and (5) showed that the non-linear aspects of the particle motion lead only to a diffusion-like process if the resonance structure of the system forms stochastic layers around the primary resonances. For a slow tune modulation the stochastic layers can be extremely wide and are called modulational layers [54]. Inside a modulational layer, the horizontal and vertical actions do not stay constant, leading to a non-oscillating variation of the horizontal and vertical tunes:

$$\nu_x(I_x, I_z) = \frac{2\pi}{L} Q_x + \frac{\partial A_{0,0,0}}{\partial I_x}(I_x, I_z), \tag{9.5}$$

$$\nu_z(I_x, I_z) = \frac{2\pi}{L} Q_z + \frac{\partial A_{0,0,0}}{\partial I_z}(I_x, I_z). \tag{9.6}$$

Thus, estimating the particle diffusion, the diffusion coefficient (9.2) must be averaged over the non-oscillating parts of the tune values inside the modulational layer. The diffusion coefficient (9.2) now becomes

$$D(I_x, I_z) = \frac{1}{4 \cdot \Delta\nu \cdot T} \cdot \left\langle \int_{-\Delta\nu}^{\Delta\nu} d\nu \int_{-T}^{T} \frac{\partial H}{\partial \phi_+}(s')ds' \times \int_{-T}^{T} \frac{\partial H}{\partial \phi_+}(s'')ds'' \right\rangle_{\phi}. \tag{9.7}$$

Furthermore, an explicit expression is necessary for the phase variables $\phi_x(s)$ and $\phi_z(s)$ in order to evaluate the integrals in Equation (9.7). Such expressions can be calculated with perturbation theory. The analysis in Section (8) showed that for the parameter values (8.1), the mode amplitudes $A_{l,m,k}$ are small in relation to the detuning term $A_{0,0,0}$ and the coupling mode $A_{2,-2,2}$. To emphasize this aspect, the mode amplitudes are written as

$$A_{l,m,k} = \varepsilon \cdot \bar{A}_{l,m,k},$$

and the action-angle variables are decomposed into zeroth and first order parts

$$I(s) = I_0(s) + \varepsilon I_1(s); \qquad \phi(s) = \phi_0(s) + \varepsilon\phi_1(s). \tag{9.8}$$

Depending on whether the modulation sidebands overlap or not, the modulation frequencies are labeled as slow or fast frequencies:

$$\vec{f}_{mod} = \vec{f}_{fast} + \vec{f}_{slow}, \tag{9.9}$$

with

$$\begin{aligned} \vec{n}_{fast} &= (n_1, n_2, ..., n_{N_1}, 0, ..., 0, 0) \\ \vec{n}_{slow} &= (0, 0, ..., 0, n_{N_1+1}, n_{N_1+2}, ..., N). \end{aligned} \tag{9.10}$$

For the following discussion three different situations are distinguished:

a) the particles are far from the coupling resonance;
b) the particles perform a rotational motion near the coupling resonance;
c) the particles are on the coupling resonance and perform a libration inside the region of regular particle motion.

a) If the particles are far from the coupling resonance, the coupling mode can be neglected and one gets for the Hamilton function

$$\begin{aligned} H &= \nu_x \cdot I_x + \nu_z \cdot I_z + A_{0,0,0}(I_x, I_z) + \\ &\varepsilon \cdot \sum_{l,m,k,\vec{n}_{fast},\vec{n}_{slow}} \left[\prod_{p=1}^{N} J_{n_{fast,p}}\left(\frac{l \cdot \Delta Q_{fast,p} \cdot f_{rev}}{f_{fast,p}}\right)\right] \cdot \left[\prod_{p=1}^{N} J_{n_{slow,p}}\left(\frac{l \cdot \Delta Q_{slow,p} \cdot f_{rev}}{f_{slow,p}}\right)\right] \times \\ &\bar{A}_{l,m,k}(I_x, I_z) \cdot \cos\left(l\phi_x + m\phi_z + \frac{2\pi}{L}\left(k + \vec{n}_{fast} \cdot \frac{\vec{f}_{fast}}{f_{rev}} + \vec{n}_{slow} \cdot \frac{\vec{f}_{slow}}{f_{rev}}\right) s + \delta_{l,k}\right), \end{aligned} \tag{9.11}$$

with

$$\begin{aligned} \dot{I}_+ &= \varepsilon \cdot \sum_{l,m,k,\vec{n}_{fast},\vec{n}_{slow}} \left[\prod_{p=1}^{N} J_{n_{fast,p}}\left(\frac{l \cdot \Delta Q_{fast,p} \cdot f_{rev}}{f_{fast,p}}\right)\right] \times \\ &(l+m) \cdot \left[\prod_{p=1}^{N} J_{n_{slow,p}}\left(\frac{l \cdot \Delta Q_{slow,p} \cdot f_{rev}}{f_{slow,p}}\right)\right] \times \\ &\bar{A}_{l,m,k}(I_x, I_z) \cdot \sin\left(l\phi_x + m\phi_x + \frac{2\pi}{L}\left(k + \vec{n}_{fast} \cdot \frac{\vec{f}_{fast}}{f_{rev}} + \vec{n}_{slow} \cdot \frac{\vec{f}_{slow}}{f_{rev}}\right) s + \delta_{l,k}\right). \end{aligned} \tag{9.12}$$

For the zeroth-order solutions of the angle variables, one gets

$$\phi_{x,0}(s) = \nu_x \cdot s + \theta_{x,0}, \qquad \phi_{z,0}(s) = \nu_z \cdot s + \theta_{z,0}. \tag{9.13}$$

The horizontal and vertical action variables vary inside the modulational layer of the seeding resonance. However, assuming that the $A_{l,m,k}$ mode amplitudes do not vary considerably *inside the modulational layer, one can neglect the variations of the action variables* and replace $A_{l,m,k}(I_x, I_z)$ by their average values inside the modulational layer. With these approximations and with the assumption

$$T \cdot \Delta\nu \gg 2\pi, \tag{9.14}$$

one can solve the integrals in (9.7) and gets for the diffusion coefficient in lowest order in ε

$$\begin{aligned} D(I_x, I_z) &= \sum_{l,m,k,\vec{n}_{fast}} \frac{(l+m)^2\pi}{2(l\Delta\nu_x + m\Delta\nu_z)} \cdot \left[\prod_{p=1}^{N} J_{n_{fast,p}}\left(\frac{l\Delta Q_{fast,p} f_{rev}}{f_{fast,p}}\right)\right]^2 \cdot A_{l,m,k}^2 \times \\ &\sum_{[\vec{n}_{slow} - \vec{n}'_{slow}] \cdot \vec{f}_{slow} = 0} \left\{\left[\prod_{p=1}^{N} J_{n_{slow,p}}\left(\frac{l \cdot \Delta Q_{slow,p} f_{rev}}{f_{slow,p}}\right)\right] \cdot \left[\prod_{p=1}^{N} J_{n'_{slow,p}}\left(\frac{l \cdot \Delta Q_{slow,p} f_{rev}}{f_{slow,p}}\right)\right]\right\}, \end{aligned} \tag{9.15}$$

where $\Delta\nu_x$ and $\Delta\nu_z$ are the layer widths in the transverse tune space, and where the sums extend over all overlapping modulation sidebands with

$$\left(\frac{m}{l}\nu_z + \frac{2\pi}{lL}\cdot\left[\vec{n}_{fast}\cdot\frac{\vec{f}_{fast}}{f_{rev}} + (\vec{n}_{slow} - \vec{n'}_{slow})\cdot\frac{\vec{f}_{slow}}{f_{rev}} + k\right]\right) \in [\nu_x - \Delta\nu,\ \nu_x + \Delta\nu]. \quad (9.16)$$

For a purely horizontal tune modulation $\Delta\nu_x$ is given by the maximum value of $\vec{n}_{slow}\cdot\frac{\vec{f}_{slow}}{f_{rev}}$ compatible with the overlap condition (5.7)

$$\Delta\nu_x = \frac{2\pi}{lL}\cdot\max_{overlap}\left(\vec{n}_{slow}\cdot\frac{\vec{f}_{slow}}{f_{rev}}\right). \quad (9.17)$$

The corresponding drift coefficient of the total action $(I_x + I_z)$ becomes

$$B(I_x, I_z) = \sum_{l,m,k,\vec{n}_{fast}} \frac{(l+m)^2\pi}{2(l\Delta\nu_x + m\Delta\nu_z)}\cdot\left[\prod_{p=1}^{N} J_{n_{fast,p}}\left(\frac{l\Delta Q_{fast,p} f_{rev}}{f_{fast,p}}\right)\right]^2 \times A_{l,m,k}\cdot\left[\frac{\partial A_{l,m,k}}{\partial I_x} + \frac{\partial A_{l,m,k}}{\partial I_z}\right] \times \sum_{\vec{n}_{slow},\vec{n'}_{slow}} \left\{\left[\prod_{p=1}^{N} J_{n_{slow,p}}\left(\frac{l\cdot\Delta Q_{slow,p} f_{rev}}{f_{slow,p}}\right)\right]\cdot\left[\prod_{p=1}^{N} J_{n'_{slow,p}}\left(\frac{l\cdot\Delta Q_{slow,p} f_{rev}}{f_{slow,p}}\right)\right]\right\}. \quad (9.18)$$

In case of only one slow modulation frequency the sum over the Bessel functions of the slow modulation frequency can be approximated by unity [58], and one gets

$$B(I_x, I_z) = \sum_{l,m,k,\vec{n}_{fast}} \frac{(l+m)^2\pi}{2(l\Delta\nu_x + m\Delta\nu_z)}\cdot\left[\prod_{p=1}^{N} J_{n_{fast,p}}\left(\frac{l\Delta Q_{fast,p} f_{rev}}{f_{fast,p}}\right)\right]^2 \times A_{l,m,k}\cdot\left[\frac{\partial A_{l,m,k}}{\partial I_x} + \frac{\partial A_{l,m,k}}{\partial I_z}\right]. \quad (9.19)$$

In the case of more than one slow modulation frequency, one can evaluate Equation (9.18) by replacing the Bessel functions of the slow modulation frequencies in (9.18) by the asymptotic formula [58]

$$J_n(\lambda) \approx \sqrt{\frac{2}{\pi\lambda}}\cdot\sin\left[\lambda - \frac{\pi}{2}n + \frac{\pi}{4}\right], \quad \lambda \gg 1, \quad |n| \le \lambda. \quad (9.20)$$

In the case of a purely horizontal sum resonance ($m = 0$) and only one slow modulation frequency one can easily calculate the tune width $\Delta\nu_x$. Because the Bessel functions of the slow tune modulation only have significant values for $(n_p < l\Delta Q_{slow} f_{rev}/f_{slow})$, the number of modulation sidebands inside the layer is approximately

$$N = 2\cdot\frac{l\Delta Q_{slow} f_{rev}}{f_{slow}}, \quad (9.21)$$

and one gets for $\Delta\nu_x$

$$\Delta\nu_x = \frac{2\pi}{L}\cdot\Delta Q_{slow}. \quad (9.22)$$

In this case the drift coefficient reduces to the simple form

$$B(I_x, I_z) = \sum_{l,k,\vec{n}_{fast}} \frac{lL}{4\Delta Q_{slow}}\cdot\left[\prod_{p=1}^{N} J_{n_{fast,p}}\left(\frac{l\Delta Q_{fast,p} f_{rev}}{f_{fast,p}}\right)\right]^2 \times A_{l,0,k}\cdot\left[\frac{\partial A_{l,0,k}}{\partial I_x} + \frac{\partial A_{l,0,k}}{\partial I_z}\right], \quad (9.23)$$

which agrees with the results in [97] and [98].

It is interesting to note that in the case of a rotational motion away from the coupling resonance, the drift and diffusion coefficients are proportional to the inverse of the slow modulation strengths. If the particles are not inside the modulational layer, or if the width of the modulational layer becomes too small for the approximation (9.14) to be valid, the drift and diffusion coefficients vanish.

b) If the particles perform a rotational motion near the coupling resonance, the coupling mode in the Hamilton function may not be neglected. Because of the oscillations of the horizontal and vertical actions near the coupling resonance, the mode amplitudes $A_{l,m,k}$, their derivatives, and the beam-beam detuning term oscillate with the frequency ω_{rot} (8.33). The left-hand side of Fig.9.1 shows an example for one period of the horizontal and vertical action oscillations for the rotational motion and the right-hand side of Fig.9.1 shows the resulting changes in the mode amplitude $A_{10,0,-313}$ and its derivatives with respect to the horizontal and vertical actions. In both pictures the total action is $I_+ = 4.4\cdot10^{-9}m$. Defining

$$\Omega_{rot} = \frac{L\cdot\omega_{rot}}{2\pi} \quad (9.24)$$

and replacing the mode amplitudes by their Fourier expansions

$$A_{l,m,k} = \frac{a_{(l,m,k),0}}{2} + \sum_{u=1}^{\infty}\left[a_{(l,m,k),u}\cdot\cos\left(\frac{2\pi}{L}u\Omega_{rot}s\right) + b_{(l,m,k),u}\cdot\sin\left(\frac{2\pi}{L}u\Omega_{rot}s\right)\right] \quad (9.25)$$

one can proceed as in case a) and gets for the diffusion coefficient

$$D(I_x, I_z) = \sum_{(l,m,k,\vec{n}_{fast})} \frac{(l+m)^2\pi}{8(l\Delta\nu_x + m\Delta\nu_z)}\cdot\left[\prod_{p=1}^{N} J_{n_{fast,p}}\left(\frac{l\Delta Q_{fast,p} f_{rev}}{f_{fast,p}}\right)\right]^2 \times \sum_{u,u'=-\infty}^{+\infty}\left[\hat{b}_{(l,m,k),u}\cdot\hat{b}_{(l,m,k),u'} + \hat{a}_{(l,m,k),u}\cdot\hat{a}_{(l,m,k),u'}\right] \times \sum_{\vec{n}_{slow},\vec{n'}_{slow}}\left\{\left[\prod_{p=1}^{N} J_{n_{slow,p}}\left(\frac{l\cdot\Delta Q_{slow,p} f_{rev}}{f_{slow,p}}\right)\right]\cdot\left[\prod_{p=1}^{N} J_{n'_{slow,p}}\left(\frac{l\cdot\Delta Q_{slow,p} f_{rev}}{f_{slow,p}}\right)\right]\right\}, \quad (9.26)$$

with

$$\hat{a}_{(l,m,k),u} = a_{(l,m,k),u} = \hat{a}_{(l,m,k),-u}, \qquad \hat{b}_{(l,m,k),u} = b_{(l,m,k),u} = -\hat{b}_{(l,m,k),-u}, \quad (9.27)$$

and where the sums extend now over all overlapping modulation sidebands with

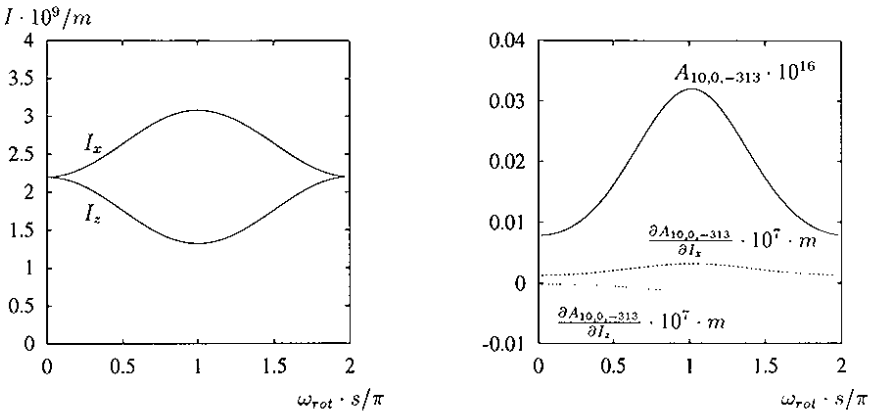

Figure 9.1:
The action oscillations for rotational motion near the coupling resonance for $I_+ = 4.4 \cdot 10^{-9} m$.
Left: The oscillations of the horizontal and vertical actions.
Right: The resulting change in the mode amplitude $A_{10,0,-313}$ *and its derivatives with respect to the horizontal and vertical actions.*

$$\left(\frac{m}{l}\nu_z + \frac{2\pi}{lL}\cdot\left[\vec{n}_{fast}\cdot\frac{\vec{f}_{fast}}{f_{rev}} + (\vec{n}_{slow}-\vec{n}'_{slow})\cdot\frac{\vec{f}_{slow}}{f_{rev}} + (u-u')\cdot\Omega_{coup} + k\right]\right) \in \tag{9.28}$$

$$[\nu_x - \Delta\nu,\ \nu_x + \Delta\nu].$$

In the case of only one slow modulation frequency, the sum over the Bessel functions of the slow modulation frequencies can be again approximated by unity. If one assumes further

$$\Delta\nu < \frac{2\pi}{L}\cdot\Omega_{coup.}, \tag{9.29}$$

one gets for the corresponding drift coefficient

$$B(I_x,I_z) = \sum_{(l,m,k)} \frac{(l+m)^2\pi}{8(l\Delta\nu_x + m\Delta\nu_z)}\cdot\left[\prod_{p=1}^{N} J_{n_{fast,p}}\left(\frac{l\Delta Q_{fast,p} f_{rev}}{f_{fast,p}}\right)\right]^2 \times \tag{9.30}$$

$$\sum_{u=-\infty}^{+\infty}\left[b_{(l,m,k),u}\cdot\left(\frac{\partial b_{(l,m,k),u}}{\partial I_x} + \frac{\partial b_{(l,m,k),u}}{\partial I_z}\right) + a_{(l,m,k),u}\cdot\left(\frac{\partial a_{(l,m,k),u}}{\partial I_x} + \frac{\partial a_{(l,m,k),u}}{\partial I_z}\right)\right].$$

In the limit of vanishing ΔI_- oscillation amplitudes, only the $u = 0$ Fourier mode is non-zero, and the drift and diffusion coefficients agree with (9.15), (9.18), and (9.19). However, for non-vanishing oscillation amplitudes, Fourier modes with $u \neq 0$ contribute to the drift coefficient. Depending on the initial phase space conditions, the additional contributions due

to the ΔI_- oscillation can lead to a drift coefficient that is larger than the one for a particle motion away from the coupling resonance. For example, for the ΔI_- oscillation in Fig.9.1, the drift coefficient is approximately four times larger than the one in the case of no action oscillations. Therefore, the coupling resonance can have a destabilizing effect on the particle motion.

c) If the particles are on the coupling resonance, its effect can be either stabilizing or destabilizing, depending on whether the particles are within a region of regular or irregular particle motion. If the particles are inside the region of regular motion around the stable fixed points of the coupling resonance, the trapping condition (5.8) is fulfilled, and the slow tune modulation can not lead to a homogeneous modulational layer. Consequently, the particle motion has no stochastic character, and one expects vanishing drift and diffusion coefficients. If, on the other hand, the resonance area of the coupling resonance contains no regions of regular particle motion, the trapping condition is not fulfilled and one can apply Equations (9.15) and (9.18).

The tracking data in Section (10) will supply an example of each case.

9.2 Randomly Varying Tune Modulation Amplitudes

Because the modulation amplitudes of the slow frequency components in the ground motion might change over time, this aspect in the estimates for the diffusion and drift coefficients must be taken into consideration. However, the stochastic properties of the tune modulation can generally not be chosen such that the resulting Focker Planck Equation is solvable. Therefore, a different approach is considered here. For explicitly random tune amplitude variations the equations of motion become

$$\dot{\phi}_+ = l\cdot(\nu_x + a\cdot\xi) + m\cdot\nu_z \tag{9.31}$$

$$\dot{I}_+ = \varepsilon\cdot(l+m)\sum_{l,m,k,\vec{n}_{slow}} \bar{A}_{l,m,k,\vec{n}_{fast},\vec{n}_{slow}}(I_x,I_z)\times \tag{9.32}$$

$$\sin\left(l\phi_x + m\phi_x + \frac{2\pi}{L}\left(k + \vec{n}_{fast}\cdot\vec{\Omega}_{fast} + \vec{n}_{slow}\cdot\vec{\Omega}_{slow}\right)s + \delta_{l,k}\right),$$

where the coupling mode has been neglected from the equations of motion, and where ξ is a random function. Assuming that ξ changes its value every τ meter, with $\xi \in [-1,1]$, $<\xi>=0$, and $T \leq \tau$, one can proceed as in Section (9.1) with $\Delta\nu_x = a$. For the particle motion far from the coupling resonance one gets for the drift and diffusion coefficients

$$D(I_x,I_z) = \sum_{l,m,k}\frac{(l+m)^2\pi}{2la}\cdot\left[\prod_{p=1}^{N} J_{n_{fast,p}}\left(\frac{l\Delta Q_{fast,p}}{\Omega_{fast,p}}\right)\right]^2\cdot A^2_{l,m,k}, \tag{9.33}$$

$$B(I_x,I_z) = \sum_{l,m,k}\frac{(l+m)^2\pi}{2la}\cdot\left[\prod_{p=1}^{N} J_{n_{fast,p}}\left(\frac{l\Delta Q_{fast,p}}{\Omega_{fast,p}}\right)\right]^2\cdot A_{l,m,k}\cdot\left[\frac{\partial A_{l,m,k}}{\partial I_x} + \frac{\partial A_{l,m,k}}{\partial I_z}\right]. \tag{9.34}$$

The coefficients do not depend on the correlation time τ and are identical with the coefficients for a purely harmonic tune modulation. Hence, one expects the same diffusion and drift coefficients for an explicitly stochastic tune modulation as in the case of a harmonic tune modulation with the same net rms modulation depth. Furthermore, for explicitly randomly

varying modulation amplitudes, it is not necessary for the modulation sidebands to form a modulational layer and the emittance growth occurs as long as the modulation amplitudes change randomly. However, in the limit of vanishing correlation times ($\tau \to 0$) or vanishing modulation depths a, the assumption (9.14) is not valid and one can not use the results (9.33) and (9.34).

9.3 The Stochastic Pump Diffusion

This section summarizes the main features of the stochastic pump diffusion as it was developed by Chirikov [36] and as it is described by Lichtenberg and Liebermann [13]. The presented work summarizes the work in [60]. The pump diffusion is based on the division of the original three-degree-of-freedom system into two systems which are successively solved.

$$H\left(I_x, I_z, \phi_x, \phi_z, s\right) = H_{driving}\left(I_x, \phi_x, s\right) + H_{coupling}\left(I_x, I_z, \phi_x, \phi_z, s\right). \tag{9.35}$$

The driving term generates the chaotic motion and the coupling term couples the chaotic motion to the remaining degree of freedom. For the sake of simplicity, the following analysis assumes a purely horizontal single resonance Hamiltonian with tune modulation for the driving term ($A_{r,0,h}$) and a single resonance Hamiltonian for the coupling term ($A_{l,m,k}$). While the pump diffusion has no significant effect on the growth rates of the total action I_+, it can have a significant effect on the action diffusion from the horizontal to the vertical plane [60].

In case of tune modulation, the separatrix of the driving primary resonance is surrounded by a stochastic layer. Inside this stochastic layer, the particle motion is chaotic and the phase variable randomizes over every half period of the oscillation around the stable fixed point [36][13]. Using Hamilton's equations

$$\frac{dI_z}{ds} = -\frac{\partial H_{coupling}}{\partial \phi_z}; \qquad \frac{d\phi_z}{ds} = \frac{\partial H_{coupling}}{\partial I_z}, \tag{9.36}$$

one can calculate a diffusion coefficient for the vertical action variable

$$D\left(I_x, I_z\right) = \frac{< \triangle I_z^2 >}{2T}, \tag{9.37}$$

where T is the half period of the motion in the stochastic layer of the horizontal driving resonance and where the average is taken over the phase variables. One gets for the change in the vertical action variable over one half period of the motion inside the stochastic layer

$$\triangle I_z = m A_{l,m,k}\left(I_x, I_z\right) \int_{s_0 - \frac{T_x}{2}}^{s_0 + \frac{T_x}{2}} \sin\left(l\phi_x(s) + m\phi_z(s) + \frac{2\pi k}{L}s + \delta_{l,m,k}\right) ds. \tag{9.38}$$

In order to solve the integral in (9.38), one can approximate the motion in the stochastic layer around the separatrix by the unperturbed motion on the pendulum separatrix

$$\phi_{x,sep}(s) = 4 \cdot \arctan\left[e^{\omega_0 \cdot s}\right] - \pi, \tag{9.39}$$

and set the integration limits to plus and minus infinity. ω_0 is the free island oscillation frequency of the horizontal driving resonance This is the central approximation in the calculation of the stochastic pump diffusion. Furthermore, one can approximate the solution of the vertical angle variable in (9.38) by the linear solution

$$\phi_z(s) = \nu_z \cdot s + \phi_0.$$

With these approximations, the integral (9.38) is improper, i.e., no limit formally exists. However, the integral is the sum of a rapidly oscillating part and a 'jump' [13]. The oscillating part leads only to a bounded oscillation in I_z and does not contribute to the diffusion. The jump can be expressed by the Melnikov-Arnold integral [36][13] (see Appendix B)

$$\mathcal{A}_{\varpi}\left(\lambda_{MA}\right) = \int_{-\infty}^{+\infty} \exp\left[i\left(\frac{\varpi}{2} \cdot \phi_{x,sep} - \lambda_{MA} \cdot \tau\right)\right] d\tau. \tag{9.40}$$

On the separatrix of the driving resonance $(r, 0, h)$ one has

$$\phi_x(s) = \left(\phi_{x,sep}(s) - h \cdot \frac{2\pi}{L}s\right)/r,$$

and gets for the change in the vertical action

$$\triangle I_z = 2m \cdot \sin\left(m\phi_0\right) \cdot A_{l,m,k}\left(I_x, I_z\right) \cdot \mathcal{A}_{\frac{2l}{r}}\left(\lambda_{MA}\right), \tag{9.41}$$

with

$$\lambda_{MA} = -\frac{2\pi}{L} \cdot \frac{\left(mQ_z + k - \frac{lh}{r}\right)}{\omega_0}, \tag{9.42}$$

where ω_0 is the free island oscillation frequency of the driving resonance.

The only quantity left in the calculation of the diffusion coefficient is the mean half period of the motion inside the stochastic layer. For a true pendulum the half period of a trajectory close to the separatrix is [36][13]

$$T = \frac{1}{\omega_0} \ln\left|\frac{32}{w}\right|,$$

where w is the relative energy deviation of the pendulum from the separatrix energy. Chirikov has shown that the average half period inside the stochastic layer may be computed by integrating the half period over the energy range of the stochastic layer, obtaining

$$\bar{T} = \frac{1}{\omega_0} \ln\left|\frac{32e}{w_s}\right|, \tag{9.43}$$

where w_s is the relative energy deviation at the edge of the stochastic layer. The stochastic layer width has been estimated in Section (5.2) and can be calculated with Equation (5.23).

In comparison with the modulation diffusion, the effect of the stochastic pump diffusion is negligible for the parameter values (8.1) and will be neglected in the following analysis. However, in contrast to the modulational diffusion, which occurs only for sufficiently wide modulational layers, the stochastic pump diffusion describes a generic diffusion that occurs for arbitrarily small stochastic layers.

9.4 RF-Noise in the Electron Cavities

Another source for the emittance growth in the proton beam comes from coherent oscillations of the electron beam. Due to a non vanishing dispersion in the electron cavities, noise in the rf-field excites coherent transverse oscillations of the electron bunch. In the interaction regions these coherent oscillations influence the proton dynamics and can cause a transverse emittance growth in the proton beam [99]. A detailed description of the process is given in [99]. Generalizing the results in [99] to include the case of one modulation frequency in the proton tunes, one gets for the average increase in the horizontal action variable

$$\begin{aligned}\Delta I_x &= \frac{x_{e,rms}^2 \cdot \delta_x \cdot I^4}{16\pi^2 Q_{p,x}^2 \beta_x^*} \cdot \Delta T \times \\ &\sum_{j=-1,1} \sum_{l,m,k,n,r} \left[J_n\left(\frac{l\Delta Q_x f_{rev}}{f_{p,mod}}\right) \cdot J_r\left(\frac{m\Delta Q_z f_{rev}}{f_{p,mod}}\right)\right]^2 \times \\ &\frac{|a_{l,m,k}|^2}{\delta_x^2 + 4\pi^2\left((l+j)Q_{p,x} + mQ_{p,z} + nf_{p,mod}/f_{rev} + k + rf_{p,mod}/f_{rev} - Q_{e,x}\right)^2},\end{aligned} \tag{9.44}$$

where $x_{e,rms}$ is the rms amplitude of the coherent horizontal electron oscillation, $Q_{e,x}$ is the horizontal electron Q-value, ΔT is the time period in number of turns, δ_x is the transverse damping constant for the electron beam in number of turns, $Q_{p,x}$ and $Q_{p,z}$ are the horizontal and vertical proton Q-values, f_{mod} and ΔQ are the modulation frequency and depth in the proton beam respectively, f_{rev} is the revolution frequency for the proton beam, and $a_{l,m,k}$ are the Fourier coefficients of the partial derivative of the horizontal beam-beam force for the protons with respect to the horizontal beam offset at the interaction region.

In [99] R. Brinkmann estimated the rms amplitude of the collective electron oscillations to

$$x_{e,rms} \sim 2\mu m. \tag{9.45}$$

The collective vertical electron oscillations are smaller than the horizontal oscillations by approximately two orders of magnitude due to a vanishing vertical dispersion in the electron cavities. Table (9.46) lists typical values for the parameters in (9.44):

Diffusion Parameters		
$x_{e,rms} = 2\mu m$	$Q_{e,x} = 47.19$	$\delta_x = 1/330$
$Q_{p,x} = 31.288$	$Q_{p,z} = 32.294$	$f_{rev} = 47.3KHz$

(9.46)

There are three important aspects regarding the growth rate (9.44). First, the growth rate increases for large rms oscillations of the electron bunch and can reach significant values for amplitudes larger than $2\mu m$. Second, like the modulational diffusion, the growth rate increases for large proton betatron oscillation amplitudes and the growth rates can reach large values for protons in the beam halo. Third, the resonance condition in (9.44) differs from that of the modulational diffusion and leads to additional resonance lines in the transverse Q-diagram.

9.5 Intra-Beam Scattering

As the particles of a bunched beam perform synchrotron oscillations, they interact with all the other particles of the same bunch. The multiple Coulomb scattering process between particles of the same bunch is called intra-beam scattering [100][101] and leads to a significant emittance growth in the longitudinal and the transverse phase space. For the proton beam in HERA the effect has been estimated in [102]. For a proton energy of $820GeV$ and the design current in the proton bunch the horizontal emittance growth rate is

$$\begin{aligned}\frac{<\Delta I_x>}{\Delta t} &\approx 1.0 \cdot 10^{-7} mm \cdot mrad/sec \\ &= 2.0 \cdot 10^{-18} m/Turn.\end{aligned} \tag{9.47}$$

The emittance growth of a single particle is independent of the beam-beam interaction and only proportional to the effective proton density in the bunch. For a Gaussian particle distribution the drift coefficient for the horizontal action can be written as [53]

$$\begin{aligned}\frac{\Delta I_x}{\Delta t}(I_x, I_z) &= 1.9 \cdot 10^{-7} \cdot \frac{1}{(2\pi)^2} \cdot \int_0^{2\pi} \exp\left(-\frac{4 \cdot I_x}{\epsilon_x} \cdot \cos^2(\phi_x)\right) d\phi_x \times \\ &\int_0^{2\pi} \exp\left(-\frac{4 \cdot I_z}{\epsilon_z} \cdot \cos^2(\phi_z)\right) d\phi_z \cdot mm \cdot mrad \cdot sec^{-1},\end{aligned} \tag{9.48}$$

where ϵ_x and ϵ_z are the horizontal and vertical two-sigma beam emittances. There are two important aspects for the emittance growth due to intra-beam scattering. First, in contrast to the emittance growth due to the non-linear aspects of the particle motion, the growth due to intra-beam scattering is independent of the beam-beam interaction and should not increase for luminosity operations. Therefore, the intra-beam scattering can not account for the increase of the particle diffusion during luminosity operation. Second, the drift coefficient attains its maximum value at the beam core, which is also qualitatively different from the modulational diffusion in the previous section, were the drift coefficient increased towards the beam halo. Hence, while the modulational diffusion dominates the emittance growth at distances larger than one sigma of the proton beam, the intra-beam scattering process is the dominant cause for emittance growth in the beam core. Section (11) will compare the different analytical estimates for the emittance growth with the particle diffusion in the proton beam of HERA.

Section 10

Numerical Evaluation of the Drift Coefficients

Before the analytical estimates are compared with tracking data, a brief summary of the procedures for the analytical and numerical evaluation of the drift coefficients is given.

First, a description of the procedure for the analytical estimate is given. In order to evaluate the amplitudes for the horizontal and vertical action oscillations during the rotational motion, one particle with the initial conditions $I_x = I_+/2 = I_z$, $\phi_x \in [-\pi, \pi]$, and $\phi_z = 0$ is tracked over 10^4 turns through the model structure. The tracking is done by a successive application of the map (3.18) to the particle coordinates. The oscillation frequency ω_{rot} can be calculated from the linear tunes and must agree with the value obtained from the particle tracking. Once the amplitude ΔI_- and the oscillation frequency ω_{rot} are known, they are inserted into the beam-beam potential (3.6) and the Fourier coefficients of the potential are calculated with an FFT. Knowing the Fourier coefficients of the mode amplitudes (9.25), one can use (9.19) or (9.30) for the calculation of the drift coefficient.

For the numerical evaluation of the drift coefficients, the time evolution of a Gaussian particle distribution is calculated by a successive application of the map (3.18) to the particle coordinates. The mean total action can be calculated from the single particle actions by

$$< I_+ >:= \sum_{n=1}^{M} \frac{(I_{x,n} + I_{z,n})}{M}, \tag{10.1}$$

where the summation extends over all particles. (The total emittance is approximately twice the total action.) In order to get reliable numbers for the drift coefficients, one must follow the particles at least over 10^6 turns. Due to the large number of particles and turns required for reliable tracking results, the numerical evaluation of the drift coefficients is extremely time consuming. (One point in the Q-diagram needs approximately 1,200 cpu-minutes on an HP 9000-730.)

The comparison of the analytical estimates and the numerical tracking data is done for two different distributions in the action variables. First, a narrow Gaussian distribution for the horizontal and vertical actions with

$$< I_y >= \frac{I_+}{2}, \quad \sigma_{I_y} = 2.5 \cdot 10^{-10} m, \quad y = x, z, \tag{10.2}$$

and with a uniform distribution of the angle variables

$$\phi_y \in [-\pi, \pi], \quad y = x, z \tag{10.3}$$

is considered. The narrow spread in the action variables was chosen for three reasons. First, the narrow action spread assures that the Fourier mode amplitudes $A_{l,m,k}$ do not vary much over the particle distribution. Second, the more particles are actually inside the region of irregular particle motion, the larger the calculated drift coefficients will be. Hence, in order to observe the emittance growth in the distribution, one has to ensure that a large fraction of the particle distribution lies inside the regions of irregular particle motion. For a narrow particle distribution the initial conditions can be chosen such that more than 60% of the particles lie within regions of irregular particle motion. A third reason for a narrow particle distribution is that it allows to clearly separate the contributions of different resonance sidebands. All three aspects form the prerequisite for an accurate comparison of the analytical estimates with the tracking data. The only prerequisite for choosing such a narrow particle distribution is a good understanding of the resonance structure and the ability to estimate the resonance positions to a high accuracy. The results in Section (8) demonstrated that such an accurate analysis of the resonance structure is cumbersome, but possible.

However, once the validity of the diffusion model is confirmed by the tracking data of a narrow particle distribution, its relevance for a wide particle distribution must still be demonstrated. Using the knowledge of the diffusion mechanism for an appropriate choice of the modulation parameters, a wide distribution of 9,000 particles with

$$< I_y >= \frac{I_+}{2}, \quad \sigma_{I_y} = 7.0 \cdot 10^{-9} m, \quad y = x, z \tag{10.4}$$

is considered in a second step. As the numerical simulation of such a large particle distribution is very time consuming, only a few examples of the tracking results will be given for such a large distribution.

10.1 Narrow Particle Distributions

The left-hand side of Fig.10.1 shows the particle distribution in the transverse action space for horizontal and vertical Q-values away from the coupling resonance, and the right-hand side shows the distribution for Q-values close to the coupling resonance. Both pictures show the particle distribution after 500 turns. An initial filamentation of the particle distribution due to the motion on the coupling resonance occurs close to the coupling resonance during the first 500 turns. However, this filamentation only leads to an increase of I_-, and not to an increase in the total action I_+. The initial conditions are chosen such that approximately 60% of the particles are on the $1200Hz$ modulation sideband of the purely horizontal 10^{th} order sum resonance. This choice of initial conditions yields approximately the same number of particles inside the modulational layer for all vertical Q-values, and thus simplifies the comparison of the drift coefficients for different vertical Q-values. The solid lines in Fig.10.1 show the upper and lower bounds of the modulational layer due to a slow tune modulation with $0.6Hz$ and $\Delta Q_{slow} = 6.25 \cdot 10^{-5}$ and for a horizontal linear Q-value

$$Q_x = 31.297. \tag{10.5}$$

For both cases, approximately half the particles are inside the modulational layer. (Without the fast tune modulation, the particles experience no low-order sum resonance, and the diffusion process stops altogether.) As the vertical linear Q-value is varied from $Q_z = 32.296$ to

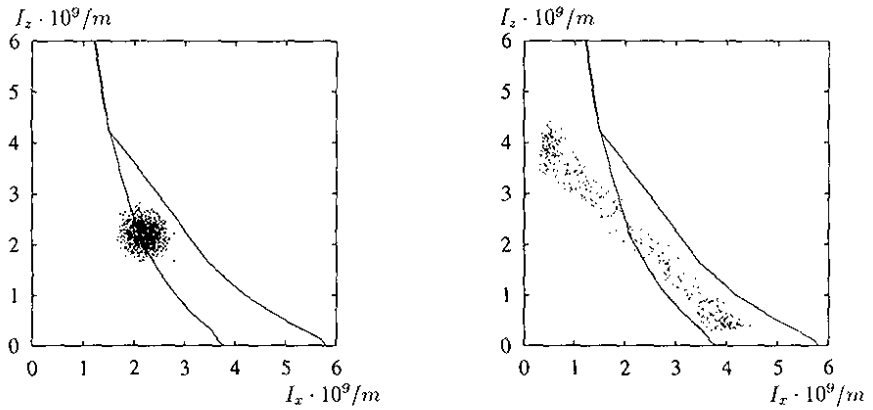

Figure 10.1:
Left: The initial particle distribution in the transverse action space after 500 *turns.*
Right: The same particle distribution for a motion on the coupling resonance. Because of the modulation due to the coupling resonance, the particle distribution is subject to an initial spread. In both cases, the external tune modulation was turned off.

$Q_z = 32.297$, the particles approach the coupling resonance. Because of the increase in the action oscillations near the coupling resonance, the drift coefficient increases as the distance from the coupling resonance decreases. As the sum resonances start to overlap on the coupling resonance, the contributions of the overlapping resonances add up and lead to a large increase in the drift coefficient (9.30). If the particle motion takes place inside the region of regular motion around the stable fixed points of the coupling resonance, the homogeneous modulational layer of the slow tune modulation vanishes and the particle motion has no stochastic character. Consequently, the drift coefficient should vanish in that case. For each set of modulation frequencies, the vertical linear Q-value is sampled over

$$Q_z \in [32.2962,\ 32,2982]. \tag{10.6}$$

In the following, four qualitatively different situations will be analyzed:

a) one fast and one slow modulation frequency:
($f_{fast,1} = 1200Hz, f_{slow} = 0.6Hz$);
b) two fast and one slow modulation frequency:
($f_{fast,1} = 1200Hz, f_{fast,2} = 50Hz, f_{slow} = 0.6Hz$);
c) two fast, one slow, and one intermediate modulation frequency:
($f_{fast,1} = 1200Hz, f_{fast,2} = 50Hz, f_{slow} = 0.6Hz, f_{int.} = 14.0Hz$);
d) a randomly varying modulation amplitude in the slow frequency spectrum.

a) The discussion starts with one slow and one fast modulation frequency with

$f_{fast} = 1200Hz$	$\Delta Q_{fast} = 3.13 \cdot 10^{-4}$
$f_{slow} = 0.6Hz$	$\Delta Q_{fast} = 6.25 \cdot 10^{-5}$.

The fast tune modulation might occur in the natural ripple spectrum of the HERA-p power supplies, and the slow tune modulation has the same order of magnitude as the tune modulation caused by the ground motion in the HERA tunnel [88]. Fig.10.2 shows the corresponding drift coefficients versus the vertical Q-value. The solid line in Fig.10.2 shows the analytically calculated drift coefficient for a contribution of the purely horizontal $(10, 0, -313)$ sum resonance alone, and the dashed line shows the analytically calculated drift coefficient for a contribution of all 10^{th} order sum resonances. In the latter, a symmetrical distribution of the sum resonances around the coupling resonance was assumed. For $32.2969 < Q_z < 32.2973$, the particles are inside the region of regular motion around the stable fixed points of the coupling resonance, and the drift coefficients vanish. The squares in Fig.10.2 show the drift coefficients obtained by the numerical tracking. Far from the coupling resonance, the numerical data agree nicely with the analytical estimates and yield an average drift coefficient of

$$B \approx 0.05 \cdot 10^{-16} m/Turn. \tag{10.7}$$

As the vertical Q-values approach the coupling resonance ($Q_z = (Q_x + 1) = 32.297$), the drift coefficient increases. The solid line in Fig.10.2 shows an increase of the drift coefficient by a factor of two due to the action oscillations close to the coupling resonance. For $32.296 < Q_z < 32.298$, the numerical data show an increase of the drift coefficient larger than the one predicted by the horizontal $(10, 0, -313)$ sum resonance alone, indicating an additional contribution of the $(8, 2, -315)$, $(6, 4, -317)$, $(4, 6, -319)$, and $(2, 8, -321)$ sum resonances. The dashed line in Fig.10.2 shows the analytically calculated drift coefficient for a consideration of all 10^{th} order sum resonances. For vertical Q-values smaller than 32.297, the measured data are slightly lower than the analytical estimate (dashed line), indicating an asymmetric distribution of the sum resonances around the coupling resonance. Neglecting the regular motion on the coupling resonance, one can calculate an upper estimate for the drift coefficient. Using Equation (9.30), one obtains

$$B_{max} \approx 1.0 \cdot 10^{-16} m/Turn.$$

The drift coefficient increases considerably if a stronger $1200Hz$ modulation is considered. For example, for

$f_{fast} = 1200Hz$	$\Delta Q_{fast} = 1.25 \cdot 10^{-3}$
$f_{slow} = 0.6Hz$	$\Delta Q_{fast} = 6.25 \cdot 10^{-5}$.

the Bessel functions of the $1200Hz$ modulation in (9.30) become larger, and the analytical estimate predicts an increase of the drift coefficients by a factor 16. Fig.10.3 shows the corresponding values for the analytically and numerically calculated drift coefficients. The solid line shows again the analytically calculated drift coefficient for a contribution of the purely horizontal $(10, 0, -313)$ sum resonance alone, the dashed line the drift coefficient for a contribution of all 10^{th} order sum resonances, and the squares the numerically calculated drift coefficients. Again, the numerical data show an increase of the drift coefficient close to the coupling resonance and a vanishing drift coefficient directly on the coupling resonance. As

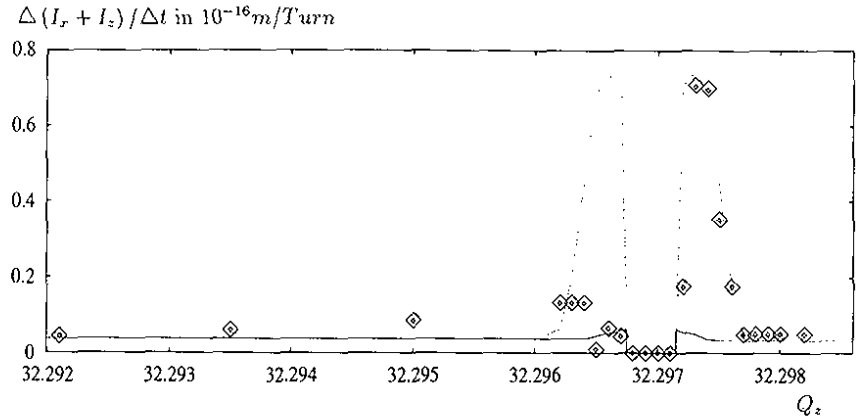

Figure 10.2: *The drift coefficient versus the vertical Q-value for* $Q_x = 31.2971$ *and a harmonic tune modulation with two frequencies:*
$f_1 = 1200Hz, \Delta Q_{1200Hz} = 1.3 \cdot 10^{-4}$ *and* $f_2 = 0.6Hz, \Delta Q_{0.6Hz} = 6.25 \cdot 10^{-5}$. *The solid line shows the analytical estimates for a contribution of the purely horizontal* $(10, 0, -313)$ *sum resonance alone, the dashed line the drift coefficient for a contribution of all* 10^{th} *order sum resonances and the squares show the numerically calculated drift coefficients.*

expected from Equation (9.30), the average drift coefficient away from the coupling resonance is about one order of magnitude larger than the drift coefficient for $\Delta Q_{1200Hz} = 3.13 \cdot 10^{-4}$

$$B \approx 0.8 \cdot 10^{-16} m/Turn. \tag{10.8}$$

For both $1200Hz$ modulation depths, the coupling mode has both a stabilizing as well as a destabilizing effect on the particle motion. The action oscillations outside the regions of regular motion have a destabilizing effect on the particle motion, and the oscillations inside the regions of regular motion have a stabilizing effect. Because of the regions of regular motion around the stable fixed points of the coupling resonance, the particle diffusion vanishes in both cases for $Q_z \approx (Q_x + 1)$.

b) Next, two fast and one slow modulation frequencies are considered. For a particle distribution on the $(f_1 = 1200Hz, n_1 = 1, f_2 = 50Hz, n_2 = -1)$ sideband of the $(10, 0, -313)$ sum resonance, the analysis starts with the frequencies

$f_{fast,1} = 1200Hz$	$\Delta Q_{fast,1} = 1.25 \cdot 10^{-4}$
$f_{fast,2} = 50Hz$	$\Delta Q_{fast,2} = 4.38 \cdot 10^{-4}$
$f_{slow} = 0.6Hz$	$\Delta Q_{slow} = 6.25 \cdot 10^{-5}$.

With the help of (9.30), one can calculate again upper estimates for the drift coefficients. Far from the coupling resonance, where only the sidebands of the $(10, 0, -313)$ sum resonance contribute to the particle diffusion, one gets from Equation (9.30)

$$B \approx 0.03 \cdot 10^{-16} m/Turn,$$

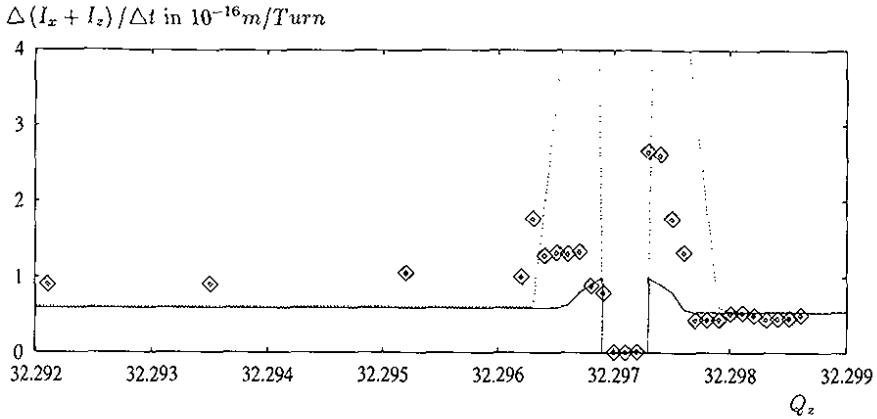

Figure 10.3: *The drift coefficient versus the vertical Q-value for* $Q_x = 31.2971$ *and a harmonic tune modulation with two frequencies:*
$f_1 = 1200Hz, \Delta Q_{1200Hz} = 1.25 \cdot 10^{-3}$ *and* $f_2 = 0.6Hz, \Delta Q_{0.6Hz} = 6.25 \cdot 10^{-5}$. *The solid line shows the analytical estimates for a contribution of the purely horizontal* $(10, 0, -313)$ *sum resonance alone, the dashed line the drift coefficient for a contribution of all* 10^{th} *order sum resonances and the squares show the numerically calculated drift coefficients.*

and close to the coupling resonance, where the contribution of all 10^{th} order sum resonances must be considered, one gets

$$B \approx 0.9 \cdot 10^{-16} m/Turn.$$

Directly on the coupling resonance, the drift coefficient should vanish again because of the regions of regular motion around the stable fixed points of the coupling resonance. For the average value of the drift coefficient for a particle motion far from the coupling resonance, the tracking data yield

$$B_{num.} \approx 5.0 \cdot 10^{-18} m/Turn,$$

and a maximum value of

$$B_{num.,max} \approx 0.5 \cdot 10^{-16} m/Turn$$

for $Q_z = 32.297$. In both cases, the numerical tracking data agree nicely with the analytical estimates in Section (9.1). As expected, the tracking data yield a vanishing drift coefficient for a particle motion on the coupling resonance.

Next, a larger modulation strength for the $1200Hz$ signal is considered:

$f_{fast,1} = 1200Hz$	$\Delta Q_{fast,1} = 1.25 \cdot 10^{-3}$
$f_{fast,2} = 50Hz$	$\Delta Q_{fast,2} = 4.38 \cdot 10^{-4}$
$f_{slow} = 0.6Hz$	$\Delta Q_{slow} = 6.25 \cdot 10^{-5}$.

(10.9)

In this case, the modulational layers of the $50Hz$ sidebands overlap, resulting in one wide modulational layer. Equations (9.19) and (9.30) predict an increase in the drift coefficients

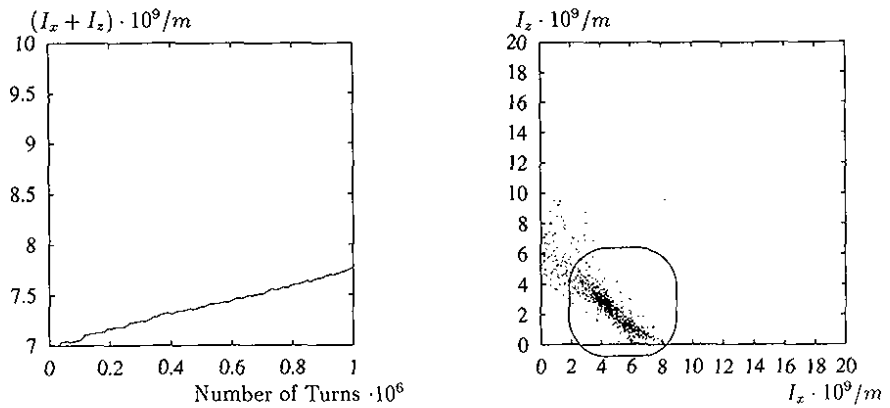

Figure 10.4:
Left: The mean total action versus the number of turns for $Q_z = 32.297$ *and a tune modulation with:*
$f_{fast,1} = 1200Hz$, $\Delta Q_{fast,1} = 1.25 \cdot 10^{-3}$, $f_{fast,2} = 50Hz$, $\Delta Q_{fast,2} = 4.38 \cdot 10^{-4}$, *and* $f_{slow} = 0.6Hz$, $\Delta Q_{slow} = 6.25 \cdot 10^{-5}$.
Right: The corresponding final particle distribution after 10^6 *turns. The oval indicates the particles inside the region of stable motion around the stable fixed points of the coupling resonance.*

by almost two orders of magnitude.

$$B \approx 5.0 \cdot 10^{-16} m/Turn$$

for a particle motion away from the coupling mode, and a maximum value of

$$B \approx 50.0 \cdot 10^{-16} m/Turn$$

for a particle motion in the direct neighbourhood of the coupling resonance. Because the size of the regions of regular motion decreases in the case of overlapping modulational layers, the region of regular motion on the coupling resonance can not contain the entire particle distribution at once. Hence, one expects the drift coefficients not to vanish for a particle motion on the coupling resonance $Q_z = (Q_x + 1)$, but to attain only a non-vanishing minimum.

The numerical data obtained by the particle tracking confirm the drastic increase of the drift coefficients and the non-vanishing drift coefficient for a particle motion on the coupling resonance. The numerical data now yield

$$B_{num.} \approx 8.0 \cdot 10^{-16} m/Turn$$

for a particle motion far from the coupling mode, and

$$B_{num.,max} \approx 25.0 \cdot 10^{-16} m/Turn$$

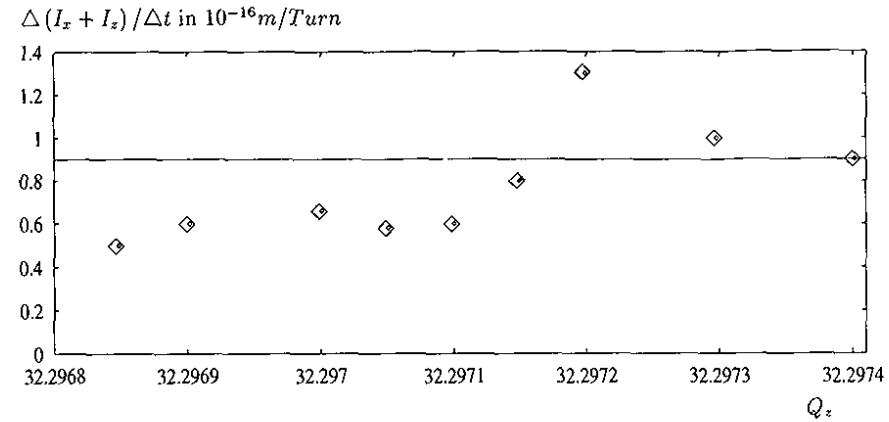

Figure 10.5: *The drift coefficient versus the vertical Q-value for* $Q_x = 31.2971$ *and a harmonic tune modulation with four frequencies:*
$f_1 = 1200Hz, \Delta Q_{1200Hz} = 1.25 \cdot 10^{-4}$, $f_2 = 50Hz, \Delta Q_{50Hz} = 4.38 \cdot 10^{-4}$,
$f_3 = 14Hz, \Delta Q_{14Hz} = 6.25 \cdot 10^{-5}$, *and* $f_{slow} = 0.6Hz, \Delta Q_{0.6Hz} = 6.25 \cdot 10^{-5}$. *The solid line shows the analytical estimate and the squares show the numerically calculated drift coefficients.*

for a particle motion close to the coupling resonance. On the coupling resonance, the tracking data yield

$$B_{num.,coup.} \approx 7.0 \cdot 10^{-16} m/Turn,$$

which is of the same order of magnitude as the drift coefficient for a particle motion away from the coupling mode. The left-hand side of Fig.10.4 shows the mean total action versus the number of turns for $Q_z = 32.297$, and the right-hand side of Fig.10.4 shows the corresponding final particle distribution after 10^6 turns. In the right-hand side of Fig.10.4, one can recognize a dark-shaded area, where the particles did not diffuse. This area corresponds to that fraction of the particle distribution which lies inside the region of regular motion around the stable fixed points of the coupling resonance.

For large $1200Hz$ modulation depths, the drift coefficients are large enough to spoil the beam lifetime. Therefore, in the case of two fast modulation frequencies, the tolerances of the power supplies must be clearly smaller than in the case of one modulation frequency only.

c) Next, a tune modulation in the intermediate frequency range ($f \in [10Hz, 50Hz]$) is included in the analysis. For a tune modulation in the intermediate frequency range, the modulation sidebands of the coupling resonance can overlap in such a way as to lead to a homogeneous modulational layer around the coupling resonance, and to an overlap of the neighbouring seeding resonances. In this case, the drift coefficient does not vanish for $(Q_z = (Q_x + 1))$, and the coupling resonance has no stabilizing effect on the particle motion. Because all 10^{th} order sum resonances contribute to the drift coefficient for $(Q_z = (Q_x + 1))$, one expects

a large drift coefficient in the direct neighbourhood of the coupling resonance. For

$f_{fast,1} = 1200Hz$	$\Delta Q_{fast,1} = 2.5 \cdot 10^{-4}$
$f_{fast,2} = 50Hz$	$\Delta Q_{fast,2} = 4.38 \cdot 10^{-4}$
$f_3 \in [10Hz, 50Hz]$	$\Delta Q_3 = 6.25 \cdot 10^{-4}$
$f_{slow} = 0.6Hz$	$\Delta Q_{slow} = 6.25 \cdot 10^{-5}$

(10.10)

the overlap condition (5.7) indicates an overlap of the sidebands around the coupling resonance for ($f_3 < 16Hz$), and the trapping condition (5.8) indicates a particle trapping for ($f_3 < 1.2Hz$). Hence, one expects a homogeneous modulational layer around the coupling resonance for an additional tune modulation with

$$1.2Hz < f_3 < 16Hz, \qquad \Delta Q_3 = 6.25 \cdot 10^{-5}.$$

In the following an additional tune modulation with

$$f_3 = 14Hz, \qquad \Delta Q_3 = 6.25 \cdot 10^{-5} \tag{10.11}$$

is considered. In this case the analytical estimate for the drift coefficient on the coupling resonance yields

$$B_{th.,max} \approx 0.9 \cdot 10^{-16} m/Turn,$$

and predicts an extremely wide modulational layer due to an overlap of all modulation sidebands. The solid line in Fig.10.5 shows the corresponding analytical estimate for the drift coefficient and the squares show again the numerically estimated drift coefficients. One clearly recognizes the non-vanishing drift coefficient around the coupling resonance and the nice correspondence of the numerical and analytical data.

d) In order to compare the drift coefficients for the explicitly random excitation with the ones for a harmonic slow tune modulation, a fast harmonic tune modulation with the same values as in case a) is considered. But this time, the slow modulation frequency is replaced by a random signal with the same net modulation depth:

$f_{fast} = 1200Hz$	$\Delta Q_{fast} = 1.25 \cdot 10^{-3}$
$a = \frac{2z}{L} \cdot \Delta Q_{rand}$	$\Delta Q_{rand} = 6.25 \cdot 10^{-5}$

In the following the correlation time τ of the random signal in Equation (9.31) is varied over three orders of magnitude from ($\tau = 10^2 \cdot L$) to ($\tau = 10^4 \cdot L$), and constant as well as stochastically varying correlation times τ are considered. The correlation time τ determines the time interval during which the detuning remains constant. As in (9.31), the modulation amplitude is assumed to change randomly every τ turns within the interval $\nu \in [\nu_x - a,\ \nu_x + a]$ and with $< \nu >= \nu_x$.

The analysis in the previous section showed that the diffusion and drift coefficients caused by an isolated sum resonance and an explicitly random tune modulation are independent of the correlation time τ and reproduce the values obtained for a diffusion due to the stochastic character of the motion inside the modulational layer of a slow harmonic tune modulation. The solid line in Fig.10.6 shows the analytical estimates of the drift coefficients for a contribution of the purely horizontal $(10, 0, -313)$ sum resonance alone and the dashed line the drift coefficient for a contribution of all 10^{th} order sum resonances. The lines are identical with the lines in Fig.10.3, where a harmonic tune modulation with the same modulation depths was

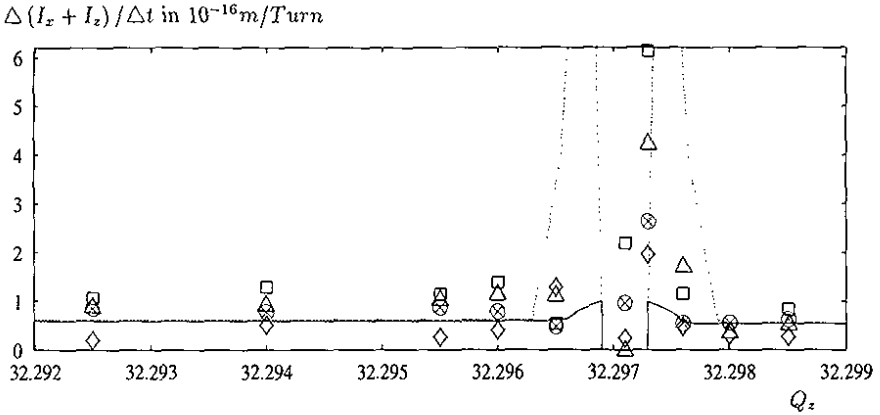

Figure 10.6: *The drift coefficient versus the vertical Q-value for $Q_x = 31.297$ and a harmonic fast tune modulation with $f_1 = 1200Hz, \Delta Q_{1200Hz} = 1.3 \cdot 10^{-3}$ and an explicitly random tune modulation with $\Delta Q_{stoch.} = 6.25 \cdot 10^{-5}$. The figure shows the numerically calculated drift coefficients for four different correlation times τ:*
$\Diamond: \tau = 10^2 \cdot L$, $\Box: \tau = 10^3 \cdot L$, $\otimes: \tau = 10^4 \cdot L$, $\triangle: \tau \in [0.2 \cdot 10^4 \cdot L,\ 1.8 \cdot 10^4 \cdot L]$.
In all cases, the same set of vertical Q-values was chosen. The solid line shows the analytical estimates for a contribution of the purely horizontal $(10, 0, -313)$ sum resonance alone, and the dashed line the drift coefficient for a contribution of all 10^{th} order sum resonances.

considered. The diamonds show the numerically estimated drift coefficient for $\tau = 10^2 \cdot L$, the squares the numerical values for $\tau = 10^3 \cdot L$, the circles the values for $\tau = 10^4 \cdot L$, and the triangles the values for a randomly changing correlation time. As expected from Equation (9.34), far from the coupling resonance, the numerical data are almost independent from the correlation time τ and agree nicely with the analytical estimates.

As in the case of a purely harmonic tune modulation, all 10^{th} order sum resonances contribute to the particle diffusion for ($Q_x - Q_z = -1$), and the drift coefficient attains its maximum value for a particle motion close to the coupling resonance. While the drift coefficient does not depend on the correlation time τ for a particle motion away from the coupling resonance, the drift coefficient for a particle motion near the coupling resonance changes with τ and Q_z. Depending on the correlation time τ, regions of regular motion around the stable fixed points of the coupling resonance can limit the particle diffusion. For $\tau = 10^2 \cdot L$ the regions of regular motion around the stable fixed points of the coupling resonance capture the particles on the coupling resonance and lead to a vanishing drift coefficient. For $\tau = 10^3 \cdot L$ the regions of regular motion disappear and the drift coefficient attains a non-vanishing value on the coupling resonance. Hence, the maximum value of the drift coefficient near the coupling resonance depends upon the correlation time τ.

Before the emittance growth in a wide particle distribution is analyzed, the dependence of the drift and diffusion coefficients on the fast modulation frequency is underlined. In all the above cases, particle diffusion is caused by a simultaneous tune modulation with fast and

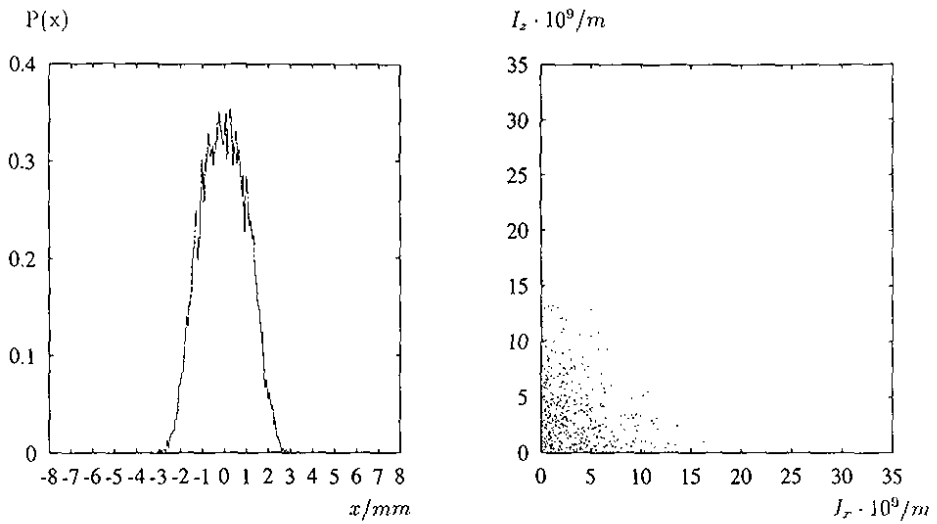

Figure 10.7:
Left: The density function $P(x)$ of the wide particle distribution for the x coordinate ($\beta_x = 191m$).
Right: The distribution of 9,000 particles in the transverse action space.

slow frequency components. Without the slow or the fast tune modulation, one does not observe any particle diffusion. Hence, assuming moderate modulation depths for the slow tune modulation one can reduce the particle diffusion by compensating the fast modulation frequencies.

10.2 Wide Particle Distributions

In order to demonstrate the relevance of the diffusion mechanism for a wide particle distribution, the time evolution of a wide particle distribution is analyzed for a simultaneous tune modulation with four harmonic frequency components. The left-hand side of Fig.10.7 shows the density function of the wide distribution (10.4) for the x variable and the right-hand side shows the distribution in the transverse action space.

In the following two different sets of modulation parameters are analyzed. First, a relatively strong tune modulation with

$f_1 = 1200Hz$	$\triangle Q_1 = 3.13 \cdot 10^{-4}$
$f_2 = 50Hz$	$\triangle Q_2 = 3.13 \cdot 10^{-4}$
$f_3 = 14Hz$	$\triangle Q_3 = 3.13 \cdot 10^{-4}$
$f_4 = 0.6Hz$	$\triangle Q_4 = 6.25 \cdot 10^{-5}$,

(10.12)

is considered. Because of the wide particle distribution, the analytical expressions from Section (10) can only yield rough estimates for the average drift coefficients in the layer. Using the expressions (9.19) and (9.30) one gets for the modulation parameters (10.12)

$$B \approx 1.0 \cdot 10^{-16} m/Turn. \tag{10.13}$$

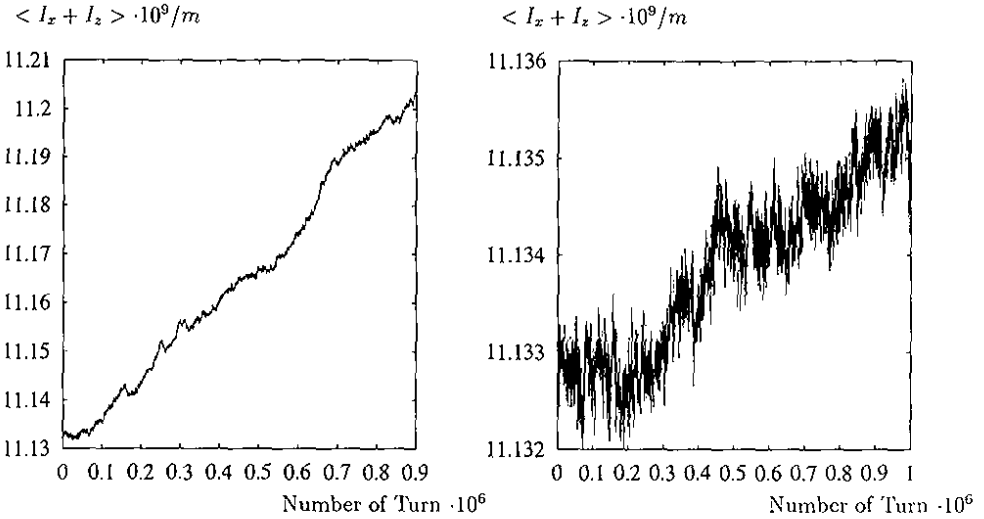

Figure 10.8:
The average action versus the number of turns.
Left: $f_1 = 1200Hz$, $\triangle Q_{1200Hz} = 3.0 \cdot 10^{-4}$, $f_2 = 50Hz$, $\triangle Q_{50Hz} = 3.0 \cdot 10^{-4}$, $f_3 = 14Hz$, $\triangle Q_{14Hz} = 3.0 \cdot 10^{-4}$, $f_4 = 0.6Hz$, $\triangle Q_{0.6Hz} = 6.25 \cdot 10^{-5}$.
Right: $f_1 = 1200Hz$, $\triangle Q_{1200Hz} = 1.0 \cdot 10^{-4}$, $f_2 = 50Hz$, $\triangle Q_{50Hz} = 1.0 \cdot 10^{-4}$, $f_3 = 14Hz$, $\triangle Q_{14Hz} = 1.0 \cdot 10^{-4}$, $f_4 = 0.6Hz$, $\triangle Q_{0.6Hz} = 6.25 \cdot 10^{-5}$.

The left-hand side of Fig.10.8 shows the resulting average action versus the number of turns. The numerical tracking data in Fig.10.8 yield for the drift coefficient

$$B_{num} \approx 0.78 \cdot 10^{-16} m/Turn, \tag{10.14}$$

and correspond nicely with the analytical estimate (10.13).

Next, a tune modulation with moderate modulation depths

$f_1 = 1200Hz$	$\triangle Q_1 = 1.0 \cdot 10^{-4}$
$f_2 = 50Hz$	$\triangle Q_2 = 1.0 \cdot 10^{-4}$
$f_3 = 14Hz$	$\triangle Q_3 = 1.0 \cdot 10^{-4}$
$f_4 = 0.6Hz$	$\triangle Q_4 = 6.25 \cdot 10^{-5}$

(10.15)

is considered. The right-hand side of Fig.10.8 shows the resulting average action versus the number of turns. From Equations (9.19) and (9.30) one expects now an average drift coefficient of the order of

$$B \approx 0.1 \cdot 10^{-16} m/Turn. \tag{10.16}$$

However, the numerically evaluated drift coefficient in Fig.10.8 yields only

$$B_{num} \approx 0.04 \cdot 10^{-16} m/Turn, \tag{10.17}$$

indicating that not all particles are subject to the diffusion process.

At the end of this Section the dependence of the drift coefficients on the fast modulation frequency is demonstrated once more. For both modulation examples, (10.12) and (10.15), the particles do not diffuse if the fast $1200Hz$ component is turned off. Even for $50Hz$ modulation amplitudes as large as $\Delta Q_{50Hz} = 1.0 \cdot 10^{-3}$, one does not observe any increase in the average action if the fast $1200Hz$ modulation is turned off. Only for $\Delta Q_{50Hz} > 1.0 \cdot 10^{-3}$ do the particles start to diffuse even without the fast modulation frequency. On the other hand, without the $50Hz$ component the particles will still diffuse as long as they are subject to the simultaneous tune modulation with $1200Hz$ and an additional slow frequency component. Hence, assuming moderate modulation depths for the slow and intermediate modulation frequencies, small modulation amplitudes for the fast frequency components are the prerequisite for a large beam lifetime in the storage ring.

Section 11

Comparison of the Analytical Estimates with the Particle Diffusion in HERA

The good agreement of the analytical estimates with the numerically evaluated drift coefficients confirms nicely the validity of the diffusion model and encourages a comparison of the analytical estimates with the measured coefficients in the proton storage ring of HERA. A comparison of the analytically and numerically estimated drift coefficients with the ones measured in the proton storage ring of HERA can be done in two ways. Either one can compare the analytical estimates for the drift coefficients with the emittance growth in HERA, or one can compare the analytical estimates for the diffusion coefficients with the fitted coefficients of a diffusion measurement at the proton collimators [103]. As the protons in HERA collide with a flat electron beam, the analytical estimates have to be derived for a beam-beam interaction with flat beams in both cases. The left-hand side of Fig.11.1 shows the resonance lines of the non-linear betatron resonances up to 10^{th} order in in the Cartesian coordinates x and z, with three typical proton Q-values during the luminosity operation in 1993. For all three working points the Q-values are clearly far from the resonance lines. The right-hand side of Fig.11.1 shows the additional resonance sidebands of a tune modulation with $600Hz$, as it is caused by ripples in the power supplies during luminosity operation (see Section 6). In the case of a fast tune modulation with $600Hz$ all working points are close to a non-linear resonance that leads to a particle diffusion. In the following, the analysis concentrates on the working point $(Q_x = 31.288, Q_z = 32.294)$.

First, the analytically estimated drift coefficients are compared to the average emittance growth in HERA. Calculating the Fourier coefficients for a beam-beam interaction with flat beams by numerical integration of (3.6) and a subsequent FFT, one can calculate analytical estimates for the diffusion and drift coefficients. Fig.11.2 shows the resulting drift coefficients

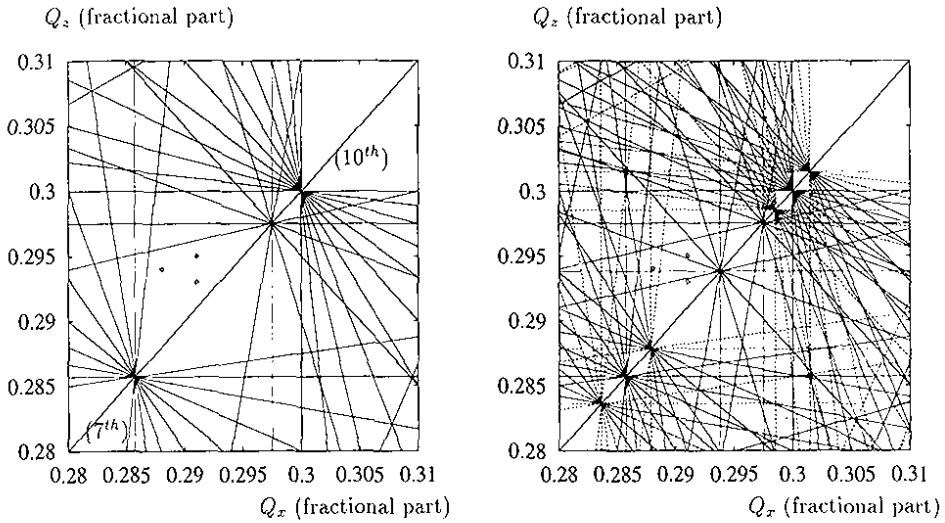

Figure 11.1:
Three typical proton working points in HERA during the 1993 luminosity runs.
Left: The resonance lines up to 10^{th} order in x and z without any tune modulation.
Right: The resonance lines and their sidebands for a fast tune modulation with $600Hz$ as caused by ripples in the power supply.

for the parameter values (11.1).

HERA Parameters	
Typical Horizontal Q-Value	$Q_x = 31.288$
Typical Vertical Q-Value	$Q_y = 32.294$
Number of Electrons per Bunch	$N_e = 3.7 \cdot 10^{10}$
Horizontal Electron Beam Size	$\sigma_{e,x} = 0.27mm$
Vertical Electron Beam Size	$\sigma_{e,y} = 0.03mm$
Horizontal Beam-Beam Detuning	$\xi_{p,x} = 0.0013$
Vertical Beam-Beam Detuning	$\xi_{p,z} = 0.0012$
β_x^* at the Interaction Points	$10.0m$
β_z^* at the Interaction Points	$1.0m$
Horizontal Beam Offset	$d_x = 10.0\mu m$
Vertical Beam Offset	$d_z = 10.0\mu m$
Fast Modulation frequency	$600Hz$
Modulation depth	$\triangle Q = 1.0 \cdot 10^{-4}$.

(11.1)

For $x > 2mm$ the diffusion due to the non-linear aspects of the particle motion becomes larger than the diffusion due to intra-beam scattering and thus dominates the particle diffusion in the beam halo. Because the particle diffusion increases with larger x values, an initially narrow particle distribution develops distribution tails over time.

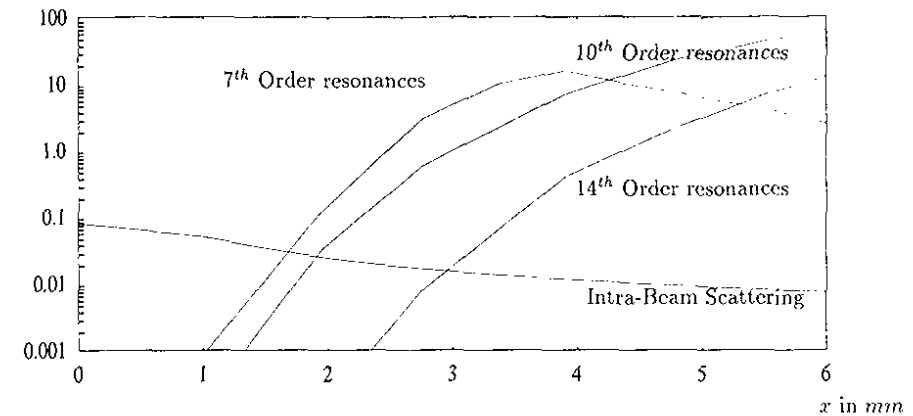

Figure 11.2:
Comparison of different diffusion mechanisms for a fast tune modulation with $600Hz$ and $\triangle Q = 1.0 \cdot 10^{-4}$. The lower curve gives the drift coefficient due to intra-beam scattering and the three upper curves show the drift coefficients for the 7^{th}, 10^{th}, and 14^{th} order sum resonances. For all curves, the betafunction is $\beta_x = 191m$ and the horizontal and vertical beam offsets are $d_y = 10\mu m$ with $\sigma_x = 0.27mm$ and $\sigma_z = 0.03mm$.

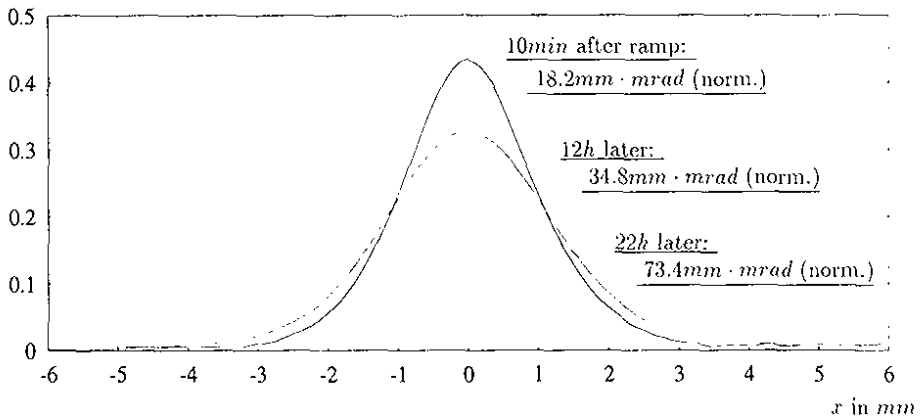

Figure 11.3:
The horizontal emittance growth in the proton storage ring of HERA during a luminosity run in 1993. The three curves show the horizontal proton distribution in HERA at three different times. The values at the curves refer to the normalized emittance at $820GeV$. The betafunction at the monitor position is $\beta_x = 191m$.

Fig.11.3 shows the horizontal proton distribution in HERA at three different times during a luminosity run in 1993. Over time the particles diffuse and fill the tails of the distribution. According to the data in Fig.11.3 the average growth rate of the normalized emittance is approximately

$$\frac{<\epsilon>}{h} \approx 1.5mm \cdot mrad, \tag{11.2}$$

and corresponds to an increase in the horizontal action of

$$< I_x > \approx 0.05 \cdot 10^{-16}/Turn. \tag{11.3}$$

The growth rate (11.3) is of the same order of magnitude as the analytical estimate of the modulation diffusion for $x \approx 1.5mm$ ($\beta_x = 191m$). The increasing number of particles in the distribution tails leads to disadvantageous background rates in the main experiments H1 and ZEUS. Thus, recognizing the high level of dependency of the particle diffusion on the modulation depths of the fast frequency components, an efficient operation of the main experiments calls for a compensation of the fast frequency components in the tune modulation spectrum. The analytical estimates for the particle diffusion suggest that the emittance growth in HERA would be smaller if the modulation depth of the $600Hz$ signal could be reduced to less than ($\Delta Q = 10^{-5}$). However, because of power supply ripples, one expects modulation depths larger than ($\Delta Q = 10^{-5}$).

Next, the analytically estimated diffusion coefficients are compared to the fitted coefficients of a diffusion measurement with the proton collimators. A detailed description of such a diffusion measurement can be found in [103]. The measured diffusion coefficients vary slightly over time and depend on the position of the collimators. Typical values for the measured diffusion coefficients during luminosity conditions vary between

$$D_{measured} = 10^{-6}(mm \cdot mrad)^2/sec, \quad \text{and } 10 \cdot 10^{-6}(mm \cdot mrad)^2/sec, \tag{11.4}$$

for $x \approx 5mm$ [103][104]. For modulation depths larger than $\Delta Q = 1.0 \cdot 10^{-5}$, the modulational diffusion yields comparable diffusion coefficients [92].

In both cases the comparison of the analytical estimates with the measured values in HERA suggests the non-linear aspects of the particle motion as the cause for the emittance growth. In this case, one expects a high dependency of the emittance growth on the tune modulation amplitudes and could be tempted to reduce the emittance growth in HERA by actively compensating the amplitudes of the fast modulation frequencies. For example, the fast frequency components could be compensated for with active filters in the power supplies. An alternative method for compensating the tune modulation in the proton storage ring is to introduce an external modulation of the proton quadrupoles. Because the fast frequency components of the tune modulation are caused by power supply ripples, the phase of the modulation signal does not vary with time. The constant phase relation allows a compensation of the fast frequency components by an additional tune modulation with the same amplitude, but with a 180° phase difference to the initial signal. The next section summarizes the results of a diffusion experiment in the proton storage ring of HERA which investigated the dependency of the particle diffusion on the modulation frequencies and amplitudes. The experimental data confirms the high dependency of the particle diffusion on the fast frequency components and indicates a strong increase in the particle diffusion for modulation amplitudes as low as $\Delta Q = 5.0 \cdot 10^{-5}$.

Section 12

Measuring the Effect of an External Tune Modulation on the Particle Diffusion in the Proton Storage Ring of HERA

The following work summarizes the main results of a diffusion experiment in the proton storage ring of HERA. The experiment was performed during a machine shift on November 6^{th}, 1993. A detailed description of the experiment and a listing of of the experimental data can be found in [92]. The aim of the HERA-p diffusion experiment was to measure the frequency dependence of the particle diffusion and to demonstrate that a tune modulation with an amplitude as low as $\Delta Q = 10^{-4}$ results indeed in a substantially large diffusion coefficient.

In the experiment, four of the superconducting quadrupoles in the proton storage ring ($QP62 - WR$ and WL) were used to create an external tune modulation of the order of $\Delta Q \sim 10^{-4}$ with a modulation frequency between $40Hz$ and $2000Hz$. The amplitude of the slow tune modulation caused by the ground motion in the HERA tunnel was measured by comparing the signal amplitudes in the proton loss rates with the signal amplitude of an external slow modulation frequency with known modulation depth. The corresponding proton diffusion was measured using the proton loss monitors and the collimators in the west arc of the proton ring.

12.1 HERA Parameters and Experimental Setup

The experiment used ten colliding electron and proton bunches at $26GeV$ and $820GeV$ respectively plus one pilot bunch for each beam. Tables (12.2) and (12.3) show the horizontal and vertical electron beam sizes $\sigma_{e,x}$ and $\sigma_{e,z}$, the revolution frequency f_{rev}, the beam currents, the corresponding numbers of particles per bunch for the electron and the proton beam (N_e and N_p), and the linear horizontal and vertical beam-beam tune shifts $\xi_{p,x}$ and $\xi_{p,z}$ for the proton beam. The number of particles per bunch is given by

$$N = \frac{I}{11 \cdot e \cdot f_{rev}}, \tag{12.1}$$

where e is the unit charge.

Electron Beam Parameters	
Electron Beam Current	$I_e = 1.0mA$
Number of Particles per Bunch	$N_e = 1.5 \cdot 10^{10}$
Relativistic γ	$\gamma_e = 62.6 \cdot 10^3$
Beam Size	$\sigma_{e,x} = 0.276mm$ | $\sigma_{e,z} = 0.046mm$
Revolution Frequency	$f_{rev} = 47.3KHz$

(12.2)

Proton Beam Parameters		
Tune Values during Experiment	$Q_x = 31.304$	$Q_z = 32.282$
Typical Tune Values in 1993	$Q_x = 31.291$	$Q_z = 32.294$
Proton Beam Current	$I_p = 1.4mA$	
Number of Particles per Bunch	$N_p = 1.8 \cdot 10^{10}$	
Relativistic γ	$\gamma_p = 874.0$	
Linear Beam-Beam Detuning	$\xi_{p,x} = 0.0004$	$\xi_{p,z} = 0.0003$
Beta Functions at the Intersection Regions	$\beta_x^* = 7m$	$\beta_z^* = 0.7m$
Beta Function at the horizontal Collimator	$\beta_x = 70m$	
Horizontal Collimator Position	$\Delta X_{Col.} \approx 5mm$	
Revolution Frequency	$f_{rev} = 47.3KHz$	

(12.3)

Due to a problem with the electron source during the experiment, the number of particles per electron bunch was smaller than the design value of $N_e = 3.7 \cdot 10^{10}$ by approximately a factor of three. Consequently, the beam-beam kick was also a factor of three smaller than the design value. The electron beam sizes were calculated using the photon detector in the H1-luminosity monitor [105]. However, due to refraction effects of the gamma beam, $\sigma_{e,z}$ merely serves as an upper estimate for the vertical electron beam size and the actual beam size can be slightly smaller than the value in Table (12.2).

In the beginning of the experiment, the proton and electron beams were brought to collision using the normal luminosity optics. Subsequently, the current in the four superconducting quadrupoles $QP62$ in the west arc of the proton ring was slowly reduced and set to zero. Table (12.4) lists the magnet parameters for the $QP62$.

$QP62$ Parameters	
Power Supply	West R/L 15162
Number of Magnets	4
Length	$l_{QP62} = 5.83m$
Inductivity	L = $0.007H$
Integrated Field Gradient	$g = 0.12T/A$
Horizontal Beta Function	$\beta_{x,QP62} = 20m$
Vertical Beta Function	$\beta_{z,QP62} = 80m$
Number of Coils	$N = 66$
Nominal Current	$I_0 = 110A$

(12.4)

The magnets were disconnected from the power supplies and connected to a frequency generator and a power amplifier. The removal of the four quadrupoles from the proton optics led to

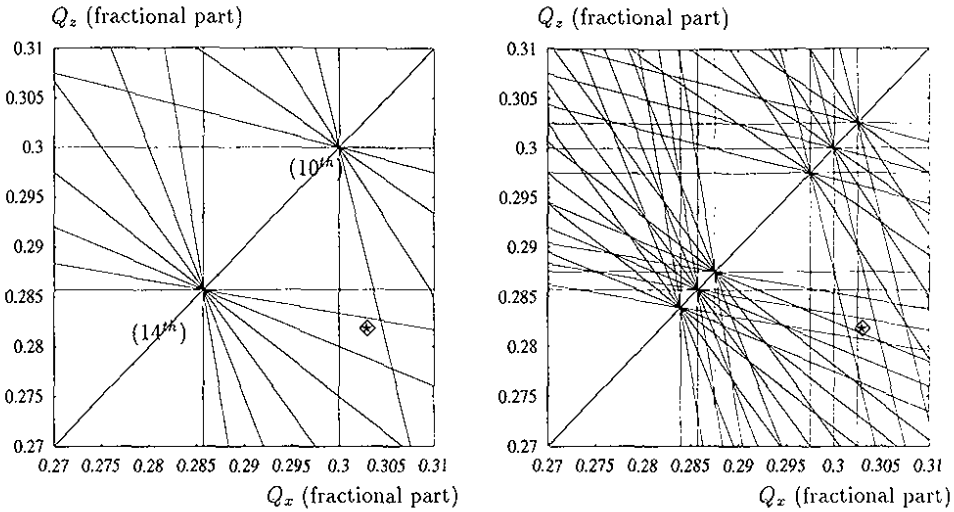

Figure 12.1:
The particle distribution in the transverse Q-diagram. The diamond-shaped box indicates the size and the position of the particle distribution.
Left: The even order resonance lines up to 14^{th} order in x and z.
Right: The even order resonance lines and their modulation sidebands for a modulation frequency of $1200Hz$.

a change in the proton tunes, which had to be compensated for by using the two quadrupole families $QP40$ and $QP42$. The procedure of disconnecting the four quadrupoles $QP62$ and correcting the tune changes by hand in the control room left the machine with tune values that were slightly different from the initial values. The final Q-values are given in Table (12.3) and the left-hand side of Fig.12.1 shows the even order sum resonances and the final position of the particle distribution in the transverse Q-diagram. The diamond-shaped box with the star indicates the size and the final position of the particle distribution between the 14^{th} and 10^{th} order sum resonances. For the parameter values (12.2) and (12.3) and a particle position near the horizontal collimator, the $(l \cdot Q_x + m \cdot Q_z = p)$ resonances with even l and m dominate over the ones with odd integers (see Fig.11.2). Without any tune modulation, the particles in the proton beam experience no low-order sum resonances and the lifetime was about $70h$. However, for an additional fast tune modulation, the proton beams might experience modulation sidebands of the 7^{th} and 10^{th} order sum resonances. The right-hand side of Fig.8.7 shows the corresponding resonance lines for a tune modulation with $1200Hz$.

After the quadrupoles were connected to the external power amplifier, a harmonic frequency generator was used to create the tune modulation. The modulation depths can be expressed as functions of the electric current I_{QP62}

$$\Delta Q_x = S(f) \cdot \beta_{x,QP62} \cdot \frac{0.2998}{\pi \cdot p[GeV]} \cdot g \cdot I_{QP62} \quad (12.5)$$

$$\Delta Q_z = S(f) \cdot \beta_{z,QP62} \cdot \frac{0.2998}{\pi \cdot p[GeV]} \cdot g \cdot I_{QP62}, \quad (12.6)$$

where $p[GeV]$ is the proton momentum and $S(f)$ the frequency dependent 'shielding factor' (6.2) in the superconducting magnets. Fig.6.2 shows the shielding factor as a function of the modulation frequency for a cold beam pipe. The voltage range of the amplifier allowed only currents up to $0.4A$ and thus limited the tune modulation to modulation depths of the order of

$$\Delta Q \sim 10^{-4}. \tag{12.7}$$

During the experiment, the modulation frequency was varied in $100Hz$ steps between $2KHz$ and $400Hz$. For each modulation frequency the corresponding diffusion coefficient was measured by moving the collimator outward by typically $0.2mm$ and recording the counting rate evolution at the proton loss monitors versus time. A subsequent fit calculation of the recorded data yields the measured diffusion coefficients [103]. In addition to this frequency range, a diffusion measurement was done for a modulation frequency of $140Hz$ and $46.4Hz$ with three different modulation depths.

Unfortunately, time did not allow for the measurement of the beam offset in the $QP62$ quadrupoles and correction of the beam misalignments in the magnets during the experiment. If the beam position at the modulated quadrupoles does not coincide with the center of the quadrupoles, the beam experiences additional dipole kicks during the tune modulation. The resulting rms closed orbit oscillation at the intersection regions becomes

$$\Delta Y_{rms,x} \approx 1.7 \cdot \Delta x \cdot \Delta Q_x, \quad \Delta Y_{rms,z} \approx 0.3 \cdot \Delta z \cdot \Delta Q_y, \tag{12.8}$$

where Δx and Δz are the horizontal and vertical orbit misalignment in the quadrupoles.

In addition to the external tune modulation in the $QP62$, the beam experiences a natural tune modulation due to the inherent power supply fluctuations [80] and due to the ground motion in the HERA tunnel [87][88][89]. During the experiment the modulation amplitudes due to the ground motion were estimated. Analyzing the loss rates at the proton loss monitors with an FFT and superimposing several FFT measurements, one clearly recognizes individual frequency components in the loss rates [91]. The periodic changes in the loss rate can be either caused by closed orbit oscillations which lead to a periodic scraping of the beam at the collimator, or by betatron tune fluctuations which modulate the mode amplitudes of the beam-beam resonances and the actual diffusion process. Assuming a tune modulation as the cause of the frequency components, the measured amplitudes can be compared with the amplitude of an external tune modulation with given amplitude. For our measurements, an external tune modulation with $46.4Hz$ was used. The $46.4Hz$ frequency was chosen because it does not appear in the natural spectrum and because the 'shielding factor' is close to unity for such a low modulation frequency. A comparison of the $46.4Hz$ signal with the frequency components between $1Hz$ and $50Hz$ indicated modulation depths of

$$\Delta Q \approx 5.0 \cdot 10^{-5} \tag{12.9}$$

for the tune modulation due to the ground motion. The measured value agrees nicely with the predicted values in [88]. Unfortunately, the relatively low counting rate at the loss monitors during the experiment did not allow for the measurement of the fast frequency components.

12.2 Analytical Estimates for the Emittance Growth

Calculating the resonance amplitudes by a numerical integration of the beam-beam potential and a subsequent FFT, one can use the expressions (9.15) and (9.18) for an analytical estimate of the drift and diffusion coefficients. The mode amplitudes of the sidebands depend on the horizontal and vertical modulation depths, the modulation frequency, the order of the sum resonance (l and m), and on the order of the sideband:

$$\tilde{A}_{l,m,p}(I_x, I_z, f, \Delta Q_x, \Delta Q_z) = J_n\left(\frac{l\Delta Q_x f_{rev}}{f_{mod}}\right) \cdot J_r\left(\frac{m\Delta Q_z f_{rev}}{f_{mod}}\right) \cdot A_{l,m,p}(I_x, I_z). \tag{12.10}$$

J_n and J_r are Bessel functions of the first kind, and n and r characterize the order of the sideband. For a tune modulation with $f > 400Hz$ and $\Delta Q \sim 10^{-4}$, the arguments of the Bessel functions are much smaller than one and only the first order modulation sidebands with $n = \pm 1$ and $r = 0$, or $n = 0$ and $r = \pm 1$ have a significant amplitude.

Table (12.11) lists the corresponding diffusion coefficients for the different modulation frequencies with $I_{QP62} = 0.4A$ and for $I_x = 240.0 \cdot 10^{-9}m$. The horizontal action value corresponds to a collimator position of $5.8mm$. The data in Table (12.11) show that the analytically calculated diffusion coefficient attains its maximum value for a tune modulation around $1000Hz$.

First Order Sidebands that Reach the Particle Distribution

l	m	$f_{mod}[Hz]$	ΔQ_x	ΔQ_z	$D[(mmmrad)^2/sec]$
2	12	1381.2	$2.75 \cdot 10^{-5}$	$1.1 \cdot 10^{-4}$	$0.9 \cdot 10^{-6}$
10	0	1135.2	$3.5 \cdot 10^{-5}$	$1.3 \cdot 10^{-4}$	$64.8 \cdot 10^{-6}$
8	2	936.5	$3.9 \cdot 10^{-5}$	$1.5 \cdot 10^{-4}$	$11.0 \cdot 10^{-6}$
4	10	690.6	$5.0 \cdot 10^{-5}$	$2.0 \cdot 10^{-4}$	$18.0 \cdot 10^{-6}$
/	/	46.7	$1.0 \cdot 10^{-4}$	$4.0 \cdot 10^{-4}$	/

(12.11)

For modulation frequencies above $1400Hz$ or below $400Hz$ Equations (9.15) and (9.18) do not indicate an enhanced particle diffusion and the diffusion coefficient should attain the normal background value. It is remarkable that the diffusion coefficients in Table (12.11) are larger than the measured diffusion coefficients under the normal luminosity condition without any external tune modulation. A typical value for the measured diffusion coefficient is found in [103]

$$D_{measured} \sim 1.0 \cdot 10^{-6}[mm \cdot mrad]^2 \cdot sec^{-1}. \tag{12.12}$$

This is particularly interesting because the resonance mode amplitudes were calculated for an electron current which is only about one third of the design value. Hence, for the design value of $3.7 \cdot 10^{10}$ electrons per bunch, the analytical estimates of the diffusion coefficients are again one order of magnitude larger than the values in Table (12.11) and are thus two orders of magnitude larger then the measured diffusion coefficients in [103].

12.3 Experimental Data

The diffusion measurements started during the early shift of November 6, 1993, and lasted for approximately three hours. During the experiment, the modulation frequency was altered

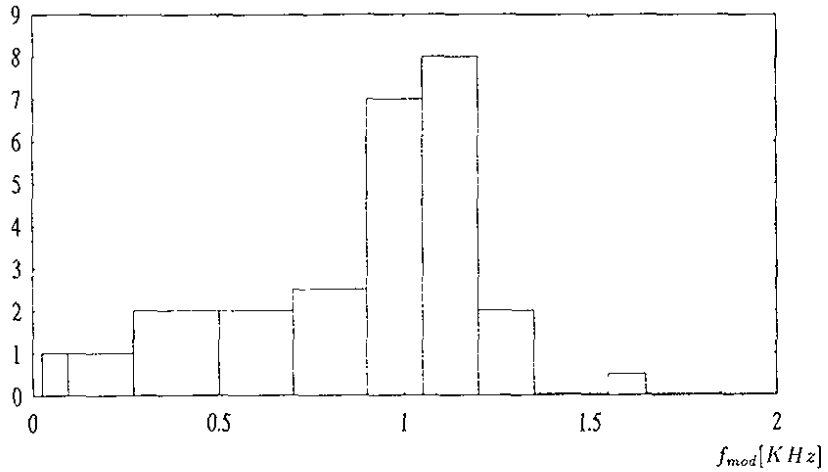

Figure 12.2:
Increase in the loss rate at the proton loss monitors for different modulation frequencies. For all modulation frequencies except for the $46.4Hz$*, the modulation depth was* $I_{QP62} = 0.4A$ *with* $\Delta Q \sim 10^{-4}$.

between $f = 2.0KHz$ and $f = 46.4Hz$ with $I_{QP62} \in [0.02A, 0.6A]$. A quadrupole current of $I_{QP62} = 0.4A$ corresponds to a tune modulation depth of $\Delta Q \sim 1.0 \cdot 10^{-4}$. Starting with a modulation frequency of $2.0KHz$ and a quadrupole current of $I_{QP62} = 0.4A$, the modulation frequency was lowered in $100Hz$ steps. For each modulation frequency the corresponding diffusion coefficient was evaluated by a fit calculation to the loss rates at the proton loss monitors. The values of a diffusion measurement typically vary within a range of $\pm 30\%$ around the average value and a reliable estimate for the particle diffusion in the proton beam relies on a sufficiently large number of measurements. Because the diffusion experiment was limited to only 3 hours, time did not allow for a large number of measurements for each modulation frequency. Consequently, a diffusion measurement could not be performed for all modulation frequencies and for some frequencies the diffusion coefficients could only be measured once. Thus, the measured diffusion coefficients can serve only as a rough estimate for the particle diffusion in the proton beam. The relative change in the measured diffusion coefficients and the rate at the loss monitors offers a better interpretation of the experimental data.

Fig.12.2 shows the increase in the loss rates due to the tune modulation for different modulation frequencies. For all frequencies the current in the quadrupoles was $I_{QP62} = 0.4A$. Table (12.13) lists the average values for the measured diffusion coefficients for different

modulation frequencies.

The Measured Diffusion Coefficients		
$f[Hz]$	$I_{QP62}[A]$	$D[[mm \cdot mrad]^2 \cdot sec^{-1}]$
0.0	0.0	$27.0 \cdot 10^{-6}$
1300.0	0.4	$72.0 \cdot 10^{-6}$
1200.0	0.4	$260.0 \cdot 10^{-6}$
800.0	0.4	$210.0 \cdot 10^{-6}$
400.0	0.4	$180.0 \cdot 10^{-6}$
46.4.0	0.6	$67.0 \cdot 10^{-6}$

(12.13)

In both cases, the experimental data show a high degree of dependency on the frequencies of the fast tune modulation and agree qualitatively as well as quantitatively with the analytical estimates in Table (12.11). The increase in the loss rates at the proton loss monitors as well as the measured diffusion coefficients attain their largest values for modulation frequencies in the analytically predicted frequency range of $f_{mod} \in [0.6KHz, 1.3KHz]$. Changing the modulation frequency in $100Hz$ steps, the rate at the proton loss monitors and the measured diffusion coefficients increased by almost one order of magnitude for a tune modulation with $f \in [0.8KHz, 1.3KHz]$ and a constant quadrupole current of $I_{QP62} = 0.4A$. For modulation frequencies above $1.3KHz$ or below $400Hz$ the loss rate and the measured diffusion coefficients did not differ substantially from the values without any tune modulation.

The experiment showed large diffusion coefficients for modulation depths as low as $\Delta Q = 1.0 \cdot 10^{-4}$. Recognizing that the electron current during the diffusion experiment was less than the design value by a factor of three, the analytical estimates of the diffusion coefficients for the design currents predict a further increase in the diffusion coefficients by one order of magnitude. Thus, for the design beam intensities, one expects substantial diffusion coefficients for tune modulation depths as low as $\Delta Q = 3.0 \cdot 10^{-5}$. Such small modulation depths are of the same order of magnitude as the natural tune modulation due to the inherent power supply ripple [80] and the ground motion in the HERA tunnel [88]. Thus, one could conjecture that the emittance growth in the proton beam during luminosity operation is caused by the non-linear particle dynamics under the combined influence of the beam-beam interaction and tune modulation.

Assuming the tune modulation as the cause for the proton emittance growth during luminosity operation, one could attempt to manipulate the particle diffusion by a controlled external excitation of a tune modulation with selected frequency components. There are at least two potential applications for using an external tune modulation during the luminosity runs. By removing the quadrupoles permanently from the proton optics and connecting the magnets to a frequency generator, one can compensate for harmful frequency components in the natural modulation spectrum and hence reduce the particle diffusion and the resulting background rates in the main experiments H1 and ZEUS. Another potential application would be to generate frequency components that create a local particle diffusion in the beam halo, which would be useful for the HERA-B experiment.

Section 13

Summary

Expanding the existing models for the particle motion in a storage ring to include modulation effects with more than one frequency component, the thesis analyzed the particle diffusion due to the combined effect of non-linear fields and tune modulation. As the diffusion mechanisms do not depend on the specific arrangement of the magnets inside the storage ring, the thesis analyzed the diffusion mechanisms first on a model structure for the storage ring and applied the results of this model analysis in a second step to the particle dynamics in existing storage rings. Including modulation effects with more than one frequency component into the stability analysis of the particle dynamics, the thesis demonstrated how a tune modulation with more than one frequency component can limit the long-term stability of the particle motion in a storage ring.

In a first part, the thesis illustrated how the combined effect of non-linear fields and a tune modulation with more than one frequency component can drastically reduce the dynamic aperture of a storage ring. The results agree with the experimental data of diffusion experiments in the SPS at CERN [8].

In addition to estimating the limiting effects of the tune modulation on the dynamic aperture, the work analyzed the particle diffusion well inside the dynamic aperture. Using existing diffusion models from non-linear dynamics, analytical estimates for the particle diffusion in HERA during luminosity operation were derived as functions of the phase space position, the strength of the non-linear fields, and the modulation parameters.

At $820GeV$ the beam-beam interaction strongly affects the proton beam lifetime in HERA. While the proton beam lifetime at $820GeV$ is larger than $1000h$ without beam-beam interaction, the beam lifetime drops to about $100h$ when the electron and proton beams are brought to collision. Because the efficiency of the main experiments in HERA increases with a large proton beam lifetime and low background rates, these two conditions are desirable for the luminosity operation.

An analytical understanding of the underlying mechanisms for the decreased beam lifetime and the increased background rates during the luminosity operation are the prerequisites for optimizing the efficiency of HERA. The analytical estimates for the particle diffusion show that even for modulation depths as small as $\Delta Q = 10^{-4}$, the combined effect of a tune modulation with fast and slow frequency components and the non-linear beam-beam interaction leads to emittance growth rates of the same order of magnitude as the observed rates during the luminosity operation in HERA. While the intra-beam scattering is the dominant source for an emittance growth in the beam core at $820GeV$, the non-linear aspects of the particle dynamics dominate the particle diffusion at distances larger than one sigma of the proton beam. In order

to obtain sufficiently small growth rates in the proton storage ring, the modulation amplitudes of the $150Hz$, $300Hz$, $600Hz$, $750Hz$, and $900Hz$ components in the ripple spectrum of the proton power supplies must be clearly smaller than $\Delta Q = 1.0 \cdot 10^{-4}$.

Furthermore, the analytical estimates predict a high sensitivity to the particle diffusion on the frequencies of the fast tune modulation. This prediction regarding the growth rates was confirmed by a subsequent modulation experiment in the proton storage ring of HERA, where an external tune modulation with $\Delta Q \sim 10^{-4}$ led to a drastic increase in the growth rates. While the loss rates at the proton loss monitors increased by more than one order of magnitude for modulation frequencies between $600Hz$ and $1200Hz$, the rates showed no significant increase for modulation frequencies smaller than $400Hz$, or larger than $1200Hz$.

Both the analytical estimates and the experimental data indicate that the emittance growth rates are highly sensitive to the fast modulation frequencies and can be manipulated by an external tune modulation. Such an additional external tune modulation has two potential applications for HERA. First, assuming the combined effect of the non-linear beam-beam interaction and the natural tune modulation in HERA as the cause for the emittance growth in the proton storage ring of HERA, a controlled tune modulation can be used to compensate for harmful frequency components in the natural modulation spectrum of the proton storage ring, and hence to reduce the particle diffusion and the background rates in the main experiments. Second, the additional tune modulation can be used to generate frequency components that create a local particle diffusion in the beam halo which would be useful for the HERA-B experiment. The analytical and experimental results of this thesis form the prerequisites for realizing such an active manipulation of the emittance growth rates in HERA.

Acknowledgments

I want to express my gratitude to the DESY directorate for giving me the possibility to write a thesis in the field of accelerator physics and for financial support.

I would like to thank Prof. Dr. J. Bartels and Dr. H. Mais for their continuous interest and support and for making this thesis possible.

Special thanks to Dr. F. Willeke for many helpful and valuable suggestions and for making the HERA diffusion experiment possible.

Thanks to Dr. R. Brinkmann for innumerable helpful discussions.

I would like to thank Dr. K. - H. Meß and Dipl.Phys. M. Seidel for their support during the HERA diffusion experiment.

I am grateful to Prof. Dr. P. Schmüser for helpful discussions.

Thanks to Dr. R. Bacher, Dipl. - Ing. H. - J. Eckoldt, and Dr. J. - P. Jensen for interesting discussions and helpful information about the HERA-p power supplies.

Thanks to Dr. H. Mais, Dr. A. Pauluhn, and Mrs. P. K. Read for carefully reading the manuscript.

The continuous support from Dr. M. Böge on the HP-cluster is warmly acknowledged.

Furthermore, I want to thank the MPY group at DESY for providing excellent working conditions and for giving me the opportunity to participate in the commissioning of HERA.

I would like to thank my colleagues Dr. Michael Böge, Dipl.Phys. Winfried Decking, Dr. Klaus Flöttmann, and Dr. Anuschka Pauluhn for providing a nice atmosphere and for many illuminating discussions.

Thanks to Dr. F. Zimmermann for various discussions and for supplying an injection optics for SIXTRACK.

Furthermore, I am grateful for the hospitality experienced at the Brookhaven National Laboratory during the 1992 workshop on long-term stability in storage rings.

I would also like to thank Dr. J. Gareyte and Dr. F. Schmidt from the CERN SL Division for their hospitality during the 1992 SPS diffusion experiment at CERN.

Finally, I want to thank my wife for her patience and her continuous support.

List of Figures

Appendix A

The Beam-Beam Kick in the Padé Approximation for the Complex Error Function

Following the work from M. Basseti and G.A. Erskine [61] one can write the beam-beam kicks of a flat electron beam in terms of the complex error function

$$\Delta p_x = C \cdot Im\left[W\left(\frac{x+iz}{\sqrt{2(\sigma_x^2-\sigma_z^2)}}\right) - e^{-\left[\frac{x^2}{2\sigma_x^2}+\frac{z^2}{2\sigma_z^2}\right]} \cdot W\left(\frac{x\frac{\sigma_x}{\sigma_z}+iz\frac{\sigma_x}{\sigma_z}}{\sqrt{2(\sigma_x^2-\sigma_z^2)}}\right)\right] \quad (A.1)$$

$$\Delta p_z = C \cdot Re\left[W\left(\frac{x+iz}{\sqrt{2(\sigma_x^2-\sigma_z^2)}}\right) - e^{-\left[\frac{x^2}{2\sigma_x^2}+\frac{z^2}{2\sigma_z^2}\right]} \cdot W\left(\frac{x\frac{\sigma_x}{\sigma_z}+iz\frac{\sigma_x}{\sigma_z}}{\sqrt{2(\sigma_x^2-\sigma_z^2)}}\right)\right] \quad (A.2)$$

$$C = \frac{N_b r_p}{\gamma_p} \cdot \sqrt{\frac{2\pi}{\sigma_x^2-\sigma_z^2}}, \quad (A.3)$$

where W is the complex error function [58]

$$W(z) = e^{-z^2} \cdot erfc(-iz), \quad z \in \mathbf{C}. \quad (A.4)$$

Following the work in [9] the calculation of an approximation for the beam-beam kick is done in three steps. First, for a vanishing real part of the argument in W, the complex error function has real values and can be approximated by [58]

$$W(i|z|) = \frac{1}{1+p\cdot z} \cdot \left(a + \frac{1}{1+p\cdot z} \cdot \left(b + \frac{c}{1+p\cdot z}\right)\right), \quad |z| \geq 0, \quad (A.5)$$

with $p = 0.47047$, $a = 0.34802$, $b = -0.09588$, and $c = 0.74786$.

In a second step, the expression (A.5) is extended to complex arguments with non-vanishing real part. In this approximation, the beam-beam kicks are continuous in the Cartesian variables x and z and the imaginary part of (A.5) turns out to be a sufficiently accurate approximation for the horizontal beam-beam kick.

However, the approximation (A.5) for the real part of $W(x+i\cdot z)$ becomes bad with increasing x especially in the region of small z. This problem is corrected in a third step.

Subtracting the complex error function approximation with argument $(x + i \cdot 0)$ from the expression (A.5), one obtains for the vertical beam-beam kick

$$\begin{aligned}\Delta p_z &= C \cdot Re\left[W\left(\frac{x+iz}{\sqrt{2(\sigma_x^2-\sigma_z^2)}}\right) - e^{-\left[\frac{x^2}{2\sigma_x^2}+\frac{z^2}{2\sigma_z^2}\right]} \cdot W\left(\frac{x\frac{\sigma_z}{\sigma_x}+iz\frac{\sigma_x}{\sigma_z}}{\sqrt{2(\sigma_x^2-\sigma_z^2)}}\right)\right. \\ &\left. -W\left(\frac{x}{\sqrt{2(\sigma_x^2)}}\right) - e^{-\left[\frac{x^2}{2\sigma_x^2}\right]} \cdot W\left(\frac{x\frac{\sigma_z}{\sigma_x}}{\sqrt{2(\sigma_x^2-\sigma_z^2)}}\right)\right].\end{aligned} \tag{A.6}$$

The extension of Equations (A.1) and (A.6) to negative values of x and z is given by

$$\Delta p_x(-x,z) = \Delta p_x(-x,-z) = -\Delta p_x(x,z) \tag{A.7}$$

$$\Delta p_z(x,-z) = \Delta p_z(-x,-z) = -\Delta p_z(x,z). \tag{A.8}$$

While the approximations (A.1) and (A.6) agree well with the exact expressions for the beam-beam kicks, the computing time needed for (A.1) and (A.6) is much faster than a library call of the complex error function.

Appendix B

Melnikov-Arnold Integral

The Melnikov-Arnold Integral refers to the integral expression

$$\mathcal{A}_\varpi(\lambda) = \int_{-\infty}^{+\infty} \exp\left[i\left(\frac{\varpi}{2}\cdot\phi_{sep}(\tau) - \lambda\cdot\tau\right)\right]d\tau, \tag{B.1}$$

where ϕ_{sep} is the separatrix solution for the angle variable of the standard pendulum

$$\phi_{sep}(\tau) = 4\cdot\arctan\left[\exp\tau\right] - \pi. \tag{B.2}$$

Following the work in [36], the integral in (B.1) can be rewritten as

$$\mathcal{A}_\varpi(\lambda) = \int_{-\infty}^{+\infty} e^{-i\lambda\cdot\tau}\cdot\left(\frac{1+i\exp\tau}{i+\exp\tau}\right)^\varpi d\tau. \tag{B.3}$$

For $\lambda > 0$ one can close the integral in the lower complex half plane and solve Equation (B.3) by evaluating the residues of the integrand. The integrand has poles at

$$\tau_n = -i\pi\cdot\left(\frac{1+n\cdot 4}{2}\right). \tag{B.4}$$

For the evaluation of (B.3) Chirikov looks at the two different cases of integer ϖ and fractional ϖ.

First, the case of integer ϖ is summarized. Looking at the contour integral in Fig.B.1, the contribution of the (3) integral vanishes for $lim_{T\to\infty}$ and $lim_{\tau_c\to\infty}$ as long as the contour integral is constructed such that

$$\lambda\cdot\tau_c \gg T. \tag{B.5}$$

The integrals (1) and (2) do not vanish for $lim_{T\to\infty}$ and $lim_{\tau_c\to\infty}$, but have only a purely oscillating contribution. The definition of the Melnikov-Arnold integral consists in neglecting this oscillating contribution of the contour integral and to consider only the non-oscillating part of the integral [36][13]. A convenient presentation of the Melnikov-Arnold integral is to give its recursion formula. Evaluating the residues in (B.3) one gets for $\lambda > 0$

$$\mathcal{A}_1(\lambda) = \frac{2\pi\exp\left[\pi\lambda/2\right]}{\sinh\left(\pi\lambda\right)} \tag{B.6}$$

$$\mathcal{A}_2(\lambda) = 2\lambda\mathcal{A}_1(\lambda) \tag{B.7}$$

$$\mathcal{A}_\varpi(\lambda) = \frac{2\lambda\mathcal{A}_{\varpi-1}(\lambda)}{(\varpi-1)} - \mathcal{A}_{\varpi-2}(\lambda) \tag{B.8}$$

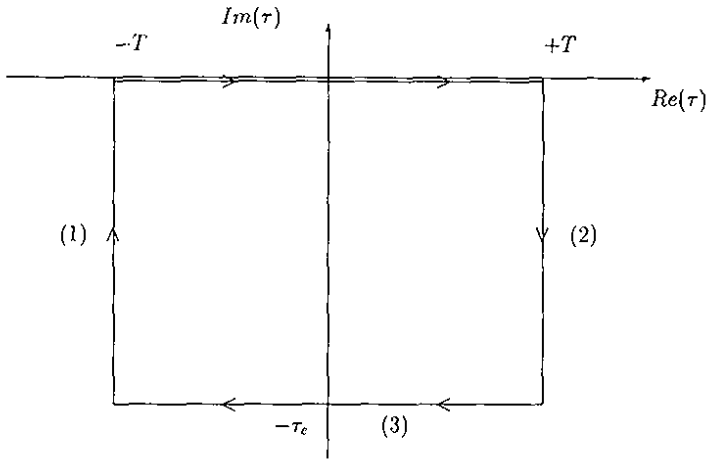

Figure B.1: *The contour integral for the Melnikov-Arnold Integral.*

and for $\lambda < 0$

$$\mathcal{A}_\varpi(\lambda) = (-)^\varpi \cdot \mathcal{A}_\varpi(|\lambda|) \cdot \exp[-\pi|\lambda|/2]. \tag{B.9}$$

In a second step, the case of fractional ϖ is considered. Choosing the integral contour such that the poles (B.4) are excluded from the area inside the contour integral, the integral (B.3) can be expressed as a sum of the purely oscillating contribution and the Gamma function given by the Hankel contour integral [36]. Neglecting again the oscillating contribution, one gets for the Melnicov-Arnold integral for fractional ϖ and $\lambda > 0$

$$\mathcal{A}_\varpi(\lambda) \approx \frac{4\pi(2\lambda)^{m-1}}{\Gamma(\varpi)} \cdot e^{\lambda\pi/2}. \tag{B.10}$$

For fractional ϖ and $\lambda < 0$ one gets

$$\mathcal{A}_\varpi(\lambda) \approx \frac{4 \cdot e^{-\pi|\lambda|/2}}{(2|\lambda|)^{\varpi+1}} \cdot \Gamma(\varpi+1) \cdot \sin(\pi\varpi). \tag{B.11}$$

Appendix C

Deprit Perturbation Theory

The calculation of the series for a normal form using the perturbation theory of Poincaré and von Zeipel becomes extremely tedious when the perturbation theory is exploit to higher than second order in the perturbation parameter. The Deprit perturbation theory uses Lie Transformation methods rather than mixed variable generating functions and thus allows the use of computer algorithms for the calculation of the normal form. The following description summarizes the work in [13].

Let $\vec{x} = (\vec{I}, \vec{\phi})$ be the vector of the generalized momenta and coordinates representing the system in phase space of the perturbed Hamilton function

$$H(\vec{x}) = H_0\left(\vec{I}\right) + \varepsilon \cdot H\left(\vec{I}, \vec{\phi}, s\right). \tag{C.1}$$

The integrable Hamiltonian H_0 depends only on the action variables $\vec{I}$. The idea of the Deprit perturbation theory is to generate a new set of canonical variables with the evolution operator of a 'Hamiltonian' w, with 'time variable' ε:

$$\frac{d\vec{\bar{x}}}{d\varepsilon} = \left[\vec{\bar{x}}, w\right]. \tag{C.2}$$

The components of (C.2) are just Hamilton's equations in Poisson bracket notation. w is also called a Lie generating function [13]. Equation (C.2) generates a canonical transformation and for any ε and initial point $\vec{x}$, the solution $\vec{\bar{x}}$ of (C.2) represents a transformation from $\vec{x}$ to $\vec{\bar{x}}$ which satisfies the Poisson bracket.

Introducing the evolution operator T, which evaluates any function g at the transformed point $\vec{\bar{x}}(\vec{x}, \varepsilon)$, and the Lie operator L

$$L = [w, \ ], \tag{C.3}$$

one can construct a perturbation series that transforms the perturbed Hamilton function (C.1) to normal form. The time evolution of the operator T is given by

$$\frac{dT}{d\varepsilon} = -TL. \tag{C.4}$$

A transformation from old to new variables can now be written as

$$\vec{\bar{x}} = T\vec{x}, \tag{C.5}$$

and the correct form for transforming the Hamilton function (C.1) to the new set of coordinates reads [13]

$$\bar{H} = T^{-1}H + T^{-1}\int_0^{\epsilon} d\epsilon' T(\epsilon')\frac{\partial w(\epsilon')}{\partial t}. \qquad (C.6)$$

Expanding w, L, T, H, and $\bar{H}$ into power series in ϵ

$$w = \sum_{n=0}^{\infty} \epsilon^n w_{n+1} \qquad (C.7)$$

$$L = \sum_{n=0}^{\infty} \epsilon^n L_{n+1} \qquad (C.8)$$

$$T = \sum_{n=0}^{\infty} \epsilon^n T_n \qquad (C.9)$$

$$H = \sum_{n=0}^{\infty} \epsilon^n H_n \qquad (C.10)$$

$$\bar{H} = \sum_{n=0}^{\infty} \epsilon^n H_n, \qquad (C.11)$$

inserting the expansions into (C.4) and equating equal powers of ϵ one obtains a recursion formula for the evolution operator T

$$T_n = -\frac{1}{n}\sum_{m=0}^{n-1} T_m L_{n-m} \qquad (C.12)$$

With $T_0 = 1$, Equation (C.12) yields T_n in terms of the L_n in all orders.

In order to obtain the n^{th} order perturbation equation, one must premultiply (C.6) with T and differentiate with respect to ϵ. Inserting the series expansions and equating like powers of ϵ, one gets finally

$$D_0 w_n = n \cdot \left(\bar{H}_n - H_n\right) - \sum_{m=1}^{n-1}\left(L_{n-m}H_m + mT^{-1}_{n-m}H_m\right), \qquad (C.13)$$

with

$$D_0 \equiv \frac{\partial}{\partial s} + [\,, H_0]. \qquad (C.14)$$

In contrast to the mixed variable transformations in the perturbation theory of Poincaré and von Zeipel, the Poisson Brackets in (C.13) can be calculated with the help of a computer code that evaluates the commutator relations. This formalism can be used to calculate the non-linear detuning terms for the sextupole kicks up to high orders in the perturbation parameter ϵ.

Bibliography

[1] 'Catalogue of High Energy Accelerators',
XIV International Conference on High Energy Accelerators, Tsukuba, Japan

[2] HERA: 'A Proposal for a Large Electron - Proton Colliding Beam Facility at DESY',
DESY - HERA 81-10 (1981)

[3] H1, Letter of Intent (1986).

[4] ZEUS, Letter of Intent (1986).

[5] HERMES, Letter of Intent (1990).

[6] HERA-B, *Letter of Intent*,
DESY-PRC 92/04 (October 1992)

[7] P. Zahng, SR.P. Johnson, M. Kuchinir, D. Siergiej and D. Wolff,
'Common Mode Noise on the Main Tevatron Bus and Associated Beam Emittance Growth',
FERMILAB-Conf-91/139 (May 1991)

[8] X.Altuna, C.Arimatea, R.Bailey, T.Bohl, D.Brandt, K.Cornelis, C.Depas, F.Galluccio, J.Gareyte, R.Giachino, M. Giovannozzi, Z.Guo, W.Herr, A.Hilaire, T.Lundberg, J.Miles, L.Normann, T.Risselada, W.Scandale, F.Schmidt, A.Spinks, M.Venturini,
'*The 1991 Dynamic Aperture Experiment at the CERN SPS*',
CERN SL/91-43 (AP), LHC Note 171, (1991)

[9] R. Brinkmann (DESY),
'A Simulation Study for the Beam-Beam Interaction of Protons with a Flat Electron Beam in HERA',
DESY HERA 89-24 (November 1989)

[10] F. Willeke, private communication (1993).

[11] H. Poincaré,
'Les Methodes Nouvelles de la Mécanique Céleste',
Gauthier-Villars, Paris, (1892).

[12] H. von Zeipel,
Ark. Astron. Mat. Fys. 11.No. 1, (1916).

[13] A.J. *Lichtenberg and M.A. Lieberman*,
'Regular and Stochastic Motion',
Springer (1983)

[14] D.K.Arrowsmith and C.M Place,
'An Introduction to Dynamical Systems',
Cambridge University Press, (1990)

[15] A.N. Kolmogorov,
'Preservation of conditionally periodic movements with small change in the Hamilton function',
Dokl. Akad. Nauk. SSSR **98**,527, (1954)

[16] V. I. Arnold,
'On the Behavior of an Adiabatic Invariant Under Slow Periodic Variation of the Hamiltonian',
Sov. Math. Dokl.**3**,85, (1963).

[17] J. Moser,
'On Invariant Curves of Area-Preserving Mappings on an Annulus',
Nachr. Akad. Wiss. Göttingen. Math. Phys. K1, p.1. (1962).

[18] H. Goldstein,
'Classical Mechanics',
Addison-Wesley Publishing Company, World Student Series (1980).

[19] A.J. Dragt and J.M. Finn,
'Lie Series and Invariant Functions for Analylitic Symplectic Maps'
J. Math. Phys. **17**, 2215 - 2227, (1976).

[20] A.J. Dragt and J.M. Finn,
'Normal Form for Mirror Machine Hamiltonians',
J. Math. Phys. **20**, 2649 - 2660, (1979).

[21] A.J. Dragt and E. Forest,
'Computation of nonlinear behavior of Hamiltonian systems using Lie algebraic methods',
J. Math. Phys. **24**, 2734 - 2744, (1983).

[22] É. Forest,
'Lie Algebraic Maps And Invariants Produced By Tracking Codes',
Part. Acc., Vol.**22**, pp. 15 - 34, (1987).

[23] É. Forest,
'A Hamiltonian-free description of single-particle dynamics in hopelessly complex periodic systems',
LBL preprint LBL-**28471**,J. Math. Phys. **31**, 1133 - 1144, (1990)

[24] M. Berz,
'Differential-algebraic description of beam dynamics to very high orders',
Part. Acc. **24**, 109. (1989).

[25] É. Forest, M. Berz and J. Irwin,
'Normal form methods for complicated periodic systems: a complete solution using differential algebra and Lie operators',
Part. Acc. **24**, 91, (1989).

[26] R.L. Warnock and R.D. Ruth,
'Invariant Tori Through Direct Solutions Of The Hamilton-Jacobi Equation',
Physica D **26**, 1 - 36, (1987).

[27] W.E. Gabella, R.D. Ruth and R.L. Warnock,
'Computation of Invariant Tori in $2\frac{1}{2}$ Degrees of Freedom',
SLAC-PUP-5414 (T/A), (1991).

[28] M. Berz,
'COSY INFINITY Version 6',
Proceedings of the International Workshop on Nonlinear Problems in Accelerator Physics held in Berlin, Germany (1992).

[29] F. Schmidt,
'SIXTRACK, Version 1.1, Single Particle Tracking Code treating Transverse Motion with Synchrotron Oscillations in a Symplectic Manner',
CERN SL/**90-52**(AP), (1991).

[30] J. Ford and G.H. Lunsford,
'Stochastic Behavior of Resonant Nearly Linear Oscillator Systems in the Limit of Zero Nonlinear Coupling',
Physical Review A, Vol.**1**,1, 59 - 70, (1969).

[31] M.A. Lieberman and A.J. Lichtenberg,
'Stochastic and Adiabatic Behavior of Particles Accelerated by Periodic Forces',
Physical Review A, Vol.**5**,4, 1852 - 1866 (1971).

[32] A.J. Dragt and J.M. Finn,
'Insolubility of Trapped Particle Motion in a Magnetic Dipole Field',
J. Geophys. Res. **81**, 2327 (1976).

[33] M. Henon,
'Numerical study of quadratic area-preserving mappings',
Q. Appl. Math. **27**, 291 (1969).

[34] M.V. Berry,
'Regular and irregular motion',
in 'Topics in Nonlinear Dynamics - a Tribute to Sir Edward Bullard' AIP Conf. Porc. **46**(1978).

[35] J.M. Greene,
'A Method for Determining a Stochastic Transition',
J. Math. Phys. **20**(6) (1978).

[36] B.V. Chirikov,
'A Universal Instability of Many-Dimensional Oscillator Systems',
Physics Reports **52**, 263-379 (1979)

[37] V.I. Arnold,
'Stability Problem and Ergodic Properties of Classical Dynamical Systems',
Proc. Intern. Congress of Mathematics, Moscow (1966).

[38] G.V. Gadiyak, F.M. Izraelev and B.V. Chirikov,
'Numerical Experiments on a Universal Instability in Nonlinear Oscillator Systems (the Arnold Diffusion)',
Proc. 7^{th} Intern. Conf. on Nonlinear Oscillations, Berlin 1975.

[39] B.V. Chirikov,
'Research Concerning the Theory of Nonlinear Resonance and Stochasticity',
Preprint 267, Institute of Nuclear Physics, Novosibirsk (1969), (Engl. Trans., CERN Trans. 71-40, 1971).

[40] N.N. Nekhoroshev,
'An exponential estimate of the time of stability of nearly integrable Hamiltonian systems',
Uspekhi Mat. Nauk 32(6), 5,
English translation: Russian Math. Surveys 32(6), 1 (1977).

[41] G. Turchetti,
'Nekhoroshev Stability Estimates for Symplectic Maps and Physical Application',
in Number Theory and Physics, Springer (1990).

[42] G.D. Birkhoff,
'Surface Transformations and Their Dynamical Application',
Acta Math., **43**, *1 - 119 (1920)*.

[43] R.L. Warnock and R.D. Ruth,
'Long-Term Stability of Orbits in Storage Rings',
SLAC-PUP-5273 (T/A) (1990).

[44] R.L. Warnock and R.D. Ruth,
'Stability of Orbits in Nonlinear Mechanics for Finite but Very Long Times',
SLAC-PUP-5304 (T/A) (1990).

[45] R.L. Warnock and R.D. Ruth,
'Stability of Nonlinear Hamiltonian Motion for Finite but Very Long Times',
SLAC-PUP-5387 (T/A) (1991).

[46] A. Wrulich,
'RACETRACK: a computer code for the simulation of nonlinear particle motion in accelerators',
DESY 84-026 (1984).

[47] G. Benettin, G.L. Vecchio and A. Tenenbaum,
'Stochastic transition in a two-dimensional Lennard-Jones system',
Phys. Rev. **A22**, 1709 (1980).

[48] J.M. Greene and J.S. Kim,
'The calculation of Lyapunov Spectra',
Physica **24D**, 213.

[49] H. Mais, A. Wrulich, F. Schmidt (1985),
'Studies of chaotic behaviour in HERA caused by transverse magnetic multipole fields',
DESY M-85-08 and IEEE Trans. Nucl. Sci. **32**, 2252 (1987).

[50] F. Schmidt,
'Untersuchungen zur dynamischen Akzeptanz von Protonenbeschleunigern und ihre Begrenzung durch chaotische Bewegung',
DESY-HERA 88-02 (1988).

[51] R. Brinkmann and F. Willeke
'Persistant Current Field Errors and Dynamic Aperture of the HERA Proton Ring',
DESY HERA **88-08**(1988)

[52] F. Zimmermann and F. Willeke,
'Long Term Stability and Dynamic Aperture of the HERA Proton Ring',
DESY HERA **91-08**(1991).

[53] F. Zimmermann,
'Emittance Growth and Proton Beam Lifetime in HERA',
DESY **93-059**(1993).

[54] B.V. Chirikov, M.A.Lieberman, D.L.Shepelyansky and F.M.Vivaldy,
'A Theory Of Modulational Diffusion',
Physica 14D, 289-304, (1985).

[55] E. Courant and H. Snyder,
'Theory of the Alternating-Gradient-Synchrotron',
Annals of Physics **3**, 1-48 (1958)

[56] F. Willeke and G. Ripken,
'Methods of Beam Optics',
DESY 88-114 (August 1988)

[57] H. Mais,
'Introduction to Beam-Beam Effects',
DESY-PRC 92/04 (October 1991)

[58] M. Abramowitz, A. Stegun,
'Pocketbook of Mathematical Functions',
Verlag Harri Deutsch

[59] A. Deprit,
'Canonical transformations depending on a small parameter',
Cel. Mech. **1**,12 (1969)

[60] O. Brüning (DESY),
'Emittance Growth in Proton Storage Rings due to the Combined Effect of Tune Modulation and Beam-Beam Interaction for Round Beams',
DESY-HERA 93-05 (May 1993).

[61] M. Bassetti and G.A. Erskine,
'Closed Expressions for the Electrical Field of a Two-Dimensional Gaussian Charge', CERN ISR-TH/80-06 (1980)

[62] O. Brüning (DESY),
'An estimate of the diffusion in the HERA-p FODO cell',
Int. J. Mod. Phys. A (Proc. Suppl.) 2A, 418 (1992)

[63] N.N. Bogoliubov and Yu.A. Mitropolsky,
'Asymptotic Methods in the Theory on Nonlinear Oscillations',
Hindustan Publ. Corp., Dehli, (1961).

[64] David Bensimon and Leo P. Kadanoff,
'Extended Chaos and Disappearence of KAM Trajectories',
Physica **13**D, (1984) 82-89.

[65] R.S. MacKay and I.C. Percival,
'Converse KAM: Theory and Practice',
Commun. Math. Phys. 98, (1985) 469-512.

[66] R.S. MacKay, J.D. Meiss and J. Stark,
'Converse KAM theory for symplectic twist maps',
Nonlinearity 2, (1989) 555-570.

[67] N.W. Murray
'Critical function for the standard map',
Physica D52, (1991) 220-245.

[68] V.K. Melnikov,
Dokl. Akad. Nauk. SSSR, **144**, (1962) 747; **148**, (1963) 1257.

[69] S. Wiggins,
'Chaotic Transport',
Springer Verlag, 1993.

[70] V.K. Melnikov,
'On the stability of the center for time periodic perturbations',
Trans. Moscow Math. Soc. **12**, 1 (1963).

[71] D.F. Escande,
'Stochasticity in Classical Hamiltonian Systems: Universal Aspects',
Physics Reports 121, Nos. 3&4, (1985) 165-261.

[72] D.F. Escande and F. Doveil,
'Renormalization Method for Computing the Threshold of the Large-Scale Stochastic Instability in Two Degrees of Freedom Hamiltonian Systems',
Journal of Statistical Physics, Vol. 26 **2**, 1981 257-284.

[73] D.F. Escande and F. Doveil,
'Renormalization Method for the Onset of Stochasticity in a Hamiltonian System'.
Physics Letters Vol. 83A7, (1981) 307-403.

[74] NAG-Library

[75] J.L.Tennyson, M.A.Lieberman, and A.J.Lichtenberg,
In M.Month and J.C.Herrera (eds.)
'Nonlinear Dynamics and the Beam-Beam Interaction',
AIP Conference Proceedings **57**(p.158)

[76] V.I. Arnold,
'Small Denominators and Problems of Stability of Motion in Classical and Celestial Mechanics',
Russian Mathematical Surveys **18:6** (1963) 85.

[77] B.V. Chirikov and D.L. Shepelyansky,
'The Statistics of the Poincaré Recurrence and the Structure of the Stochastic Layer of a Nonlinear Resonance',
Preprint 81-69, Institute of Nuclear Physics, Novosibirsk (1981).
PPPL Trans. 133, Princeton (1983)

[78] T. Chen and S. Peggs,
'Beam-Beam Tune Modulation, the Driven Gravity Pendulum, and Josephson Junctions',
Proceedings of the third ICFA beam dynamics workshop, Novosibirsk (1989).

[79] H.-J. Eckoldt, private communication (1992).

[80] O. Brüning (DESY),
'Power Supply Ripple in the HERA-p Storage Ring',
In 'Bad Lauterberg 1992, Proceedings, Harz Seminar', 411-419 (1992)

[81] R.Bacher, R.Lange, K.-H.Meß, M.Seidel,
'Electrical Test of the HERA-p Octant WL',
DESY HERA 90-16 (September 1990)

[82] H. Kaden,
'Wirbelströme und Schirmung in der Nachrichtentechnik',
Springer-Verlag / Berlin-Göttingen-Heidelberg, 1959.

[83] P. Schmüser, private communication (1992).

[84] R.Bacher, private communication (1992).

[85] R.Bacher, K.-H.Meß and M.Seidel,
'Transmission Line Characteristics of the Superconducting HERA Dipole and Quadrupole String'
Proceedings of the 1992 High Energy Accelerator Conference, Hamburg (1992).

[86] H.-J. Eckoldt,
'Simulation of Transmissionline Effects within an Octant of the Superconducting HERA Proton Ring during an Energy Dump',
Proceedings of the 1992 High Energy Accelerator Conference, Hamburg (1992).

[87] J. Roßbach,
'Fast Gound Motion at HERA',
DESY **89-023**(1989).

[88] W. Decking (DESY),
'Zusammenhang zwischen Bodenbewegungen und der Strahlschwankungen in Speicherringen am Beispiel HERA',
DESY HERA 90-13 (August 1990)

[89] K. Flöttmann (DESY),
'Untersuchungen mechanischer Schwingungen von supraleitenden Quadrupolmagneten und ihres Einflusses auf die Strahlstabilität bei HERA',
DESY HERA 90-09 (August 1990)

[90] J. Roßbach and P. Schmüser,
'Basic Course on Accelerator Optics',
Lectures given at the CERN Accelerator School,
DESY M-93-02, February 1993.

[91] Meß, Seidel: Frequency spectrum of the loss rates.

[92] O. Brüning, K.-H. Meß, M. Seidel, F. Willeke,
'Measuring the Effect of an External Tune Modulation on the Particle Diffusion in the Proton Storage Ring of HERA',
DESY HERA 94-01 (Januar 1994)

[93] R. Nagaoka, K. Yoshida and M. Hara,
'Nonlinear dynamics with sextupoles in low-emittance light source storage rings',
Nuclear Instruments A302 (1991), 9-26

[94] O. Brüning (DESY),
'Diffusion in a FODO Cell due to Modulation Effects in the Presence of Non-Linear Fields',
Particle Accelerators 41, pp 133-151 (1993)

[95] B.H. Wiik,
'Design and Status of the HERA Superconducting Magnets',
DESY Hera 88-05 (April 1988)

[96] O. Brüning (DESY),
'Emittance Growth in Proton Storage Rings due to the Combined Effect of Non-Linear Fields and Modulation Effects with more than one Frequency',
DESY-HERA 93-10 (October 1993).

[97] L.R.Evans, J.Gareyte, 'The Beam-Beam Effect in the SPS',
CERN SPS/82-8(DI-MST) (1982)

[98] L.R.Evans, 'The Beam-Beam Interaction'
CERN Accelerator School 'Antiprotons in Colliding Beam Fascilities',
Geneva 1984, CERN 84-15(1984)

[99] R. Brinkmann,
'Proton Emittance Growth Caused by Electron RF Noise and the Beam-Beam Interaction in HERA',
DESY M-88-04 (November 1988) 17-19.

[100] A. Piwinski,
'Intra-Beam Scattering',
Proc. of the 9^{th} Int. Conf. on High Energy Accelerators, Stanford, Springfield (1975), 405 - 409.

[101] A. Piwinski,
'Intra-Beam Scattering',
CERN Accelerator School, Nordwijkerhout 1992, CERN 92-01 (1992).

[102] E. Karantzoulis and J.R. Maidment,
'Estimates of Intra-Beam Scattering in HERA',
DESY HERA 85-12 (1985)

[103] M. Seidel,
'Determination of Diffusion Rates in the Proton Beam Halo of HERA',
DESY HERA 93-04 (April 1993)

[104] M. Seidel, private communication.

[105] W. Bialowons (DESY),
'Zusammenfassung des Luminositätsbetriebes '92',
In 'Bad Lauterberg 1993, Proceedings, Harz Seminar', 33-70 (1993)